SAND REPORT
SAND2003-0153
Unlimited Release
Printed January 2003

Measurement and Modeling of Energetic Material Mass Transfer to Soil Pore Water – Project CP-1227 Annual Technical Report

James M. Phelan, Stephen W. Webb, Joseph V. Romero, James L. Barnett, Fawn Griffin, and Mehdi Eliassi

Prepared by
Sandia National Laboratories
Albuquerque, New Mexico 87185 and Livermore, California 94550

Sandia is a multiprogram laboratory operated by Sandia Corporation, a Lockheed Martin Company, for the United States Department of Energy under Contract DE-AC04-94AL85000.

Issued by Sandia National Laboratories, operated for the United States Department of Energy by Sandia Corporation.

Available to DOE and DOE contractors from
U.S. Department of Energy
Office of Scientific and Technical Information
P.O. Box 62
Oak Ridge, TN 37831

Telephone: (865)576-8401
Facsimile: (865)576-5728
E-Mail: reports@adonis.osti.gov
Online ordering: http://www.doe.gov/bridge

Available to the public from
U.S. Department of Commerce
National Technical Information Service
5285 Port Royal Rd
Springfield, VA 22161

Telephone: (800)553-6847
Facsimile: (703)605-6900
E-Mail: orders@ntis.fedworld.gov
Online order: http://www.ntis.gov/ordering.htm

SAND2003-0153
Unlimited Release
Printed January 2003

Measurement and Modeling of Energetic Material Mass Transfer to Soil Pore Water – Project CP-1227 Annual Technical Report

James M. Phelan, Stephen W. Webb and Joseph V. Romero
Environmental Technology Department

James L. Barnett and Fawn Griffin
Explosive Subsystems Department

Mehdi Eliassi
Geohydrology Department

Sandia National Laboratories
P.O. Box 5800
Albuquerque, NM 87185-0719

Abstract

Military test and training ranges operate with live fire engagements to provide realism important to the maintenance of key tactical skills. Ordnance detonations during these operations typically produce minute residues of parent explosive chemical compounds. Occasional low order detonations also disperse solid phase energetic material onto the surface soil. These detonation remnants are implicated in chemical contamination impacts to groundwater on a limited set of ranges where environmental characterization projects have occurred. Key questions arise regarding how these residues and the environmental conditions (e.g. weather and geostratigraphy) contribute to groundwater pollution impacts. This report documents interim results of experimental work evaluating mass transfer processes from solid phase energetics to soil pore water. The experimental work is used as a basis to formulate a mass transfer numerical model, which has been incorporated into the porous media simulation code T2TNT. Experimental work to date with Composition B explosive has shown that column tests typically produce effluents near the temperature dependent solubility limits for RDX and TNT. The influence of water flow rate, temperature, porous media saturation and mass loading is documented. The mass transfer model formulation uses a mass transfer coefficient and surface area function and shows good agreement with the experimental data. Continued experimental work is necessary to evaluate solid phase particle size and 2-dimensional effects, and actual low order detonation debris. Simulation model improvements will continue leading to a capability to complete screening assessments of the impacts of military range operations on groundwater quality.

Acknowledgements

This work was sponsored by the Strategic Environmental Research and Development Program (SERDP), under the technical direction of Jeff Marqusee and programmatic direction of Brad Smith. Sandia is a multiprogram laboratory operated by Sandia Corporation, a Lockheed Martin Company, for the United States Department of Energy under Contract DE-AC04-94AL85000.

Contents

List of Figures

List of Tables

1.0 Introduction

SERDP is seeking techniques and knowledge that will permit assessment of the environmental impact of residual energetic material from test and training operations. Low-order detonations that disperse discrete solid phase particles onto and into the soil leave the greatest legacy of energetic material residues. One principal environmental impact is contamination of aquifers. The energetic material most likely to impact aquifers is RDX due to its low drinking water advisory limits, low retardation during soil transport and low rate of environmental degradation.

Understanding the mass transfer rate from discrete solid phase particles into the soil pore water is critical to the impact analysis of these residues for groundwater contamination. Weather is an important process that drives the mass transfer phenomena. This work seeks to analyze this mass transfer process using laboratory measurement and numerical simulation methods. The results from this work will create a new predictive ability to assess the migration potential of residual energetic materials. The transition plan will extend this work to evaluate groundwater impact and range management strategies.

Objective

This work seeks to develop an energetic material source release function that describes the mass transfer of solid phase energetic materials to a solute in soil pore water, and to incorporate this process in a solute transport model with linkages to time dependent weather phenomena. The ultimate objective of this work is to develop a screening level simulation tool, with data defining an energetic material source release function, that can be used to assess groundwater pollution management strategies for residual energetic materials left by military testing and training operations.

2.0 Background

Energetic Material Deposits

Distinct solid phase energetic material ejected from a detonation may be either large chunks or dispersed as fine particulates. In addition, the heat of partial detonation may melt and vaporize portions of the energetic material, followed by solidification into discrete particles or recondensation onto soil particles. Figure 1 shows low-order detonation debris found buried in the soil following a 105 mm artillery impact into soil (Phelan et al, 2001). From the same test, Figure 2 shows a soil aggregate containing an apparent vapor deposit of soot with high levels of extractable TNT (1400 mg/kg) and Figure 3 shows solid phase energetic material about 20 m from the impact location.

Figure 1. Low Order Detonation Debris Containing TNT Main Charge (~ 30 cm long)

Figure 2. Soil Aggregate Containing Soot and Extractable TNT (~ 5 cm long axis)

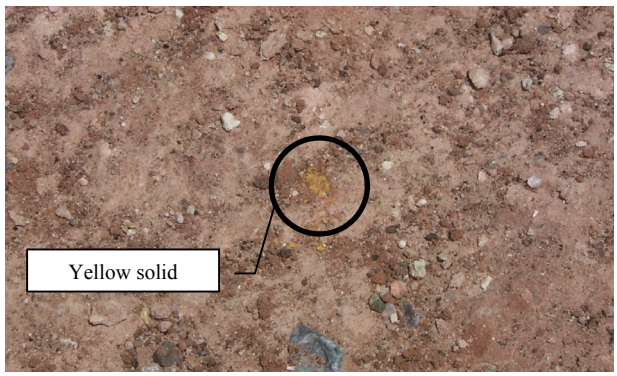

Figure 3. Unreacted TNT Ejected from Low Order Detonation (~ 5 cm dia)

These materials may have the same physical properties as the main charge in the ordnance, or they may have been altered by the temperature, shock and dispersal during detonation, and by weathering. For example, we have evidence of a low-order detonation of a 60 mm mortar that appeared to have melted the Comp B main charge, then splattered the material onto the walls of the test chamber. The physical properties of detonation debris have not been well studied.

The surface area of the energetic material increases dramatically as the particle size decreases. We believe that study of the leaching of fine particulate matter will provide great insight and experimental control. Once the experimental methods and fundamentals of leaching have been established, testing of other detonation debris materials can follow.

Solid Phase Energetic Materials in Soils

Traditional field soil sampling and chemical residue analysis is often unable to determine the presence of solid phase energetic material. The soil extraction and analyte determination process averages the measured energetic material quantity over the entire mass of the soil sample, masking the potential presence of small particles of energetic material. Estimating the transition from classical soil chemical residues based on sorption equilibria to the potential presence of a separate solid phase energetic material may be important in the selection and use of appropriate fate and transport analysis tools.

One method to estimate the transition of trace soil residues to the potential presence of solid phase energetics is through evaluation of phase partitioning equilibria (Jury, 1991; Phelan and Barnett, 2001). A soil system will partition the total mass of chemical between the air, water and solid phases according to equilibrium partitioning theory. The mass fraction in each soil phase is established by the air-water partition (Henry's constant), the soil-water partition (K_d) and soil-air partition ($K_{d'}$) coefficients. The greater the total soil residue (among all soil phases), the greater the concentration in each of the soil phases. However, when the total soil residue approaches a value that, when partitioned, approaches the water solubility limit, any additional mass added to the system must partition into a separate solid phase. Total soil concentrations that do not exceed the partitioning equilibria will behave as a traditional pollutant. Total soil concentrations that exceed this value may require analysis tools that include the behavior of a separate solid phase.

Figure 4 presents the results of an analysis that shows the maximum total soil concentrations of RDX that a soil can partition before a separate solid phase must exist. At 20°C, the maximum solubility of RDX in water is about 45 mg/L. Due to the low vapor pressure and air-water partitioning coefficient, the soil-water partition coefficient (K_d) is the principal factor influencing the maximum total soil residue. Figure 4 shows that total soil concentrations above 30 to 70 µg/g (sum of liquid, sorbed to soil and vapor

phases) indicate the potential presence of solid phase energetics in the soil. The lower the soil-water partitioning coefficient (K_d) the lower the maximum total soil residue because of the smaller sorption capacity of the soil.

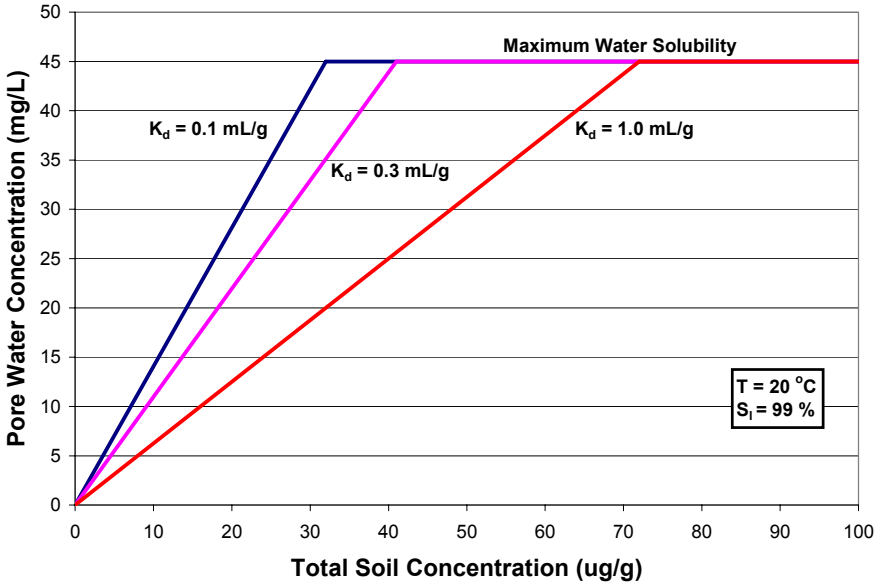

Figure 4. Effect of Soil Water Partitioning Coefficient (K_d) on Maximum Soil Residue for RDX

Importance of Surface Conditions

Leaching of energetic material from detonation debris is likely to be controlled by surface weather phenomena. These materials are found on and in near-surface soils, where large changes in temperature, pore water velocity and soil saturation occur. Higher temperatures increase the solubility of the energetic material in water. Increased pore water velocity may increase the mass transfer rate and a higher water flux will increase the mass of contaminated water. Increased saturation fills more pore space potentially increasing contact with the energetic material.

The soil surface temperature has a strong diurnal variation due to the balance of solar radiation, long-wave radiation, heat conduction into the soil, and evaporation. For example, the diurnal variation for a bare soil in a dry climate has been measured to be between 15°C and 50°C with an approximately sinusoidal variation (Braud et al., 1993). The solubility data for RDX shows a change in solubility of about a factor five for this temperature range (Phelan et al., 2002).

The soil surface and near-surface conditions, such as the temperature, saturation and evaporation, are driven by local weather conditions including pressure, air temperature, relative humidity, wind speed, solar radiation, long-wave radiation and precipitation. Webb and Phelan (2000) modeled the effect of diurnal and seasonal weather on the surface and near-surface TNT, DNT, and DNB chemical signatures from a constant source release simulation of a buried landmine or UXO. Liquid-phase chemical

concentrations showed about a 2-order of magnitude diurnal variation under dry conditions, and about an 8-order of magnitude range over the entire year. Therefore, the effect of weather conditions on chemical concentrations of energetic materials is expected to be significant.

Webb and Phelan have used the T2TNT code (Webb et al., 1999), which is a modified version of TOUGH2 (Pruess, 1991), for simulation analysis of environmental impacts to energetic materials. The T2TNT code has been successfully compared to chemical concentration data from column tests, including wetting and drying cycles (Phelan et al., 2000, 2001). Modifications include the incorporation of surface weather conditions as well as chemical properties and transport coefficients appropriate for TNT, DNT, and DNB. For the surface weather conditions, the SiSPAT model developed by Braud et al. (1995) has been used (with permission). The SiSPAT model includes the effect of weather on the surface boundary layer including the influence of plants, and the impact of vegetation on subsurface moisture through roots. Only the bare soil version of the SiSPAT model (without vegetation) is included in T2TNT at the present time.

The effect of weather cycles on surface and near-surface conditions, including temperature and liquid saturation, extend from the surface down to a few meters below the surface. Further down, the soil moisture content is not influenced by the surface conditions except as a net recharge of water. Examples are given by Faybishenko (2000), who presents results from Kutilek and Nielsen (1994) of soil pressure head (capillary tension) as a function of depth for a semi-arid region of North China for April and August. The profiles are significantly different from the surface down to about 8 m. From 8 m to about 15 m, the two profiles merge. Below 15 m, the profiles diverge again due to a fluctuating water table.

Similar results are given by Andraski (1997) for native soil in an arid site in Nevada. Soil water content with depth is presented for nonvegetated and vegetated soil over a period of up to 5 years. For the nonvegetated soil, the soil moisture profiles down to 1.5 to 2.0 m are a function of the time of year and the year; below that depth, the water contents are essentially the same over the 4 year period studied. For the vegetated soil, the profiles down to about 1 m vary widely with the time of the year and, to a lesser degree, with the year. The profiles converge below this depth for the 5 year time period of this investigation. Therefore, the effect of surface conditions including vegetation is probably confined to the top few meters of soil.

Mass Transfer from Energetic Materials to Water

In the surface and near-surface zones, contamination will occur due to mass transfer from the energetic material to the soil water during variable saturated conditions. Particle-to-liquid mass transfer has been extensively studied for liquid-saturated packed bed systems in chemical engineering (Wako and Kaguei, 1982). Unsaturated packed beds have also been analyzed, although to a lesser extent. Range

contamination from low order detonation debris may be comparable to trickle bed reactors (Satterfield, 1978).

More recent work has explored mass transfer of nonaqueous phase liquids (NAPLs) to soil pore for evaluation of impacts on the rate of groundwater restoration (Powers et al., 1994; Imhoff et al, 1993; Miller, et al., 1990). This research evaluated mass transfer in porous media using Reynolds numbers more representative of rainfall rates in near surface soils and with residual NAPL saturation. Residual NAPLs leave discrete blobs potentially similar in size to particulate energetic materials deposited from detonations. Notwithstanding the differences between NAPL versus solid phase energetics, the process for laboratory measurement of mass transfer and simulation modeling is analogous. Derivation of a dimensionless mass transfer correlation as a function of critical properties is an important first step. Because information for unsaturated fixed beds is limited, the discussion below will concentrate on saturated conditions.

In these packed bed systems, the Sherwood number is usually correlated with the Reynolds number. The Sherwood number is a dimensionless parameter, or

$$Sh = \frac{k \cdot D_p}{D_v} = f(\mathrm{Re}) \qquad [1]$$

where k is the mass transfer rate from the particle, D_p is the particle diameter, and D_v is the diffusion coefficient. The Reynolds number is the ratio of the fluid velocity times the particle diameter divided by the fluid viscosity. In many situations, such as NAPL dissolution as given by Powers et al. (1992), the interfacial area of the mass source is not measured, and a modified Sherwood number, Sh^*, can be defined using a lumped mass transfer coefficient ($k^* = k\ a$), or

$$Sh^* = \frac{k \cdot D_p^{\ 2}}{D_v} \qquad [2]$$

where a is the specific surface area. The lumped mass transfer coefficient can then be evaluated directly from the effluent concentration from a column flow test apparatus.

While soils contain a wide range of particle diameters, an average or mean particle size is sometimes employed for Reynolds number calculations. Using a 1 mm mean grain size and a rainfall rate (or net recharge) of 1 cm/day, the Reynolds number is very low, about 10^{-4}. Models for the mass transfer rates (modified Sherwood number) from NAPLs under saturated flow conditions with these low Reynolds numbers ($Re < 1$) have been developed by a number of authors, including Powers et al. (1992, 1994) and Imhoff et al. (1993). NAPL dissolution behavior is not entirely analogous to energetic materials because the NAPL is a liquid and the size of the NAPL "particles" will be determined by the soil particle size distribution.

These models need to be modified for application to the mass transfer from solid phase particles deposited on the ground surface from low order detonations. The functional form of the correlations are in terms of a Reynolds number such that the modified Sherwood number and the mass transfer from the particles, goes to zero as the Reynolds number goes to zero. In the present situation, if there is no precipitation, the local Reynolds number could be zero, but mass transfer will continue due to diffusion from the energetic material into the surrounding water. The correlations will be modified by the addition of a constant term, as is common practice in packed bed mass transfer (Wakao and Kaguei, 1982).

The above relationships are only tentative due to a number of factors. First of all, these relationships are derived for saturated flow conditions. For unsaturated flow, few investigations have been conducted. Based on a preliminary analysis of heat transfer in unsaturated flow, the results of Plumb (1991) indicate that the heat transfer coefficient is approximately proportional to the liquid saturation. By analogy, mass transfer can be assumed to be proportional to the liquid saturation. As mentioned above, NAPL "particle" sizes will be influenced by the soil pore size distribution, which will not be the case for energetic particles. Sorption and degradation losses involving energetic particles and the soil may further complicate experimental determination of the mass transfer rate, which may be avoided by using a synthetic soil made from glass beads. Nevertheless, the correlation methods developed for dissolution of NAPLs in soils under saturated conditions will be used as an initial starting point for the present investigation.

3.0 Project Plan

This project has been divided into two tasks, Experimental and Modeling, as follows:

Task 1: Experimental

Measurement of mass transfer from solid particles to water has been performed predominantly with packed bed reactors in support of chemical engineering operations research (Wakao and Kaguei, 1982) and with NAPLs in porous media (Powers et al., 1994). Experimental design for this application was patterned after this previous work. The principal parameters that control the mass transfer rate include:

- Soil saturation
- Porous medium particle size distribution
- Fluid flow rate
- Energetic material surface area
- Temperature
- Buried or surface deposit
- Steady or pulsed flow
- Energetic material type

Figure 5 shows a schematic of the soil column mass transfer test apparatus for unsaturated soil studies. Soil columns were packed with glass beads that represent a porous media that is not chemically reactive or sorptive and can be created with hydraulic properties similar to a sandy loam. A layer of energetic material particles was mixed with the porous media and placed between two clean sections to form a dilute packed bed. The upper section helps establish a uniform flow profile and the bottom section is important to control unsaturated conditions.

A porous membrane is located at the base of the column in order to control unsaturated conditions. Water present in unsaturated porous media is held under tension that is analogous to capillary rise in small diameter tubing. Smaller pores cause more capillary tension than larger pores. The porous membrane has a much smaller pore size distribution than the porous medium, which keeps the porous membrane saturated even when the porous medium above is unsaturated. A vacuum greater than 600 mbar is needed to desaturate the porous membrane; this 600 mbar is the bubbling or air-entry pressure. The vacuum conditions established below the porous membrane translate into the porous media establishing a regulated capillary tension, which controls the unsaturated water content of the porous media. Water from the porous media flows through the porous membrane with minimal head loss because the membrane is 1-mm thick and designed for high flow. A detailed description of this system is found in Van Genuchten and Wierenga (1986).

Soil moisture characteristic curves were measured for the glass bead mixture. This correlates soil tension (applied vacuum) to volumetric water content. A vacuum of about 80 to 200 mbar is sufficient to maintain the porous medium at the desired wetness (or saturation). Several mini-tensiometers were

placed into the wall of the soil column (penetrating < 1 cm into the column) to allow point measurements of the porous media tension. These were placed on each side of the explosive particle bed and midway between the explosive bed and the top and bottom of the column.

Water samples were collected in a fraction collector set to optimize the number of samples per day depending on the set water inflow rate. Time sequenced sample collection allows an evaluation of the time-dependent behavior of the mass transfer. Water samples were analyzed by Reverse Phase High Performance Liquid Chromatography optimized for RDX and TNT elution times.

U.S. Military Composition B was used as the principal source material to allow data collection for both RDX and TNT in a formulation commonly used in military training operations. RDX is likely to have the greatest threat to groundwater as it has the lowest drinking water advisory (McLellan, et al., 1988), sorbs poorly to soils (Singh, 1988), and has a low degradation rate under typical aerobic vadose zone pore water conditions (Hawari, J., 2000).

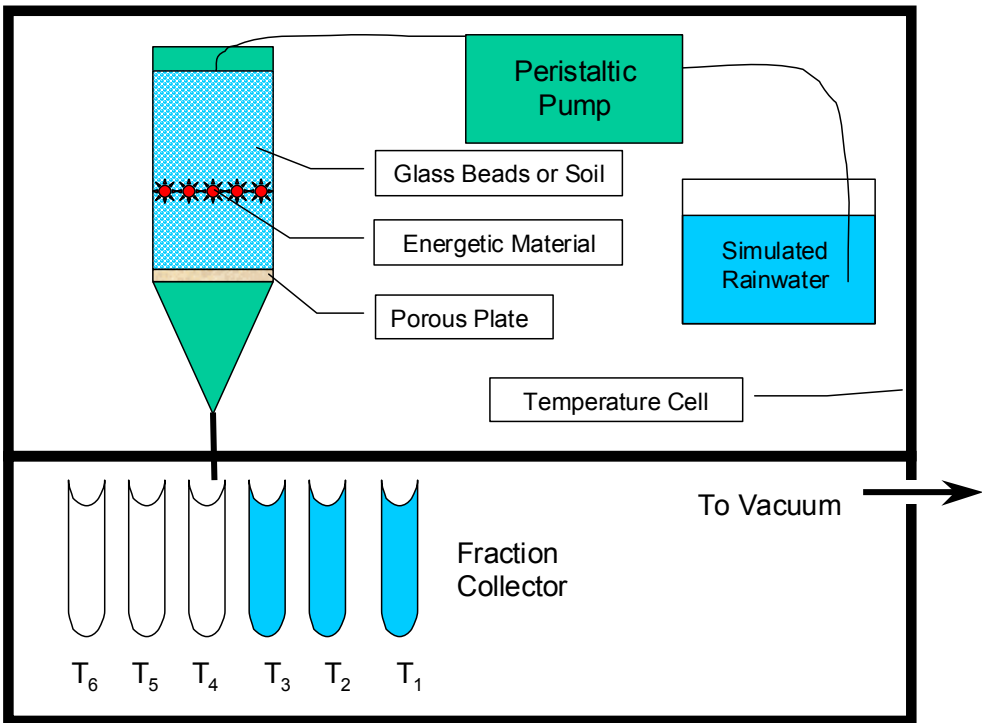

Figure 5. Laboratory Experimental Apparatus

The tests will involve two phases of experimentation and model development. Phase I will consist of an initial series of experiments designed to determine the critical parameters affecting the mass transfer of energetic materials to pore water and the derivation of a mathematical function that incorporates the most significant factors. Phase II will evaluate in more detail the factors that have the greatest impact in the mass transfer process and evaluate actual post blast residue with soil obtained from test or training ranges.

This will allow a comparison of artificial glass bead with manufactured explosive particles with more realistic conditions found in the field.

Task 2: Modeling

The effect of weather cycles on surface and near-surface conditions, including temperature and liquid saturation, extends from the surface down to a few meters below the surface. At greater depths, the soil moisture content is not influenced by the surface conditions except as a net recharge of water. Therefore, except for areas with shallow water tables (< 10m), the vadose zone can be divided into a near-surface region and a subsurface region. In the subsurface region, existing vadoze zone flow and transport codes can be employed with appropriate sources (water and chemicals) from the near surface.

This work is developing a model for a source release zone, which calculates the water and chemical source term for use in a vadose zone contaminant transport simulation tool (Figure 6). The near-surface region model considers the effect of weather on the surface conditions. Variables influencing the surface interface include pressure, temperature, relative humidity, wind speed, solar radiation, long-wave radiation and precipitation. Models for the boundary layer at the surface are used to calculate the heat and mass transfer rates between the atmosphere and the ground surface, including evaporation. Solar radiation has a significant influence on the surface temperature, which may have a diurnal variation of many tens of degrees.

The T2TNT code, which is based on the TOUGH2 code (Pruess, 1991), is used for this modeling effort because it includes the impact of weather data on the surface and near-surface environment. Vegetation will also influence the surface heat and mass transfer through changes to the boundary layer resistance, interception of solar radiation, as well as subsurface mass transfer through the root system. At present, T2TNT does not include the effects of vegetation; modification of T2TNT to include vegetation is not included in this effort. Currently, T2TNT will be most applicable to active test and training ranges where plant coverage can be assumed to be negligible.

In order to calculate the source flux from the source release zone, an energetic material source function is being added to T2TNT. This function will be dependent on numerous parameters, including the local saturation, temperature, pore water velocity, material surface area, etc. Initial development of this function is decribed later in this report.

T2TNT was written in the inverse-modeling framework of ITOUGH2 (Finsterle, 1999). As experimental data are obtained, inverse modeling will be used iteratively to perform data-model comparisons to improve the form of the energetic material source function and to evaluate the sensitivities of the function to the various dimensionless groups. Pretest predictions will also be conducted for upcoming tests to provide insight into the test and the predictive capabilities of the model. The result of

the modified code will be an energetic material mass and water mass source rate as a function of time, which can be incorporated into existing vadose zone codes.

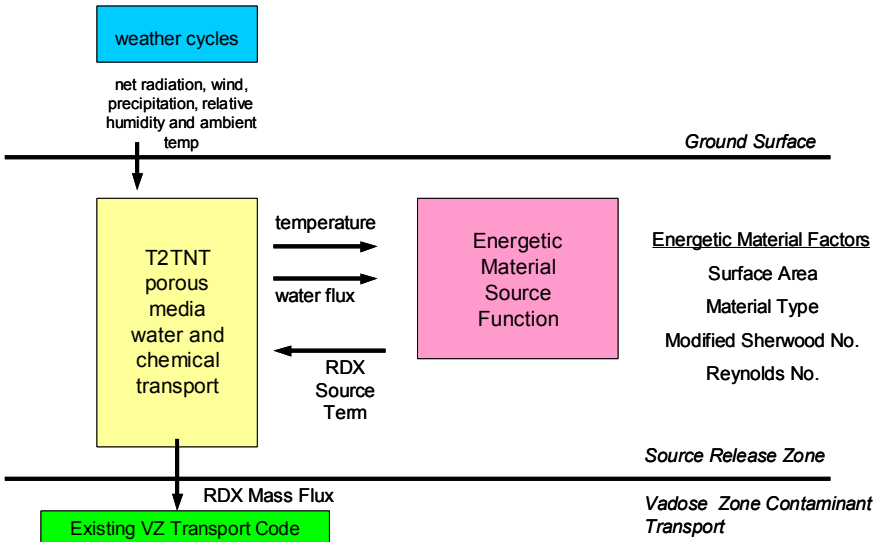

Figure 6. Simulation Modeling Approach

Table 1 shows the task, milestone and deliverable schedule for this project.

Table 1 – Master List of Tasks, Milestones and Deliverables				
Task Name	Milestone	Date	Status	Deliverable
1 - Phase I Experiments	Complete solubility kinetics pretest	8/01	Completed	Phelan, J.M, J.L. Barnett, J.V. Romero, D.R. Parker, 2002. Solubility and Dissolution Kinetics of Composition B in Water. Sandia National Laboratories Report SAND2002-2420, December 2002.
	Complete Phase I, Test Group A	11/01	Completed	
	Complete Phase I, Test Group B	01/02	Completed	
2- Initial Model Development	Develop Preliminary Form of Energetic Material Source Function	8/01	Completed	
	Integrate with T2TNT	11/01	Completed	
	Compare Modified T2TNT with Experimental Data	02/02	Completed	
3 – Phase II Experiments	Phase II Test Plan	02/02	Completed	
	Complete Phase II, Test Group A	06/02	Completed	
	Complete Phase II, Test Group B	09/02	Completed	
4 – Revised Energetic Material Source Function	Complete New Energetic Material Source Function	06/02	Completed	
	Compare Energetic Material Source Function with Phase II Experimental Data	11/02	Completed	
5 – Technical Reports to SERDP	Annual Technical Report	12/01	Completed	Phelan, J.M., S.W. Webb, J.V. Romero and J.L. Barnett, 2001. FY01 Interim Technical Report, Strategic Environmental Research and Development Program, Project 1227, Measurement and Modeling of Energetic Material Mass Transfer to Soil Pore Water.
	Annual Technical Report	12/02	This report	Phelan, J.M., S.W. Webb, J.V. Romero, J.L. Barnett, F. Griffin, M. Eliassi and J.L. Brainard, 2002. Measurement and Modeling of Energetic Material Mass Transfer to Soil Pore Water – Final Report, Project CP-1227. Sandia National Laboratories Report SAND2002-xxxx, December 2002.

4.0 Experimental Methods

4.1 Test Plans

Test plans were developed in the project proposal based on best judgement of the most important controlling factors. As the tests were completed, subsequent tests were designed to assess certain factors in more detail. A total of twenty-one distinct tests were successfully completed. Table 2 shows the factors explored in each test phase and group.

Table 2. Experimental Test Phases and Principal Factors

Test Phase	Principal Factors	Mass Transfer Test Designator
Phase I, Test Group A	Flow, temperature, EM particle size	MT1, MT2, MT3
Phase I, Test Group B	Porous media saturation	MT5, MT12
Phase II, Test Group A	Bed loading, bed depth, initial wetting rate	MT6, MT7, MT8, MT8b, MT8c, MT8d, MT9b2, 9b3
Phase II, Test Group B	Flow, EM particle size, detonation debris	MT10, MT13, MT14, MT11, MT15, MT16, MT17, MT18

4.2 Chemical Analysis

HPLC Method.

Water samples were analyzed by RP-HPLC using a Waters 600E System Controller, Waters 717 Plus Autosampler, and a Waters 996 Photodiode Array Detector. The samples were injected (10µL) into either a Waters Xterra RP-C18 column (4.6 mm x 250 mm) or a Waters Symmetry RP-C18 column and eluted with a 45:55 water and acetonitrile eluant run in isocratic mode with a flow rate of 1.00 mL/min at approximately 35°C. The photodiode array detector accumulated all peaks found at the 254 nm wavelength.

The standards used for calibration were prepared from stock solutions of recrystallized RDX (50 mg in a solution of 50 mL acetonitrile for a 1000 ppm concentration) and recrystallized military grade TNT (50 mg in a solution of 50 mL acetonitrile for a 1000 ppm concentration). Table 3 shows the dilutions of the stock solutions prepared for calibration of RDX and TNT. Each standard was run in duplicate.

Table 3. RDX and TNT Standard Compositions

40 µL RDX solution	100 µL TNT solution	860µL distilled water	40 ppm RDX 100 ppm TNT
30 µL RDX solution	80 µL TNT solution	890 µL distilled water	30 ppm RDX 80 ppm TNT
20 µL RDX solution	60 µL TNT solution	920 µL distilled water	20 ppm RDX 60 ppm TNT
10 µL RDX solution	40 µL TNT solution	950 µL distilled water	10 ppm RDX 40 ppm TNT
5 µL RDX solution	20 µL TNT solution	975 µL distilled water	5 ppm RDX 20 ppm TNT

Table 4 shows a typical calibration data set. Recrystallized RDX is composed of approximately 10% HMX so all RDX area counts are multiplied by a correction factor of 1.10. Detection limits for RDX and TNT using this method are about 50 µg/L.

Table 4. Calibration Chart for RDX and TNT standards

RDX	Area	TNT	Area
Standard (ppm)		Standard (ppm)	
40	618392	100	3323126
40	617110	100	3315721
30	463950.5	80	2641996
30	464988.2	80	2636602
20	308603	60	1988464
20	308652.5	60	1989367
10	154020	40	1328480
10	152578	40	1325699
5	83437.69	20	652792
5	83570.84	20	653216
Slope	15460.23	Slope	33116.58
R2	0.999851	R2	0.99995

Each fraction collector sample was weighed in its container (an 8 mL glass test tube). The tare weight of an empty vial was subtracted to determine the effluent mass of each sample. A 1 mL subsample was collected by disposable pipette, placed in a 2 mL amber autosampler vial. Analysis routines used a calibration check sample every 10 sample runs to verify analyte recovery between 90 and 110%. Recalibration was necessary about every two to four weeks.

4.3 Energetic Material Preparation

Source Material.

The Composition B material was obtained from the demilitarization line at McAlester Army Depot, Oklahoma. Military ordnance was heated until the main explosive charge melted. The melt was poured onto a conveyor belt and allowed to solidify to produce a thin sheet (~ 5 mm). The thin sheet was broken into pieces for packaging and shipment to Sandia National Laboratories in Albuquerque, NM. Figure 7 shows the Composition B material as received.

Figure 7. Composition B Starting Material

Physical/Chemical Properties

The Composition B was further reduced in size by first freezing in liquid nitrogen and then placing it into a ball mill which was rotated for 1 hour at ~ 60 revolutions per minute. The broken material from the ball mill was placed into a sieve shaker, including the zirconium oxide balls, with the sieves as shown in Table 5 and shaken for 1 hour. Size fractions were collected and the shaker operated for another three cycles.

Table 5. Sieve Series

Sieve Number	Opening (μm)
16	1180
18	1000
30	600
35	500
140	106
170	90
635	20

Approximately 500 g of Composition B was processed. Size fractions containing 1000 to 1180 μm, 500 to 600 μm and 90 to 106 μm were collected. There was very little in the less than 20 μm fraction. To quantify the fraction of RDX and TNT in each Composition B size separate, ca. 0.010 g (± 0.0001 g) was dissolved into 10 mL of acetonitrile, diluted 1:1 with water and quantified using the RP-HPLC as described above. The results of the mass fraction of RDX and TNT in each size separate are shown in Table 6.

Table 6. RDX and TNT Mass Fraction in Each Size Separate

Component	90 to 106 μm	500 to 600 μm	1000 to 1180 μm
RDX	0.546	0.598	0.579
TNT	0.454	0.402	0.421

These results indicate that the Composition B size separates remained near the typical 60/40-blend ratio, with slightly lower ratio for the 90 to 106 μm size separate.

The specific surface area of each size separate was measured using a Micromeritics Accelerated Surface Area and Porosimetry 2405 Instrument that measures BET surface area with Kr gas. The results for the BET specific surface area measurements are shown in Table 7 along with estimates based on the geometry of a spherical particle.

Table 7. Specific Surface Area of Composition B Size Separates

Size Fraction	BET Single Point (m^2/g)	BET Multi Point (m^2/g)	Spherical Calculated (m^2/g)
90 to 106 μm	0.3283	0.4961 (± 0.0052)	0.0371
500 to 600 μm	0.1566	0.2071 (± 0.0013)	0.0066
1000 to 1180 μm	0.1750	0.2293 (± 0.0012)	0.0033

This data indicates that the measured BET surface areas are much greater than that estimated from uniform spherical particles by a factor of 13 to 70. This may be due to the non-spherical nature of the size separates and that there were many smaller size particles found on the surface of the larger

particles when observed with scanning electron microscopy (SEM). Figure 8 shows a SEM photograph of the 500 to 600 µm size fraction showing many smaller particles present on the surface of the principal particles.

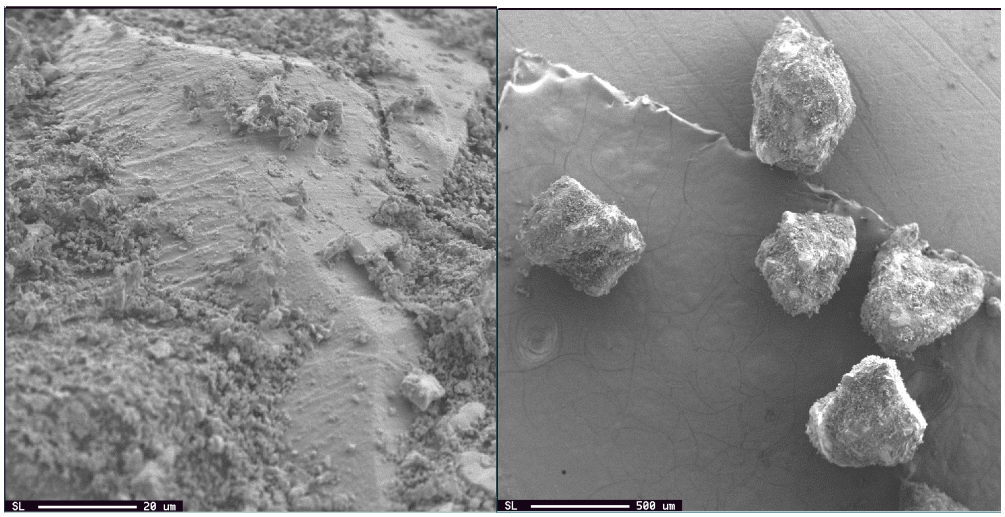

Figure 8. SEM Photograph of 500 to 600 µm size fraction

4.4 Porous Media Characterization

Physical/Hydraulic Properties.

Glass beads were chosen for the first series of experiments because they have limited propensity for biotic and abiotic degradation, and low sorption characteristics. Glass beads obtained from MoSci Corporation (Rolla, MO) were solid soda-lime (GL-0191) with a specific gravity of 2.5.

A glass bead particle size distribution was selected that would approximate a sandy loam soil, providing adequate control of varying states of pore saturation and sufficient hydraulic conductivity to complete tests in short time frames. To determine the saturated hydraulic conductivity (K_{sat}), a falling head test procedure was implemented using the following relationship

$$K_{sat} = \frac{aL}{At_1} \cdot \ln\left(\frac{H_1}{H_2}\right) \qquad [3]$$

where,

a is the area of the standpipe

L is the column length

A is the area of the sample

t is the time interval

and, H_1 and H_2 are the head at t_1 and t_2, respectively

The first glass bead batch produced a K_{sat} lower than desired. In order to increase the K_{sat} value, the percentage of larger particles was increased. The saturated hydraulic conductivity of the second batch

was determined to be about 2.3 E-4 cm/sec, which is in an acceptable range. Figure 9 shows the particle size distribution of glass beads of this second batch.

Min	max	avg	mass %	cum %
0.001	0.037	0.019	14	14
0.037	0.053	0.045	14	28
0.053	0.074	0.064	14	42
0.074	0.105	0.090	12	54
0.105	0.149	0.127	11	65
0.149	0.210	0.180	9	74
0.210	0.297	0.254	8	82
0.297	0.420	0.359	7	89
0.420	0.590	0.505	7	96
0.590	0.840	0.715	4	100

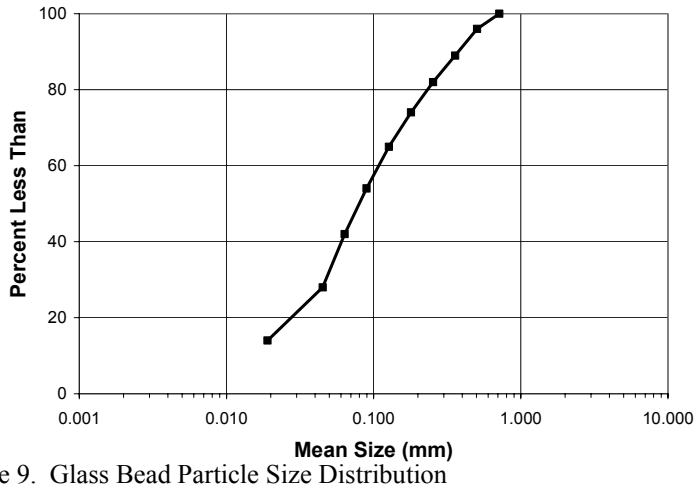

Figure 9. Glass Bead Particle Size Distribution

To control the soil moisture content (also referred to as saturation) in the test apparatus, the capillary tension is adjusted to desired values as indicated on a moisture characteristic curve. Data for the moisture characteristic curve is collected with hanging column and pressure plate equipment using standard protocols (Klute, 1986) and typically represented as volumetric water content versus matric potential.

The traditional method of determining these curves involves establishing a series of equilibrium points either by gravimetric means with hanging column or pressure plate extraction methods. Each method is used for an optimal range of pressure or tension. The hanging column and pressure extractor ranges are from 0 to 300 cm and 300 to 15,000 cm, respectively.

Water contents were measured using the hanging column and pressure extractor method for discrete matric potentials from 0 to 1000 cm water tension. Two samples were averaged using the hanging column method at 20 cm intervals from 0 to 300 cm. In addition, ten samples were tested on the pressure extractor at 600 cm and 1000 cm. Five of the ten samples were weighed for water contents at 600 cm, and then allowed to equilibrate again with the remaining samples at 1000 cm and then re-weighed. Thus, two samples averaged for 0 to 300 cm, five samples were averaged at 600 cm, and 10 samples at 1000 cm. The water content is measured gravimetrically for each tension. The ratio of the mass of water to the mass of soil is determined by:

$$\omega = \theta_g = \frac{M_w}{M_s} \qquad [4]$$

where, M_w is the water mass, and M_s is the mass of soil. From this, the volumetric water content is defined as:

$$\theta_v = \frac{V_w}{V_T} = \theta_g \cdot \frac{\rho_d}{\rho_w} \qquad [5]$$

where, θ_v = volumetric water content, θ_g = gravimetric water content, V_w = volume of water, V_T = total volume, ρ_d = dry bulk density ($\rho_d = \rho_b$), ρ_w = density of water (1 g/cm^3). The dry bulk density of packed glass beads was measured experimentally and was determined to be equal to 1.924 g/cm^3. The primary drainage moisture characteristic curve using this method is shown in Figure 10.

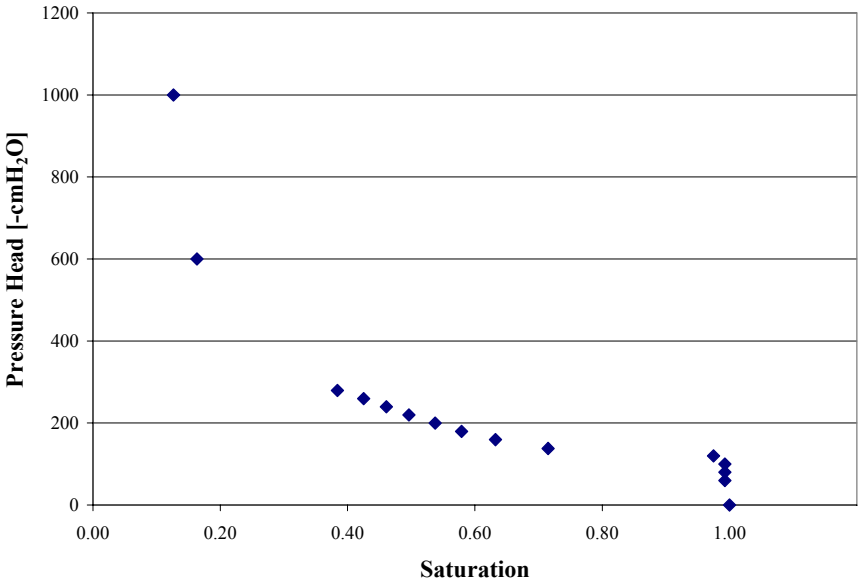

Figure 10. Primary Drainage Results for Glass Bead Tension versus Saturation

The soil water retention curve was fit to the *van Genuchten* [1986] function:

$$S_e = \left[1 + (\alpha \cdot h)^n\right]^{-m} \qquad [6]$$

where: α, n, and m are empirical constants affecting the shape of the retention curve. The air entry pressure is $1/\alpha$ and h is the pressure head.

The unsaturated hydraulic conductivity for the liquid phase is given by Mualem [1986]

$$K(S_e) = K_{sat} \cdot S_e^l \cdot [1-(1-S_e^{1/m})^m]^2 \qquad [7]$$

where K_{sat} is the hydraulic conductivity at saturation, and l is a pore-connectivity parameter estimated to be about 0.5 as an average for many soils. The value of m in equation [7] and [8] is estimated from the fit to the soil retention data (Figure 10). RETC (RETention Curve, US Salinity Lab public domain software) was used to fit the van Genuchten function to the experimental soil retention data. Table 8 shows the parameter estimates determined using the RETC software.

Table 8. Moisture Characteristic Curve Values from RETC Program

Parameter	Value
θ_r	0. cm^3/cm^3
θ_s	0.27 cm^3/cm^3
α	0.009
n	19.9
m	0.05
l	0.5
K_{sat}	2.30E-04 cm/sec

Figure 11 shows the results of the parameter estimates (Table 8) used in equation [7] with the experimental data (Figure 10). Figure 12 shows the estimated liquid hydraulic conductivity using the parameters from the moisture characteristic curve and the Mualem model.

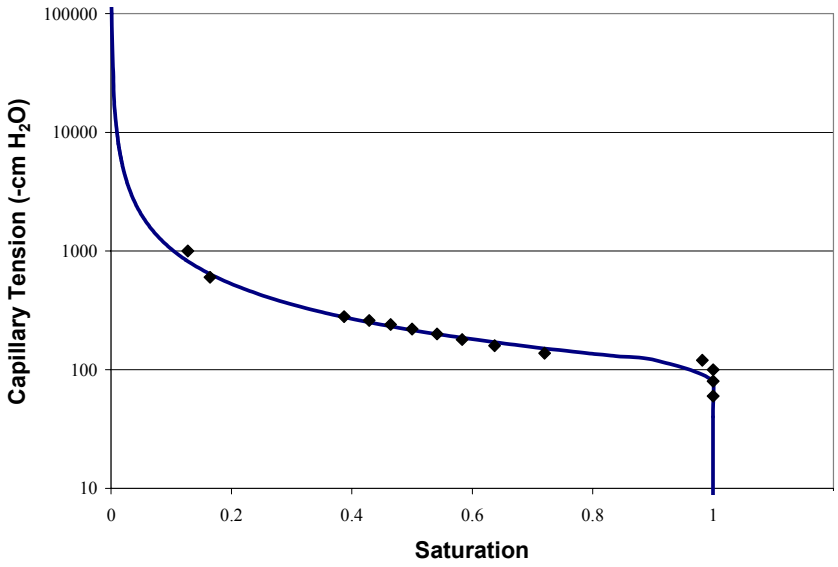

Figure 11. Glass Bead Moisture Characteristic Curve (Table 9)

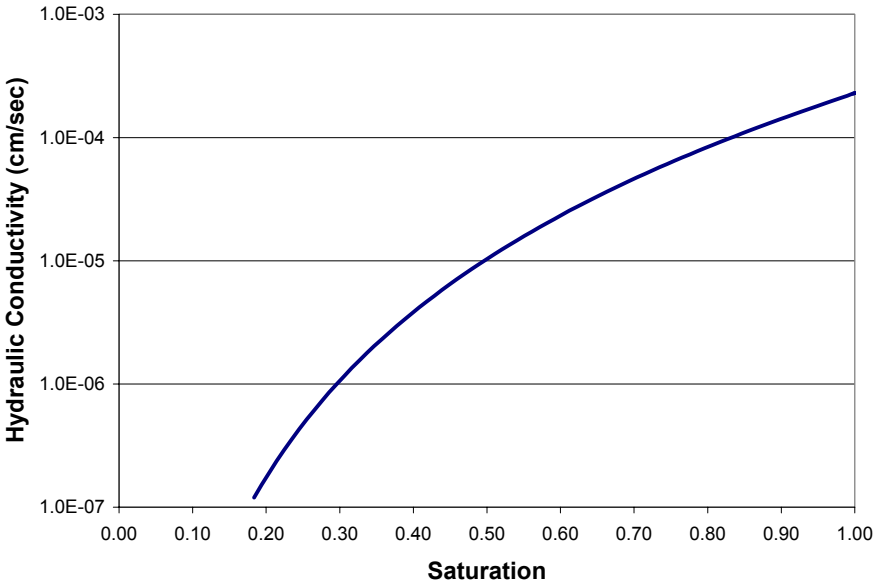

Figure 12. Unsaturated Hydraulic Conductivity Prediction Using Mualem, Eq. [7]

The results from Figure 12 indicate that the glass bead particle size distribution will provide sufficient unsaturated hydraulic conductivity (i.e. adequate water flow rates) to complete experiments in reasonable time periods. The results from Figure 11 indicate this glass bead mixture has sufficient differences in matric potential to maintain constant saturation values at 0.80, 0.60 and 0.40.

Aqueous-Solid Partitioning

Glass beads were selected, in part, because of the low sorption potential. Batch equilibrium sorption tests were performed using 4 g of glass beads and 16 mL of aqueous solution containing about 10 mg/L of both TNT and RDX. A 1 mL sample was collected from each test at 8, 24, 48 and 192 hours, and analyzed by direct injection with the HPLC. Duplicate tests were performed with controls (no glass beads) and with the soda lime glass beads. Table 9 shows the changes in measured aqueous concentrations of TNT and RDX in each test over time and the estimated single point aqueous-solid partition coefficient (K_d) values. These results confirm the very low apparent sorption coefficients for TNT and RDX. Since these tests were not performed at multiple aqueous phase concentrations for each analyte to produce a sorption isotherm, the single point values of K_d are only rough estimates.

Table 9. Soda Lime Glass Bead Aqueous-Solid Partitioning Data and Results

Time (hrs)	Control (mg/L)		Control Replicate (mg/L)		Control Average (mg/L)	
	TNT	RDX	TNT	RDX	TNT	RDX
8	7.7	11.3	7.8	11.4	7.77	11.34
24	7.9	11.5	7.9	11.5	7.89	11.49
48	7.8	11.4	7.8	11.3	7.80	11.37
192	7.7	11.5	7.7	11.4	7.71	11.45
Time (hrs)	Soda Lime Glass Beads (mg/L)		Soda Lime Glass Beads Replicate (mg/L)		Soda Lime Glass Beads Average (mg/L)	
	TNT	RDX	TNT	RDX	TNT	RDX
8	7.7	11.2	7.8	11.2	7.77	11.21
24	7.8	10.8	7.7	10.9	7.71	10.85
48	7.6	10.4	7.6	10.3	7.58	10.33
192	7.3	7.8	7.4	7.8	7.34	7.81
				mass (g)	4.0	4.0
				Vol (mL)	16.0	16.0
				K_d (8 hrs)(mL/g)	0.00	0.05
				K_d (24 hrs)(mL/g)	0.09	0.24
				K_d (48 hrs)(mL/g)	0.07	0.40
				K_d (192 hrs)(mL/g)	0.20	1.87

4.5 Saturated Flow Test Methods

Saturated flow experiments were conducted to evaluate the effects of flow rate, temperature, energetic material particle size, bed loading/depth, and low order detonation debris. Figure 13 below shows a schematic of the saturated column setup. Flow columns were obtained from Soil Measurement Systems; saturated experiments used a 1″ diameter by 6″ long acrylic columns. Each column used a nylon mesh between the top and bottom plate with non-restrictive flow capability to minimize glass bead particles exiting the column.

Saturated column studies were packed in a three-layer composition. The bottom layer contained between 50-60 g of glass bead, the middle layer was the bed depth/loading composed of glass beads mixed with a specific amount of composition B particles for each experiment (5-20 g), and the top layer ranged from 40-45 g. The glass beads and Comp B were weighed separately, then combined to created a uniformly loaded layer. Experiments used either a ~0.5cm or ~2.5cm bed depth. Columns were packed by first pouring in the lower layer and lightly tapping, then adding the CompB layer and tapping, and finally filling with the top layer and tapping until flush with the top of the column. Experiments were initially saturated from below with a slow flow rate between 0.4 – 0.8 ml/hr for one pore volume (~19 ml). Table 10 summarizes the physical properties.

Table 10. Specifications of Saturated Columns

Property	Value
Column diameter (cm)	2.54
Column area (cm^2)	5.07
Column length (cm)	12.60
Column volume (cm^3)	63.85
Column mass (g)	118.82
Bulk density (g/cm^3)	1.77
Particle density (g/cm^3)	2.50
Porosity (cm^3/cm^3)	0.29
Pore volume (ml)	18.71

Following the initial wetting phase, flow rates (0.8, 1.2, 1.8, 3.5 ml/hr) were set for each test and a CF-1 fraction collector gathered samples at each time interval. The initial three experiments (Phase I, Test Group A) used downward flow while the remaining experiments used upward flow to assure the column was saturated. Figure 13 shows a schematic of the saturated flow apparatus. A peristaltic pump (Rainin Co.) was initially used to control flow rates. Later a microprocessor controlled syringe pump (KDS200 series) replaced the peristaltic pump for better consistency and accuracy for low flow conditions. An inline pressure transducer (0-5 psi) and a Type K thermocouple were linked to a Campbell Scientific 21X data logger to monitor pressure and temperature. Temperature values were used to calculate the maximum allowable concentration for each time step (i.e. C_{max}).

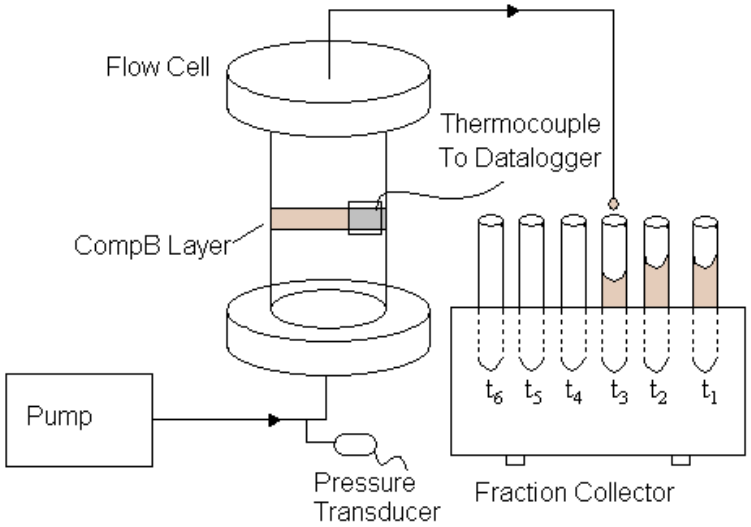

Figure 13. Saturated Column Schematic

Figure 14 shows an actual column; the layer centered vertically covers the cross-sectional area of the column. The discoloration in the column occurred in the early stages of the experiment and remained thereafter. The effluent showed color only for the initial samples. The discoloration is an indication of TNT degradation and was present in each test.

Flow Cell

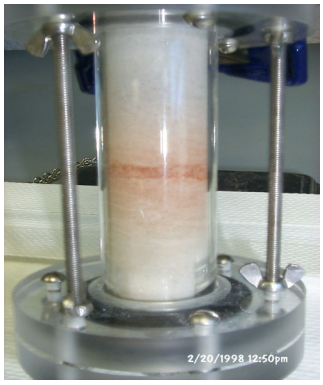

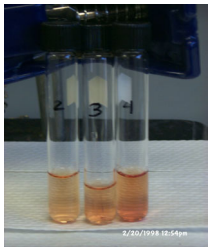

38C Cell Outflow

Figure 14. Flow Cell and Effluent Color

4.6 Unsaturated Flow Test Methods

The tests in Phase I, Test Group B were unsaturated flow tests. The basis for the design is described in Section 2.2. Figure 15 shows a picture of the system including the vacuum box, column, tensiometers, peristaltic pump, and data acquisition system. Figure 16 shows a close up of the column with the Composition B layer installed. Figure 17 shows a close up of a tensiometer showing the porous cup, water filled standoff, and 0-5 psi pressure transducer.

Figure 15. Unsaturated Flow Apparatus

Figure 16. Unsaturated Flow Column, Composition B layer, Tensiometers

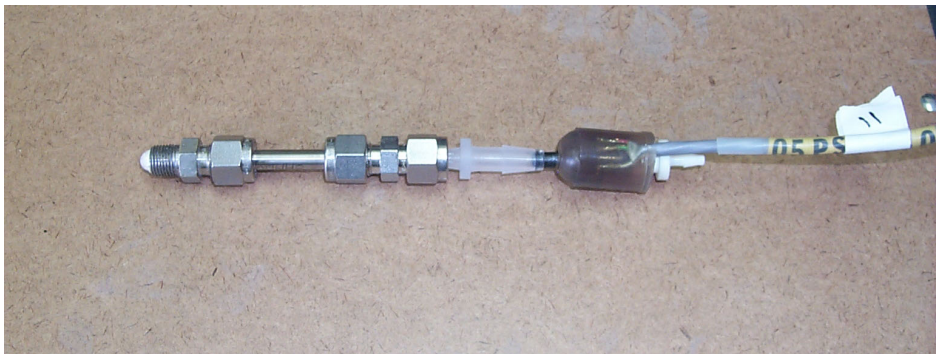
Figure 17. Tensiometer Assembly

Unsaturated columns (2″D x 8″H) were packed in a similar manner as the columns used for the saturated studies, except with larger mass values. Nearly 400g were placed below and above the Comp B layer, and approximately 20g for the Comp B layer itself. Unsaturated columns were also pre-saturated from below for one pore volume (~70 ml) at 3.5 ml/hr for 20 hrs. The experiments used tap water with downward flow into the vacuum box where a fraction collector was used to gather samples at specified time intervals. A matched set of vacuum and water inflow rate created the desired porous media saturation as interpreted from the characteristic curve (Figure 11) and the unsaturated hydraulic conductivity relationship (Figure 12). Tensiometers, with 1 bar porous cups and 0-5psi wet/wet differential pressure transducers, recorded pressure via a CR10x data logger to a laptop computer. A series of four tensiometers were used, shown in Figures 14 and 15. The third tensiometer from the top was in direct contact with the Comp B bed; the tension at this location evaluated the desired saturation. For accurate measurements of inflow, especially flow rates <1 ml/hr, Hamilton 1000 series syringes and KDS230 syringe pump were chosen. Table 11 summarizes the main components used for flow tests.

Table 11. Experimental Equipment

Hamilton 1000 series gastight syringes
Microprocessor controlled syringe pump (KDS200 series, KDS210 & KDS230, infusion/withdrawal)
Rainin peristaltic pump
Vacuum pump
Pressure regulator
CF-1 Fraction collector from Spectrum Chromatography
Campbell Scientific 21x and CR10x dataloggers
Porous Cups: Round bottom straight wall cup, 1 bar standard
PX160 Series: Wet/Wet differential pressure transducers (0 to 5psi –50mV)
2″ x 8″ Column for unsaturated, 1″ x 6″ for saturated studies
Vacuum box
Laptop computer

4.7 Degradation

The concentrations of RDX and TNT in the column effluent are the net result of mass transfer from the solid phase Comp B less any degradation. Glass beads were chosen for the porous media to minimize microbial and geochemical reactions that occur in soils. Tap water was chosen for the mass transfer media because it more closely mimics soil pore water; however, naturally occurring microorganisms are present in tap water that could promote RDX and TNT degradation. Historic information implied that RDX only degraded in strongly reducing conditions; however, more recent test results indicate that RDX can degrade in aerobic conditions (Hawari, 2000).

To evaluate the impact of degradation losses for the mass transfer tests, degradation tests were designed using a slurry mixture of Comb B particles, glass beads and water. While this mixture has a greater water:glass bead ratio than in the mass transfer columns, it allows one to collect aqueous samples over time. Two types of tests were completed: 1) slurry tests where aqueous samples were collected over time, and 2) slurry tests where the entire test was sacrificed at each time step.

Slurry Tests with Aqueous Samples. Two tests were prepared – one to mimic a low mass loading (designated Comp B 1X slurry test) and one to mimic a higher mass loading (designated Comp B 5X slurry test). Each test was prepared by mixing Comp B (100 μm particles) and 190 grams of glass beads, and then adding 100 mL tap water into 500 mL glass amber jars. The 1X slurry test contained 5.5 mg of Comp B and 5X slurry test contained 27.5 mg of Comp B. The slurry tests were not agitated (to mimic soil column conditions) and were held at room temperature (20-23°C). Slurry test 1X was sampled over 316 hours and slurry test 5X was sampled over 766 hours. At the end of each test period, the remaining RDX and TNT in the container was quantified.

Prior to collection of a sample, a stir spatula was used to mix the Comp B/glass beads mixture and then allowed to settle for approximately 30 minutes. A 1 mL sample was removed by disposable pipette,

placed into a plastic syringe and filtered with a 0.45 µm syringe filter into an amber autosampler vial. Quantification was performed using the HPLC using the method described in Section 4.2. To determine if any residual RDX or TNT were present on the stir spatula, the spatula was rinsed with acetonitrile and run on the GC-ECD for trace analysis. No significant residuals were found on the spatula rinsates.

At the end of the test period, 100 mL of acetonitrile was added and the whole mixture was thoroughly shaken then sonicated at 10°C for 30 minutes. Then a 1 mL sample was removed, filtered into an amber autosampler vial for HPLC quantitation.

The Comp B contained 54% RDX, 6% HMX and 40% TNT. The maximum concentration of RDX in the slurry could reach 30 mg/L (~75% of C_{max}) if all the material dissolved. The maximum concentration of TNT in the slurry could reach 22 mg/L (~18% of C_{max}). Figure 18 shows the results from Comp B Slurry Test 1X where the RDX reached about two-thirds of the maximum and stayed constant over the test period. The TNT, however, initially reached up to the 80% of the maximum, but began to decline in concentration at a constant rate. The reason for RDX not reaching a greater concentration is not known, but this phenomenon was also observed in the preliminary dissolution kinetics test results (Phelan et al., 2002).

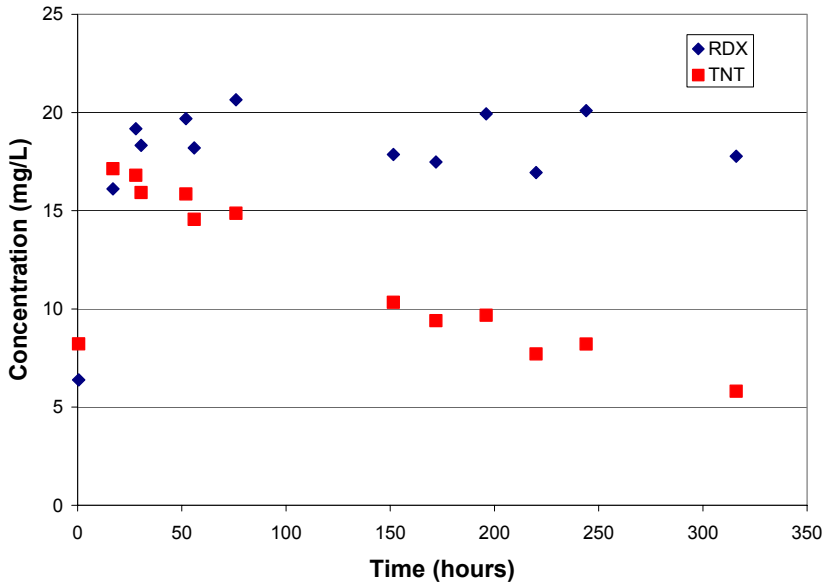

Figure 18. Slurry Test 1X Results

For the 5X slurry tests, the total RDX added would exceed the RDX water solubility if it became completely dissolved. Thus, the RDX should have shown near water solubility values of 40 mg/L; however, the RDX approached 30 mg/L, then began to decline slowly (Figure 19). Either degradation became prominent or the CompB dissolution was restrained by binders or other unknown mechanisms. If the TNT fully dissolved, it would have reached ~110 mg/L, which is close to the maximum solubility of

TNT at 118 mg/L (23°C). The TNT also did not reach this maxima, reaching only about 55 mg/L and then declining over several hundred hours to below detection limits. This major decline was clearly indicative of TNT degradation.

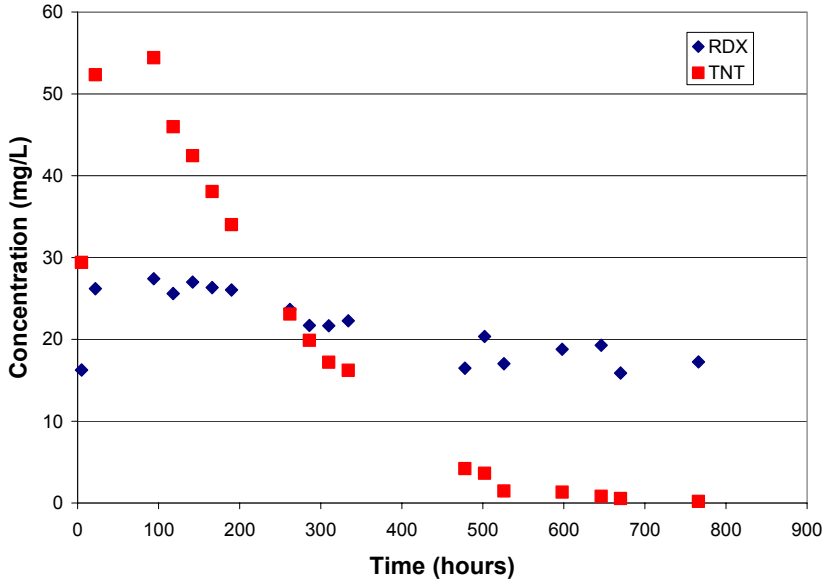

Figure 19. Slurry Test 5X Results

The 5X slurry samples were screened for the presence of amino-DNTs in addition to RDX and TNT. The conditions used to analyze RDX and TNT in the Comp B slurry samples would not resolve 2-amino-4,6-DNT nor 4-amino-2,6-DNT. Individual 2-amino and 4-amino DNTs were prepared at 50 ppm in DI, like the calibration standards for RDX and TNT, to obtain response factors.

Resolution of amino-DNTs was not possible under HPLC conditions utilized for RDX and TNT quantification. Thus, the peak at retention time of amino-DNTs (5.87-5.94 minutes) was evaluated as either all 2-amino DNT or as all 4-amino DNT.

The amounts of 2-amino and 4-amino-DNT were relatively small (accumulated values of 0.30 mg of 4-amino-DNT or 0.21 mg of 2-amino-DNT) and thus did not clarify why TNT recoveries were so low. It is possible conditions were appropriate for TNT degradation beyond the amino DNTs to products not quantified by the analytical method used.

Slurry Sacrifice Tests. For this test, 5.7 mg Comp B was mixed with 190 grams of glass beads and 100 mL of water in each of four separate containers. The containers were sacrificed by adding 100 mL of acetonitrile, thoroughly shaken then sonicated for 30 minutes at 10°C. A 1 mL sample was collected, syringe filtered and quantified by HPLC. Containers were sacrificed at time 0, 24, 72 and 216 hours.

The results from these tests showed that both RDX and TNT diminished at a constant rate. Figure 20 shows the zero order degradation plot and Figure 21 shows the first order degradation plot. Both of these show excellent linear correlation. Using the slope of the first order degradation plot, the calculated

half-life for RDX is 260 hours and for TNT is 115 hours. The slurry sacrifice test results clearly show a consistent degradation loss trend for both RDX and TNT that will support mass balance closure for the mass flux tests.

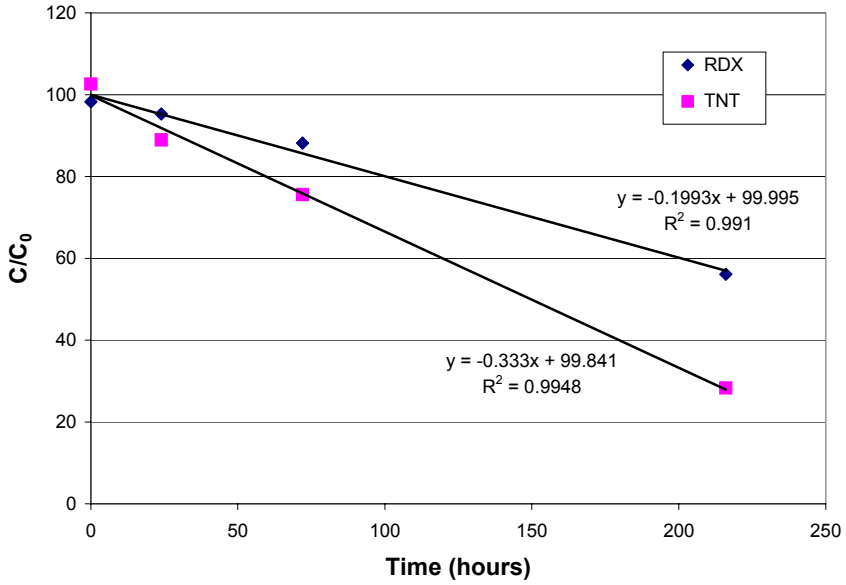

Figure 20. Slurry Sacrifice Test Results – Zero Order Degradation Plot

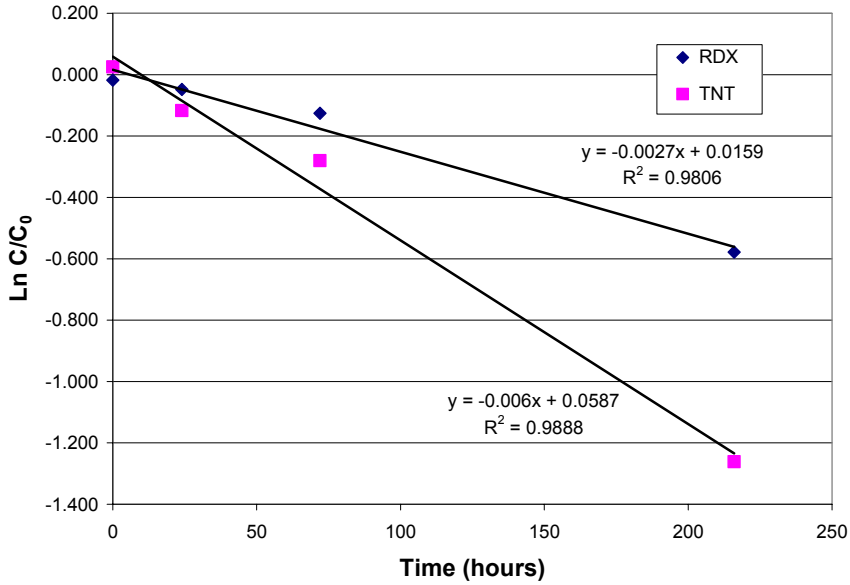

Figure 21. Slurry Sacrifice Test Results – First Order Degradation Plot

5.0 Experimental Results

Each set of experiments was performed to evaluate a specific mass transfer process. These included: particle size, bed loading/depth, low order detonation debris, temperature, flow rates, initial wetting rates, pulsed and steady flow, and water content (percent saturation). Twenty-four experiments were completed to date including two for unsaturated flow, nineteen for saturated conditions and three that failed (MT4, MT9, MT9b). The duration of the experiments varied from 3 days to 121 days. In some tests, the only a single variable was explored. In others, several parameter changes were changed in sequence to evaluate effects without rebuilding a new test cell.

5.1 Data Analysis Methods

C/C_{max}. Often the ratio of concentration values to their maximum temperature value (C_{max}) better describes data where small changes in temperature may influence the maximum capacity of the chemical in the water. As each effluent sample was collected, a temperature measurement was recorded using a thermocouple attached to the outside of the column and recorded with a datalogger. With this temperature, C_{max} was calculated for RDX and TNT using empirical data correlations shown in Table 12 and Figure 22 (Phelan et al, 2002).

Table 12. Aqueous Solubility Empirical Correlation

	Equation	a	b	c	r^2
TNT	$y = a+bexp(-x/c)$	20.176	36.295	-22.061	0.994
RDX	$y^{-1} = a+blnx$	0.0804	-0.0194		0.997

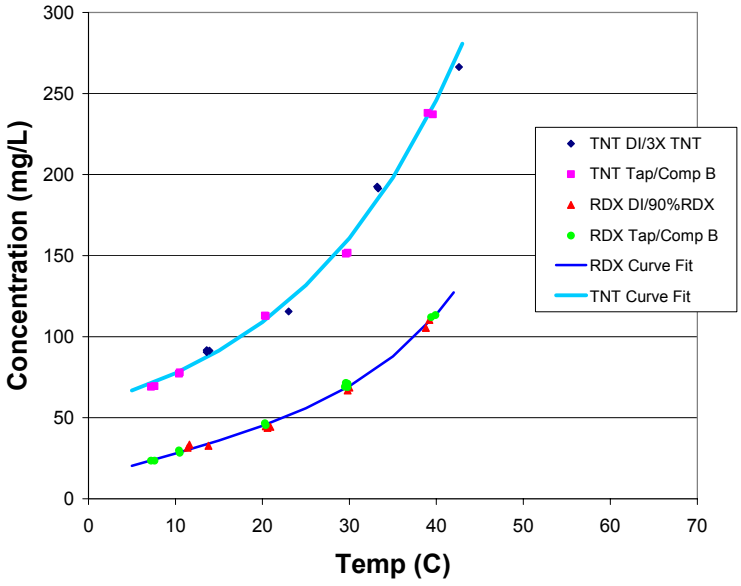

Figure 22. Compiled RDX and TNT Solubility Data

Cumulative Discharge. The cumulative discharge datum is another derived value that describes how much of the initial mass placed into the column has been discharged in the effluent. Concentration values with each aqueous effluent sample mass define a chemical discharge mass. When summed and referenced to the initial mass, the cumulative discharge defines the fraction of chemical mass discharged from the column. The charts for cumulative discharge use the total mass of chemical discharged from the column as the fractional basis – not the total mass placed into the column.

Pore Volume. The time duration of each test was transformed into pore volumes of water that had passed through the column. This was important for comparison of tests with differing water flux rates. The pore volume is determined from the bulk density and glass bead particle density and is about 20 mL for the saturated flow tests (small column) and about 90 mL for the unsaturated flow tests (large column).

Effluent Discharge Profiles. The effluent concentration versus time or pore volume plots show several characteristic features that were frequently encountered. A plateau of high effluent C/C_{max} was evident under certain conditions. This has been termed an excess mass capacity stage. At the end of this plateau, the effluent C/C_{max} began a decline that has been termed a mass depletion stage. The nature of the magnitude and duration of the excess mass capacity stage and the rate of decline of the depletion stage are described further in Section 7.0 Data Model Comparisons.

5.2 Effect of Bed Loading

In order to evaluate the performance of the various parameters, we explored the effects of energetic material loading in the column. The first few tests were run with a bed load of 25% CompB(100μm particle size)/75% glass beads in a bed depth of 0.5 cm. This ratio was later found to be an extreme excess, such that parameter influences on C/C_{max} and Cumulative Discharge were overwhelmed by the effect of bed loading.

The tests in this section explored impacts at much lower bed loadings. Table 13 shows the test parameters for 100 μm CompB particles where the bed loadings were reduced to ~ 2.5%, 0.25% and 0.05%. To vary the bed loadings with a constant bed depth (0.5 cm), the initial mass of CompB was reduced by a factor of 10 and 50.

Table 13. Test Parameters – Effect of Bed Loading

MT Test No.	6	7	8
Constant flow rate (ml/hr)	1.74	1.74	1.74
Bed depth (cm)	0.53	0.54	0.54
Initial RDX mgs	65.83	6.58	1.24
Initial TNT mgs	48.76	4.87	0.92
Loading (CompB) %	2.440%	0.250%	0.047%
Loading (RDX) %	1.317%	0.135%	0.025%
Loading (TNT) %	0.976%	0.100%	0.019%
Mass ratio to bed depth	1.293	0.136	0.025

The effect of bed loading on the RDX C/C_{max} is shown in Figure 23. In each case, the effluent C/C_{max} reached 0.8 to 0.9, and only the duration of the plateau of C/C_{max} declined with reduced initial bed loads. A similar patterned appeared for the TNT (Figure 24).

The cumulative discharge results (Figures 25 and 26) demonstrate the consistent mass transfer rate during the duration of the C/C_{max} plateau. The declining phases all begin after 90 to 95% cumulative discharge, indicating a rapid transition to low mass transfer in this phase. The asymptotic nature of the curves to 100% is an artifact of the calculation, where the reference maximum is the sum of all mass discharged from the column. Section 5.12 describes mass balance analysis that includes the cumulative mass discharged and the measured mass remaining in the column upon test sacrifice.

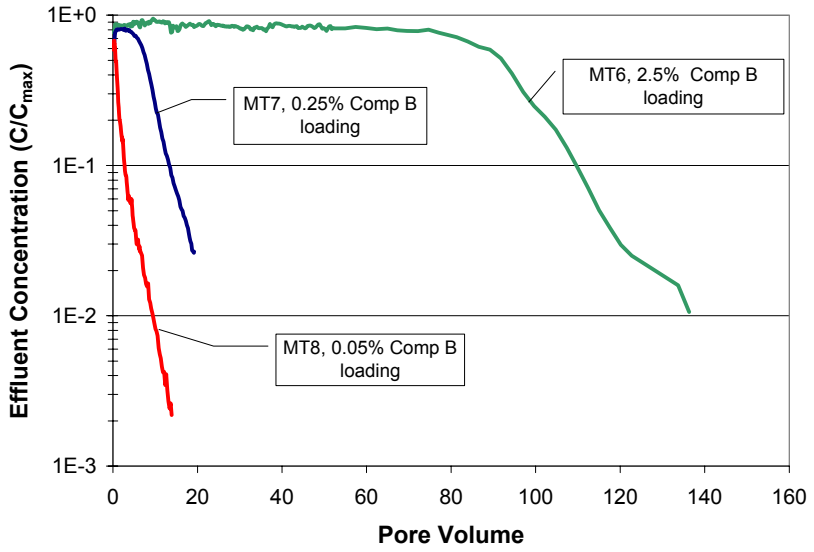

Figure 23. Effect of Bed Loading – Effluent Concentration (C/C_{max}), RDX

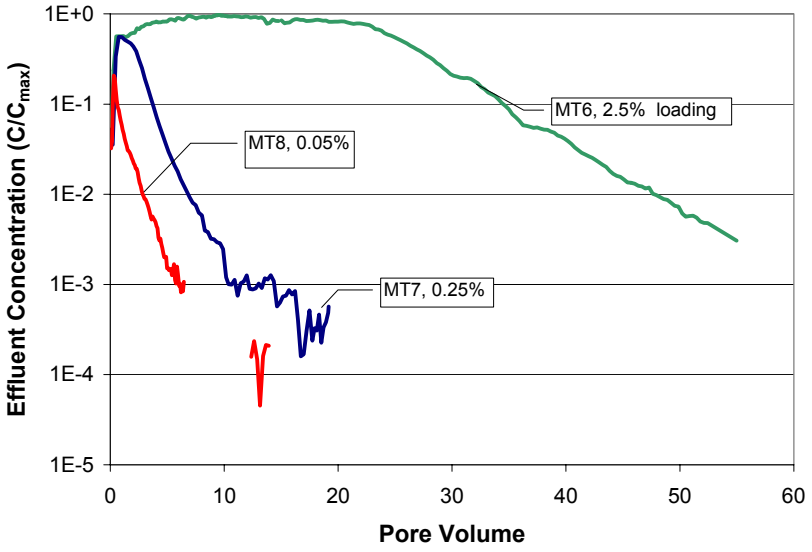

Figure 24. Effect of Bed Loading – Effluent Concentration (C/C_{max}), TNT

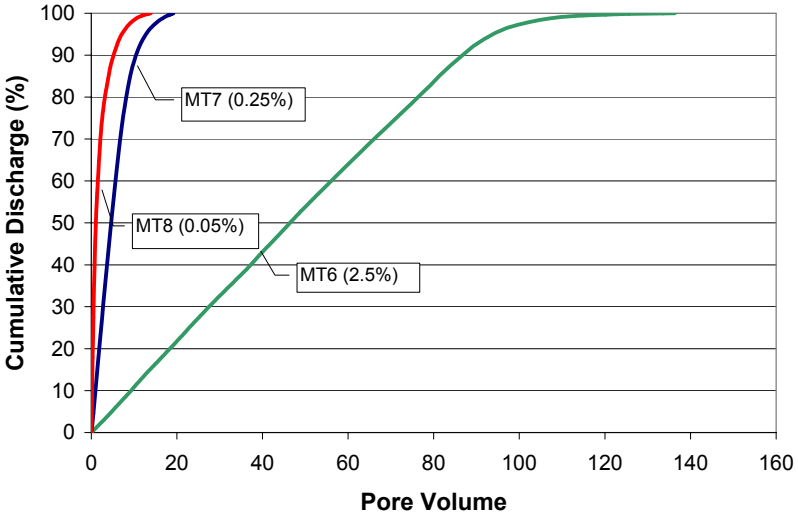

Figure 25. Effect of Bed Loading – Cumulative Discharge, RDX

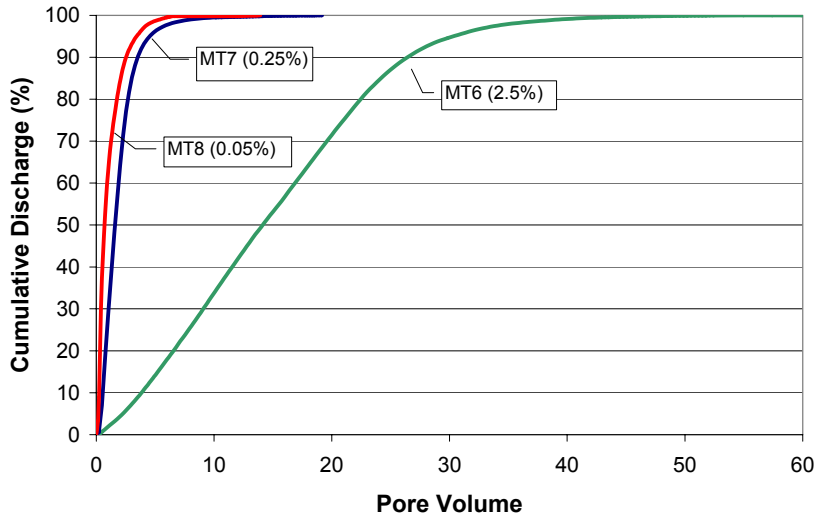

Figure 26. Effect of Bed Loading – Cumulative Discharge, TNT

5.3 Effect of Bed Depth

The results from the effect of bed load tests showed that the greater the mass, the longer the duration of the steady state mass transfer period. The next tests explored whether the same initial mass distributed in a short bed depth (0.5 cm) or a tall bed depth (2.75 cm) influenced the effluent concentration profile. In addition, this test evaluated variations in replicate test configurations.

Table 14 shows the test parameters for the effect of bed depth. Test numbers 8 and 8d are replicate tests with a short bed depth and test 9b2 is the tall bed depth. The results shown in Figures 27 and 28 indicate that for both RDX and TNT, the effect of bed depth did not significantly affect effluent concentration profiles. The results from the short bed depth replicates did show some variability in effluent concentration profiles and that more work is needed to better understand the variability of this test method. At this point, a decision was made to explore the nature of the principal mass transfer parameters before exploring in detail the variability of the process.

Table 14. Test Parameters – Effect of Bed Depth

MT Test	8	8d	9b2
Constant flow rate (ml/hr)	1.74	1.74	1.74
Bed depth (cm)	0.54	0.53	2.75
Initial RDX mgs	1.24	1.30	1.59
Initial TNT mgs	0.92	0.96	1.18
Loading (CompB) %	0.047%	0.049%	0.012%
Loading (RDX) %	0.025%	0.027%	0.007%
Loading (TNT) %	0.019%	0.020%	0.005%

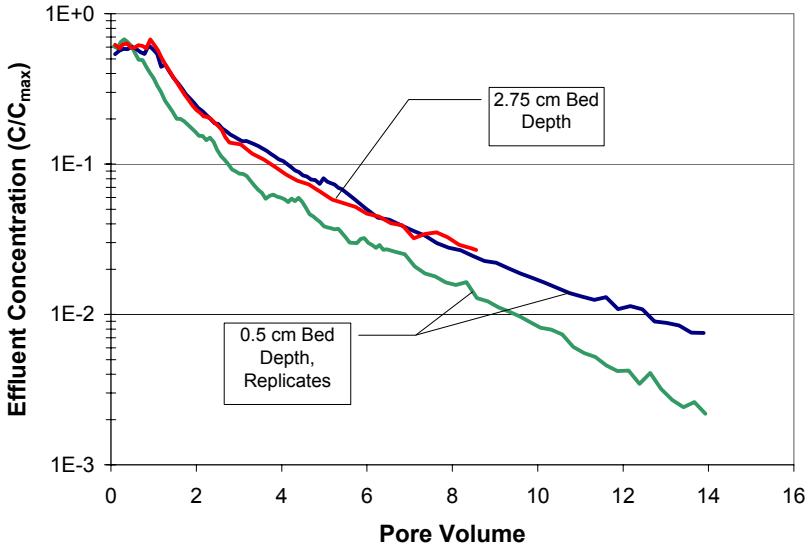

Figure 27. Effect of Bed Depth - Effluent Concentration (C/C_{max}), RDX

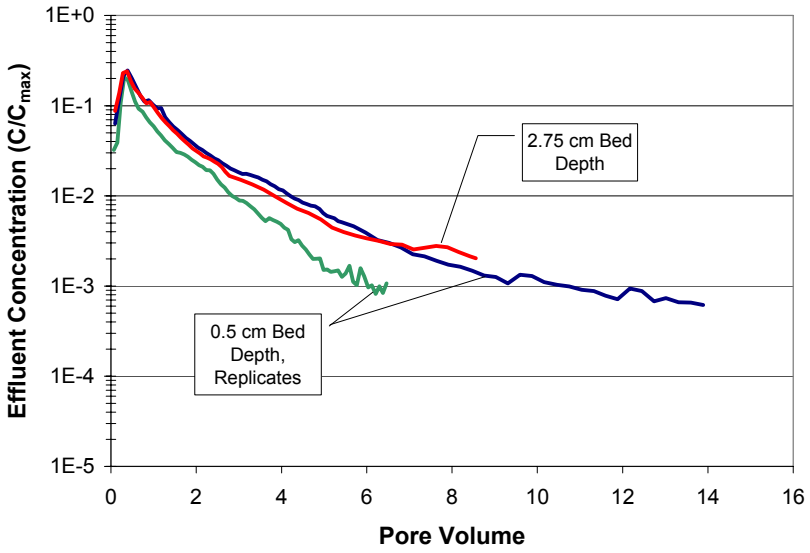

Figure 28. Effect of Bed Depth - Effluent Concentration (C/C_{max}), TNT

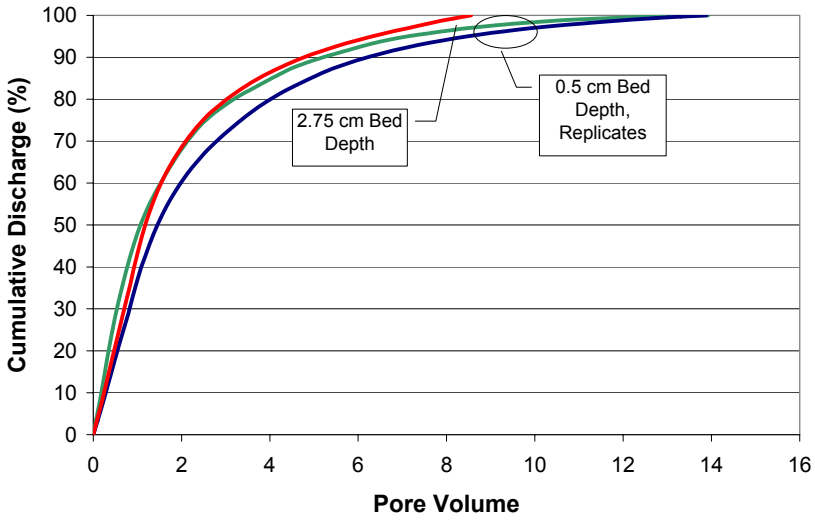

Figure 29. Effect of Bed Depth – Cumulative Discharge, RDX

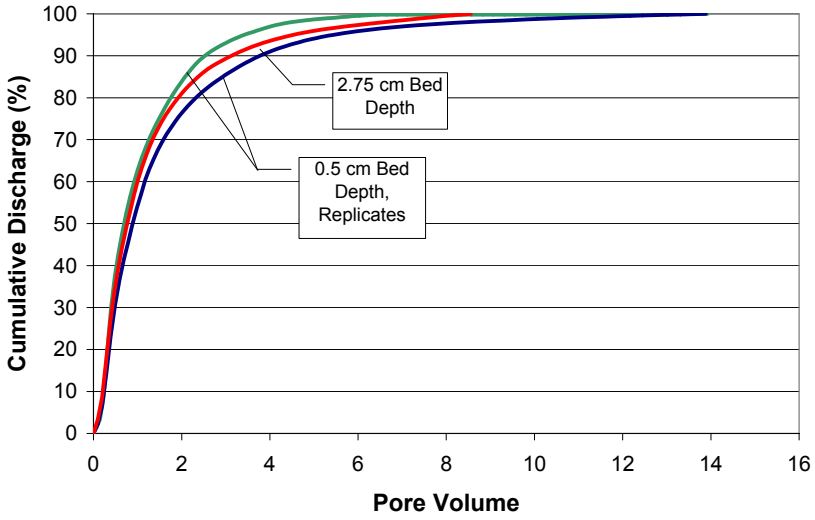

Figure 30. Effect of Bed Depth – Cumulative Discharge, TNT

5.4 Effect of Initial Mass

Section 5.2 showed an initial evaluation of the effect of bed load. Then Section 5.3 showed that the effect of bed depth was minimal and that the only factor seemed to be the initial mass loading. This section expands on the analysis of the effect of initial mass through a much larger range of values. Table 15 shows the initial masses from low, medium, high and very high. Note that the bed depths include both short and tall.

Table 15. Effect of Initial Mass

	Low Loading			Medium Loading	High Loading		Very High Loading
MT test	8	8d	9b2	10	7	9b3	6
Constant flow rate (ml/hr)	1.74	1.74	1.74	1.74	1.74	1.74	1.74
Bed depth (cm)	0.54	0.53	2.75	2.62	0.54	2.75	0.53
Initial RDX mgs	1.24	1.30	1.59	4.00	6.58	6.59	65.83
Initial TNT mgs	0.92	0.96	1.18	2.96	4.87	4.88	48.76
Loading (Comp B) %	0.047%	0.049%	0.012%	0.030%	0.250%	0.050%	2.440%
Loading (RDX) %	0.025%	0.027%	0.007%	0.016%	0.135%	0.027%	1.317%
Loading (TNT) %	0.019%	0.020%	0.005%	0.012%	0.100%	0.020%	0.976%

Figure 31 shows for RDX that the plateau of the C/C_{max} values lengthens as the initial mass increases. The peak C/C_{max} range from 60 to 90%, where the greater initial mass tests showed slightly greater peak C/C_{max} values. This may be a function of either unsteady state behavior in the early time frames or that the transition into the declining phase is gradual and interferes with achieving the peak C/C_{max} with the low initial mass tests. The slopes of the declining phase for each case are consistent indicating similar behavior for each case.

The results for TNT (Figure 32) show similar trends, but the peak C/C_{max} values are lower and the duration of the C/C_{max} plateau are shortened in each case compared to the RDX. The cumulative discharge results (Figures 33 and 34) show expected trends with the greater initial mass tests requiring greater pore volumes to reach the depletion stage.

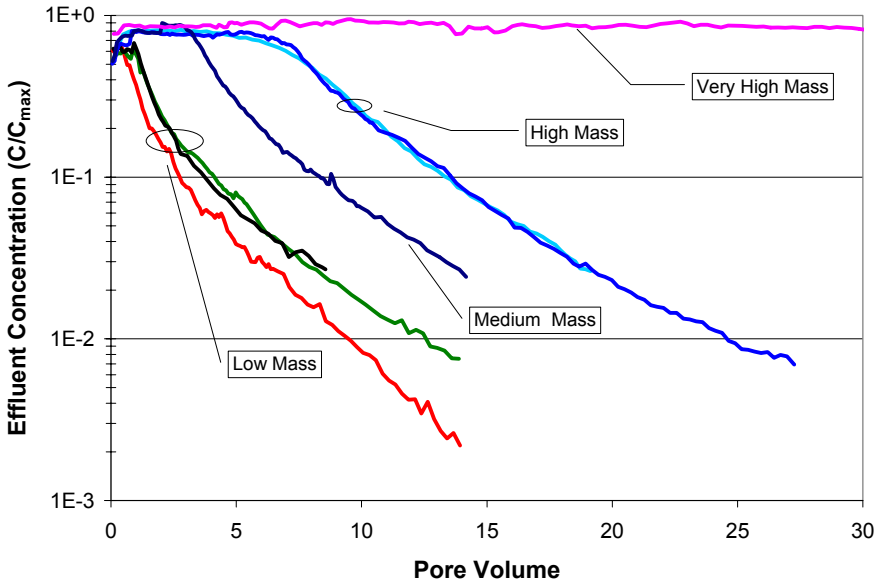

Figure 31. Effect of Initial Mass – Effluent Concentration (C/C_{max}), RDX

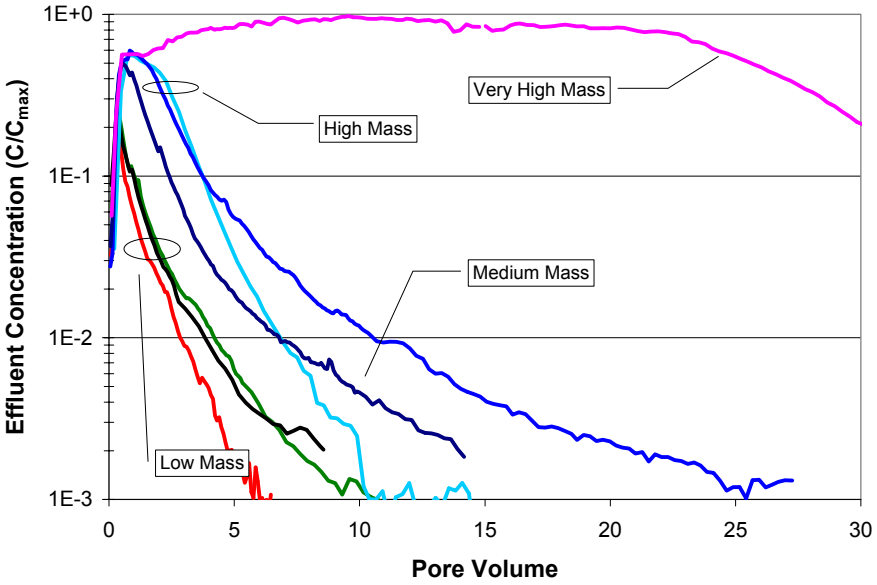

Figure 32. Effect of Initial Mass – Effluent Concentration (C/C_{max}), TNT

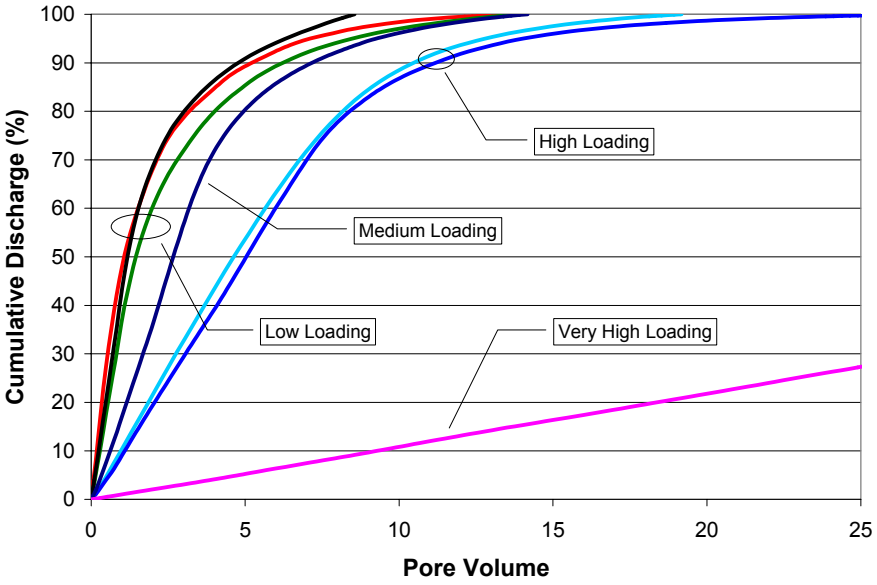

Figure 33. Effect of Initial Mass – Cumulative Discharge, RDX

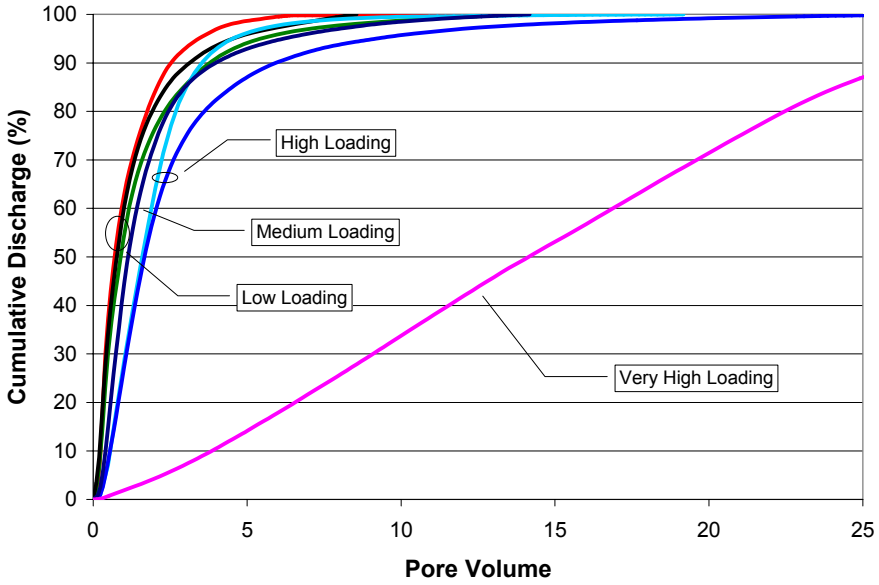

Figure 34. Effect of Initial Mass – Cumulative Discharge, TNT

5.5 Effect of Flow

The initial scoping tests (Tests MT1, MT2 and MT3) varied flow rates as part of initial screening tests for this project. These tests showed erratic results where an increase in flow initially caused a decrease in effluent concentration, but then rose gradually back to initial conditions. These tests were used bed loads of 25% CompB and may have caused preferential flow paths.

Table 16 shows three tests with a medium initial mass (~ 4 mg of RDX and 3 mg TNT) and a tall bed depth. The water flow rates were selected to be 20, 40 and 90% of the saturated hydraulic conductivity (K_{sat} = 0.8 cm/hr = 4 mL/hr) of the glass bead porous media. Values below K_{sat} were selected to mimic surface water infiltration without any significant ponding of water at the ground surface.

Table 16. Test Parameters – Effect of Flow

MT Test	14	10	13
Variable flow rate (ml/hr)	0.87	1.74	3.48
Bed depth (cm)	2.75	2.62	2.75
Initial RDX mgs	3.94	4.00	3.83
Initial TNT mgs	2.92	2.96	2.84
Loading (Comp B) %	0.030%	0.030%	0.029%
Loading (RDX) %	0.016%	0.016%	0.016%
Loading (TNT) %	0.012%	0.012%	0.012%

Figures 35 and 36 show an impact of water flow only on the mass depletion stage under these test conditions. The peak C/C_{max} values ranged from 60 to 90% with consistent plateaus for RDX and peak C/C_{max} for TNT in the range of 30 to 50% with no discernable plateau as noted previously in the medium initial mass tests (Section 5.2). The declining phases for RDX showed a trend with the slow flow test declining faster than the medium flow and the high flow; however, the TNT results were very similar.

The cumulative discharge charts show a trend for the RDX (Figure 37) with the slow flow showing a faster discharge rate until effluent concentration depletion compared to the medium and higher flow. However, the TNT (Figure 38) did not show this trend.

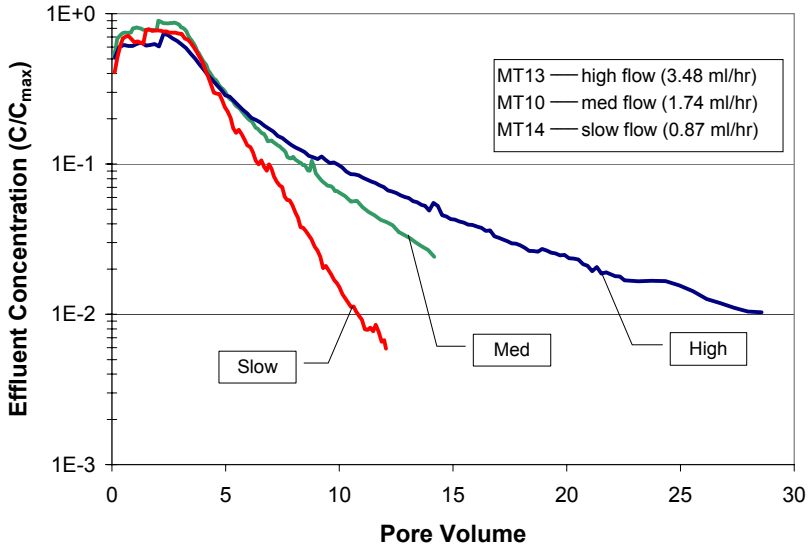

Figure 35. Effect of Flow – Effluent Concentration, RDX

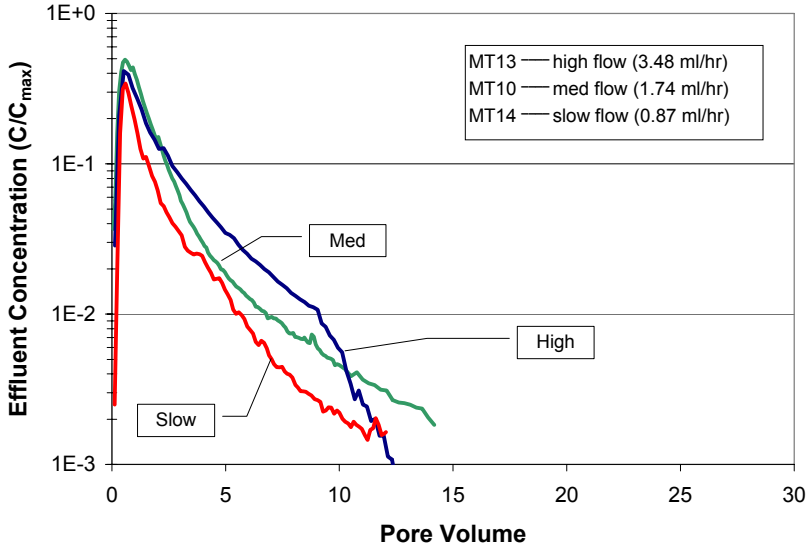

Figure 36. Effect of Flow – Effluent Concentration, TNT

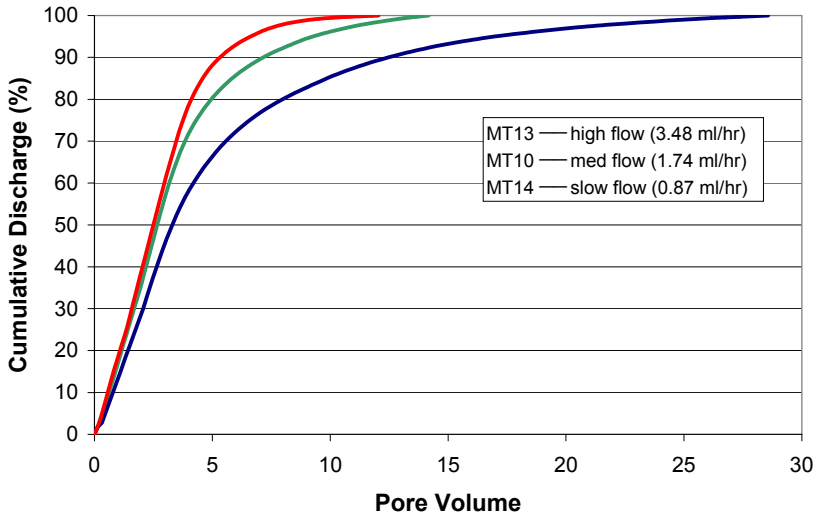

Figure 37. Effect of Flow – Cumulative Discharge, RDX

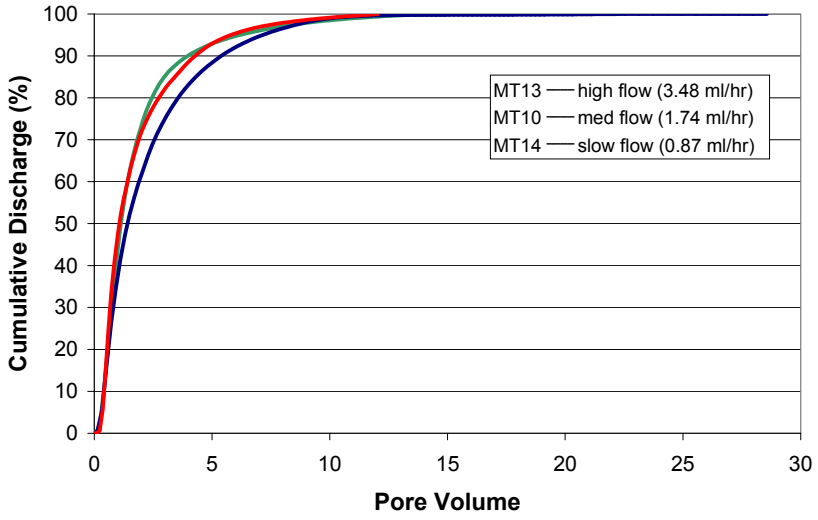

Figure 38. Effect of Flow – Cumulative Discharge, TNT

5.6 Effect of Temperature

The effect of temperature was explored in the early screening tests with the high initial mass. Figure 39 shows the results from Test No. 1. Notwithstanding the very high initial mass, the impact of temperature on the maximum water solubility of RDX and TNT is reflected in the very high concentrations found in the column effluents. Figure 39 shows effluent concentrations of RDX as a function of temperature at 5, 23, and 38°C. Figure 40 shows the RDX C/C_{max} values in the range of 80 to 100%.

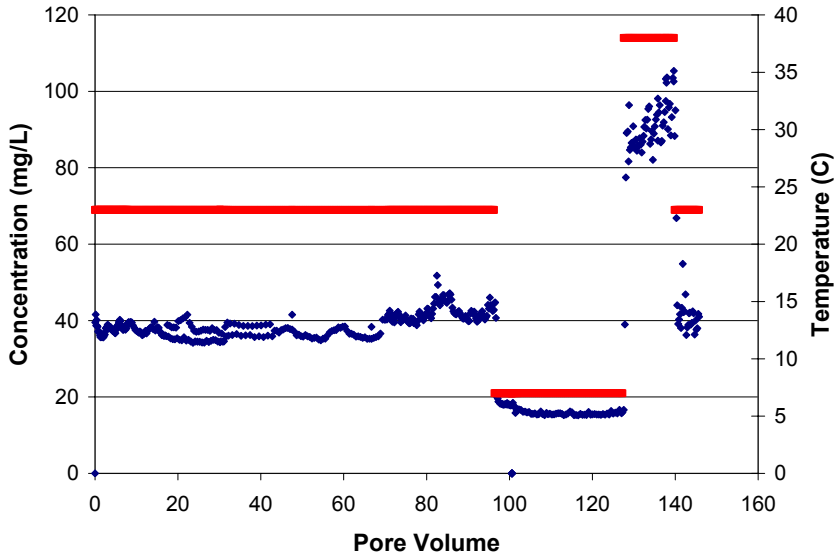

Figure 39. Effect of Temperature – Effluent Concentration, RDX

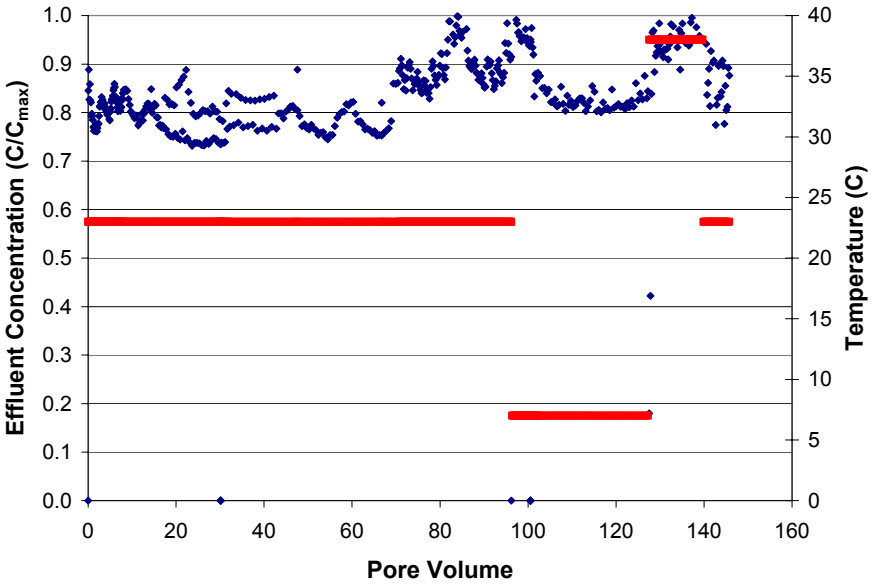

Figure 40. Effect of Temperature – Effluent Concentration, RDX C/C_{max}

Figure 41 shows similar trends in the column effluent concentrations of TNT. However, Figure 42 shows slightly lower C/C_{max} values at 23 and 38°C when compared to RDX. But, notably, the 5°C period showed C/C_{max} values at about 30 to 40%. Additional tests were considered to explore temperature effects in more detail, however, these were placed at lower priority compared to other tests.

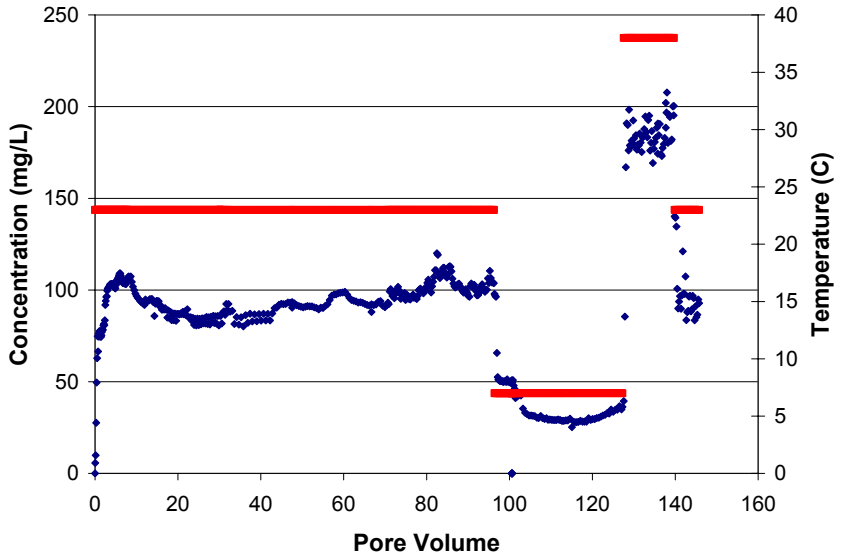

Figure 41. Effect of Temperature – Effluent Concentration, TNT

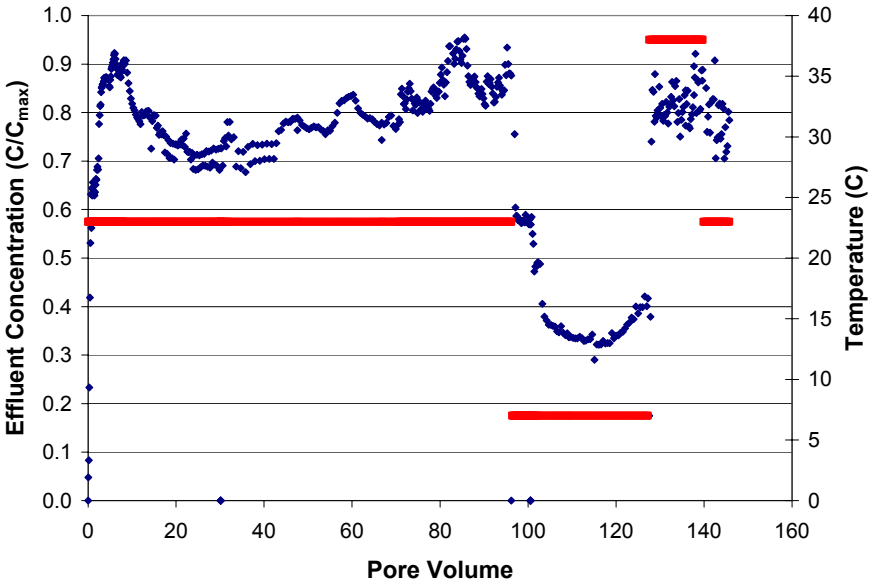

Figure 42. Effect of Temperature – Effluent Concentration, RDX C/C_{max}

5.7 Effect Of Energetic Material Particle Size

The effect of energetic material particle size was explored using the 100 µm and 1000 µm CompB size fractions. Table 17 shows the test variations evaluated in this section. Tests 8 and 10 used the 100 µm particles and were previously evaluated with the effect of initial mass. Test 8 was a low initial mass and Test 10 was a medium initial mass. Tests 16, 17 and 18 use the 1000 µm Comp B particles where the initial mass in Test 16 is equivalent to that in Test 10. Test 17 used 10 times more mass than Test 16 and Test 18 used about 50 times more mass than Test 16.

Figure 43 shows a comparison of these tests for RDX C/C_{max}. Tests 10 and 16 were prepared with nearly identical initial masses, but different particle sizes. In Section 5.4, equivalent initial mass values of the same particle size gave very similar results (Figure 31 and 32). However, similar initial mass with a ten-fold variation in particle size showed very different results. The large particles in Test 16 showed the influence of a very small initial mass, where the peak C/C_{max} was reduced with a shortened plateau. Increasing the mass of the larger particles in Tests 17 and 18 showed stepwise increases in the slope of the declining phase, however, none of the large particle tests sustained a high C/C_{max} plateau. Of note is the similarity in slopes of the declining phase for each set of CompB particle tests. The slopes for the larger particles are always lower than for the smaller particles. The results for TNT mimicked the RDX results. This result may indicate that 2-dimensional, number of particles, cross-sectional area and total surface area effects are important. At the time of this report, insufficient testing and analysis were completed to fully understand this effect.

Table 17. Test Parameters – Effect of Energetic Material Particle Size

MT Test	8	10	16	17	18
Bed depth	0.54	2.62	2.81	2.83	2.78
RDX mass (mg)	1.24	3.9	4.2	40.9	211.5
TNT mass (mg)	0.9	2.9	3.1	30.3	156.7
Diameter (µm)	100	100	1000	1000	1000
# of particles	1757	5577	6	58	299
Total particle x-sect. Area (cm^2)	0.14	0.44	0.05	0.45	2.35
ratio % (particle area/column)	3%	9%	1%	9%	46%
Total surface Area RDX (cm^2)	0.30	0.95	0.10	0.98	5.08
Total surface Area TNT (cm^2)	0.22	0.70	0.07	0.73	3.76

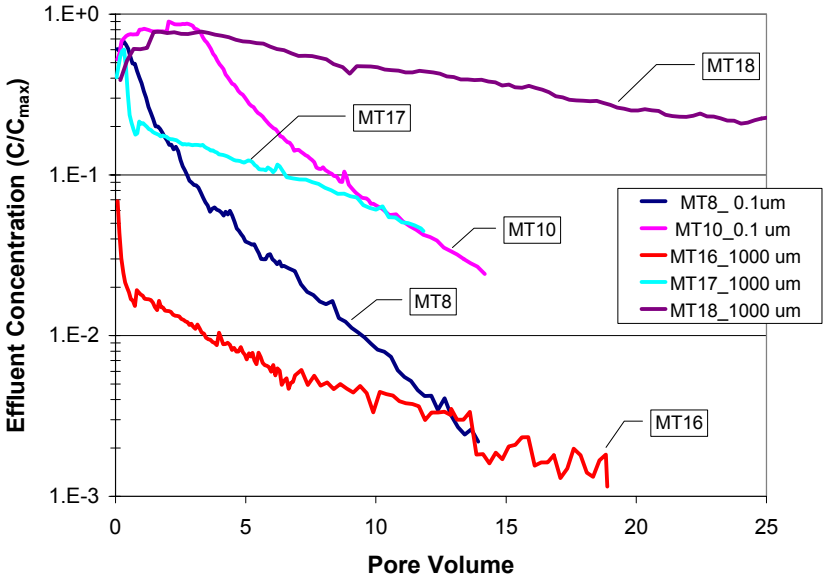

Figure 43. Effect of Energetic Material Particle Size – RDX C/C_{max}

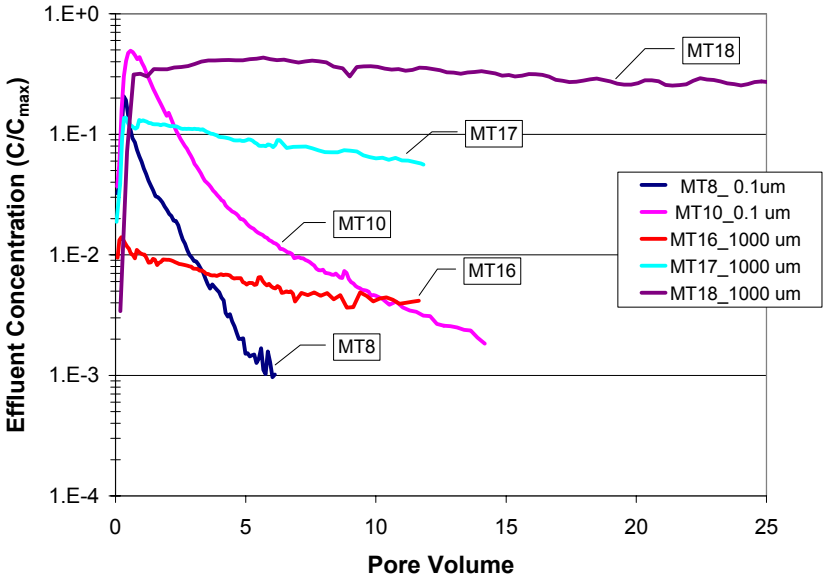

Figure 44. Effect of Energetic Material Particle Size – TNT C/C_{max}

5.8 Effect Of Initial Wetting Phase

For the low initial mass tests, some concern arose regarding the initial wetting of the column before discharge effluents were collected. The upflow tests were typically wetted slowly (0.8 mL/hr) over a period of about 24 hours. This procedure was started with the unsaturated flow tests to limit lifting and causing a hydraulic break in unsaturated conditions and carried over for consistency reasons for the saturated flow tests. During this slow wetting, mass transfer processes could have the opportunity to achieve greater C/C_{max} values before the depletion phase begins. Thus, a fast (1.7 mL/hr) initial wetting phase that equaled the continuous flow during the test and an intermediate (1.2 mL/hr) wetting phase were completed for comparison.

Table 18. Test Parameters – Effect of Initial Wetting Rate

MT test	8	8c	8b	8d
Wetting Flow (ml/hr)	~0.8	~1.2	~1.7	~0.8
Bed depth (cm)	0.54	0.52	0.55	0.53
Initial RDX mgs	1.24	1.23	1.30	1.30
Initial TNT mgs	0.92	0.91	0.96	0.96
Loading (Comp B) %	0.047%	0.047%	0.049%	0.05%
Loading (RDX) %	0.025%	0.025%	0.027%	0.027%
Loading (TNT) %	0.019%	0.019%	0.020%	0.020%

Figure 45 shows the effluent C/C_{max} results for RDX for this test group. These results show nearly identical peak C/C_{max} and plateau duration indicating that the effect of the initial wetting phase is not important under these test conditions. The results for TNT mimic that of RDX (Figure 46) and the

cumulative discharge charts for RDX (Figure 47) and TNT (Figure 48) also confirm little influence of the initial wetting phase.

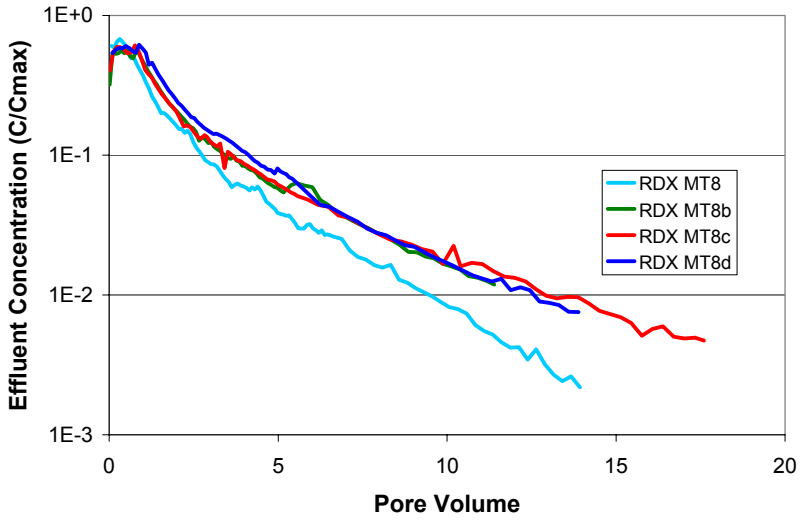

Figure 45. Effect of Initial Wetting Rate – Effluent Concentration, RDX

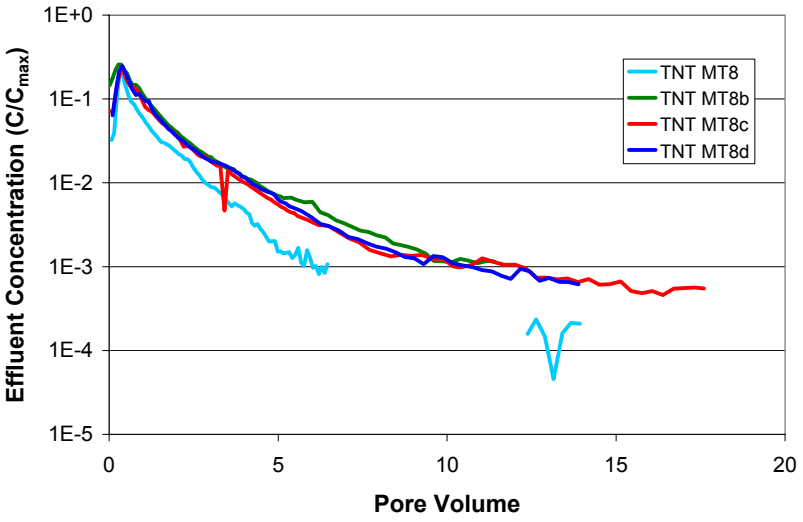

Figure 46. Effect of Initial Wetting Rate – Effluent Concentration, TNT

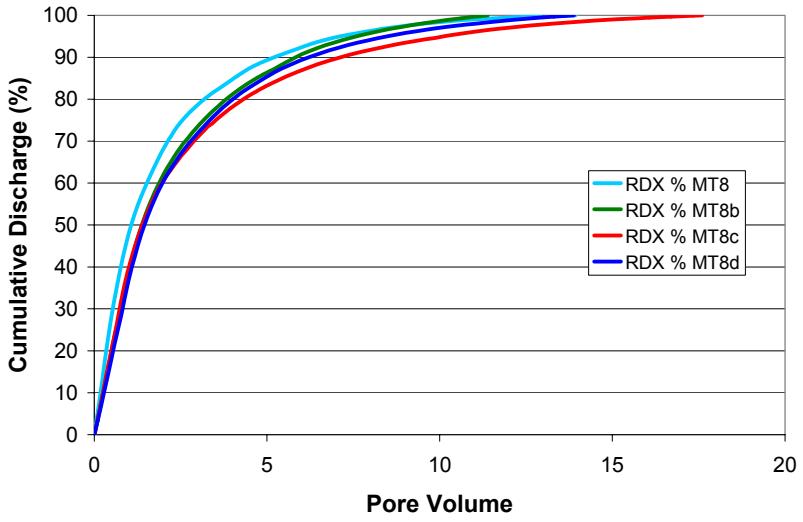

Figure 47. Effect of Initial Wetting Rate – Cumulative Discharge, RDX

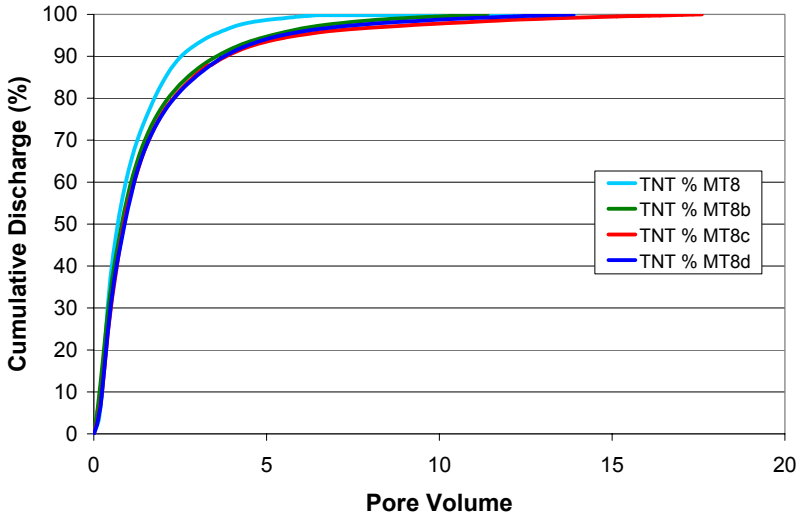

Figure 48. Effect of Initial Wetting Rate – Cumulative Discharge, TNT

5.9 Effect Of Porous Media Saturation

Unsaturated flow tests were more complicated to execute than the saturated flow tests. The unsaturated tests began with a slow wetting phase from the bottom of the column up to fully saturate the column and minimize entrapment of air. Figure 49 shows the data from the four tensiometers embedded into the side of the column. Tensiometer #4 is located at the bottom of the column and is first to show decreasing matric potential (increasing saturation). As the column becomes fully saturated, all four

tensiometers converge at about –50 cm tension, which is indicative of full saturation according to the moisture characteristic curve (Figure 11).

The column was then connected to the vacuum box containing the fraction collector. The box pressure was reduced to produce a column saturation of 0.80. The tensiometers responded quickly and achieved steady state values in about 1-2 hours. Water inflow was placed on the top of the column and the tests began. Effluent samples were removed from the vacuum box by switching a 3-way valve that maintained vacuum on the column and simultaneously relieving vacuum from the box.

The tests were run in sequential mode where a saturation value was maintained until effluent concentrations appeared at steady-state. Water inflow for each saturation level was matched to the unsaturated hydraulic conductivity at a specific saturation level (Figure 12). Table 19 shows the sequence of saturation and water flow for each stage of the test. Figure 50 shows the column saturation and effluent flux density over the duration of test MT5.

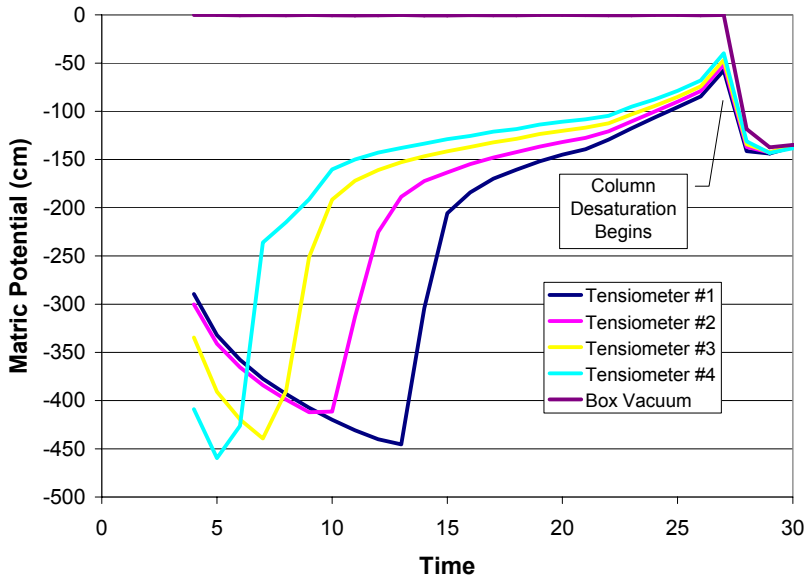

Figure 49. Column Wetting Phase – Matric Potential with Tensiometers

Table 19. Unsaturated Flow Test MT5 Saturation and Flow Schedule

Phase	Period (hours)	Water Inflow (mL/hr)	Saturation
Column Saturation	0 - 20	3.5	Up to 1.0
1	26 - 125	5.8	0.80
2	126 - 222	1.6	0.60
3	223 – 672	0.26	0.40
4	673 - 1204	1.6	0.60
5	1205 - 1518	0.26	0.40
6	1519 - 1746	1.6	0.60

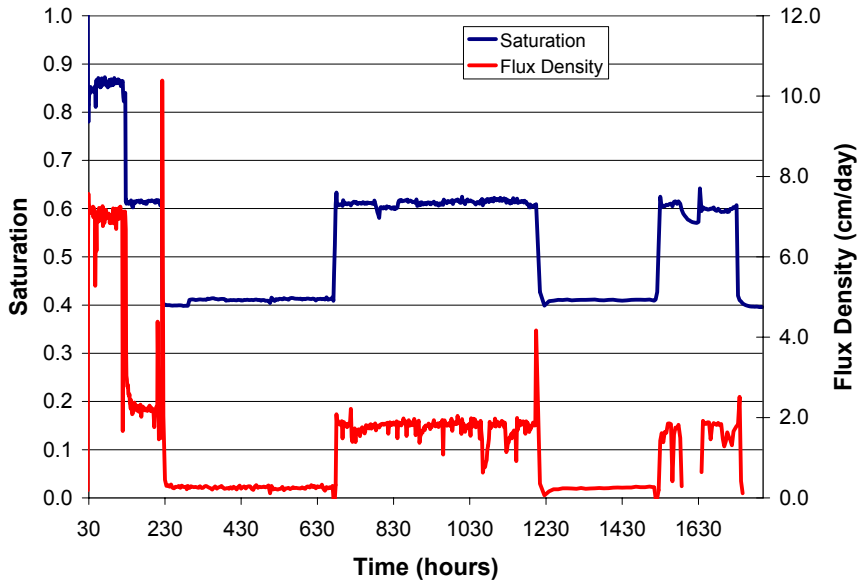

Figure 50. Column Saturation and Effluent Flux During Unsaturated Flow Test MT5

The effluent concentration of RDX at each saturation level is shown in Figure 51. In the early part of the test with saturation levels of 0.80 and 0.60, the RDX C/C_{max} remained high at values typical of the saturated flow tests (0.80 to 0.90). The rising trend during this period may be related to natural variability of the experimental system and not a function of changes in saturation. When the column was lowered to a saturation of 0.40, the RDX effluent C/C_{max} declined over several hundred hours to a steady-state level of about 0.40 with a range of 0.30 to 0.50. When the saturation was raised back up to 0.60, the RDX effluent C/C_{max} rose back to the range of 0.80 to 0.90. To verify the effect of changing saturation from 0.60 to 0.40, the column saturation was reduced to 0.40. Again, the RDX effluent C/C_{max} declined at a similar rate as the previous change. However, the steady-state C/C_{max} appeared to stabilize at about 0.75. The column saturation was then increased to 0.60 again and the RDX effluent C/C_{max} increased again. At this time, water inflow was interrupted due to equipment failure. When the test resumed, the RDX effluent C/C_{max} showed a return to the 0.80 to 0.90 range.

Figure 52 shows the results for TNT and indicates the same general response. However, in the transition from 0.80 to 0.60 saturation, the TNT effluent C/C_{max} declined from 0.70 to 0.50 – whereas the RDX effluent C/C_{max} remained steady. The TNT effluent C/C_{max} also appeared slightly lower than that of RDX. At the 0.40 saturation, the TNT effluent C/C_{max} was near zero. After the transition from a saturation of 0.40 to 0.60, the TNT increased just as the RDX, however, the TNT effluent C/C_{max} began to decline. This decline may have been the start of the declining phase were insufficient mass was now available to sustain the high C/C_{max} values. At the end of the MT5 unsaturated flow test, a pulsed water flux test was started and is described in Section 5.10.

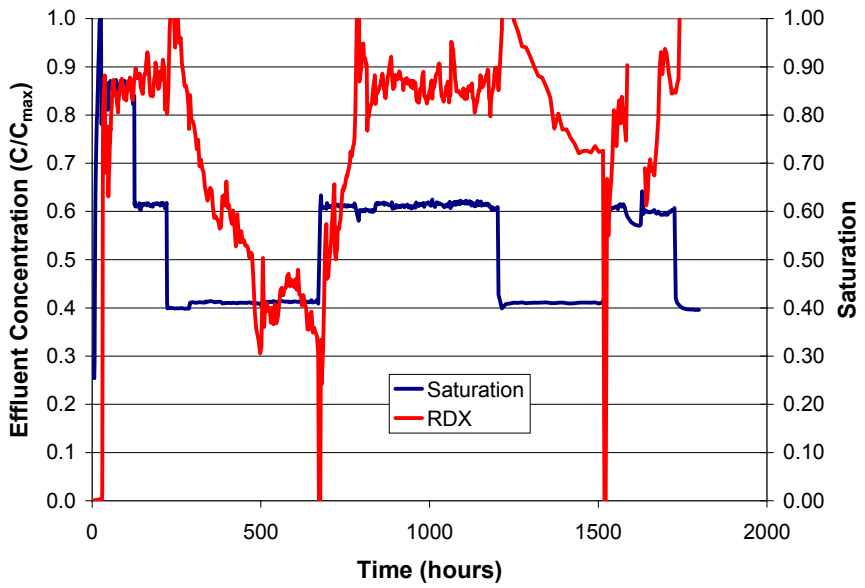

Figure 51. Effect of Porous Media Saturation – Effluent Concentration, RDX

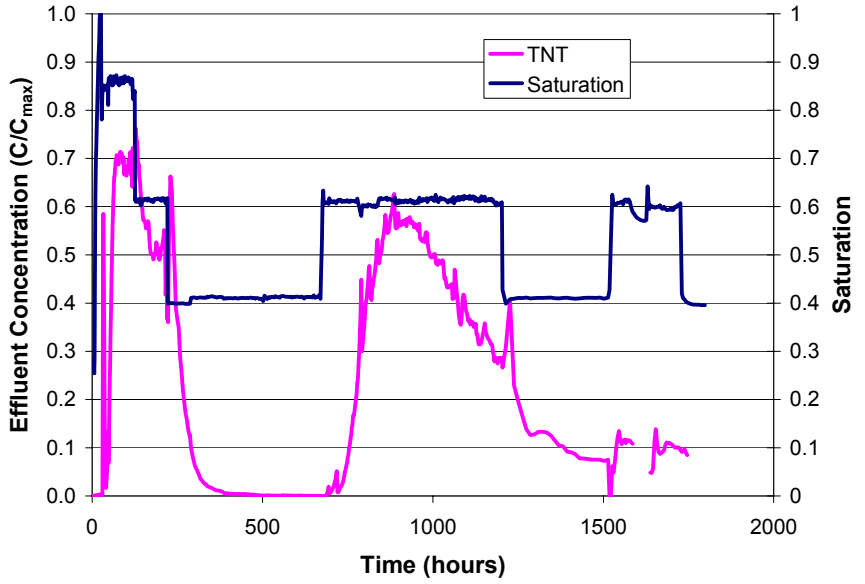

Figure 52. Effect of Porous Media Saturation – Effluent Concentration, TNT

The results of the unsaturated flow tests indicate that pore saturation level is not important until saturation drops below 0.60. At a saturation of 0.40, the effluent concentrations of RDX and TNT dropped significantly. The saturation effect on effluent C/C_{max} could be interpreted as a bypass flow issue, where at low saturation some of the CompB particles that are located in large pore spaces are not in contact with flowing water. To evaluate this effect, the maximum pore size filled with water was

estimated based on capillary bundle theory. The matric potential of the porous media is assumed to be equivalent to the height of water rise in a capillary tube. The height of water rise in a capillary tube is

$$\psi_m = h = \frac{-2 \cdot \sigma}{r \cdot \rho_w \cdot g} \quad [8]$$

where ψ_m is the matric potential (m), σ is the surface tension of water (7.2E-2 kg/s^2), ρ_w is the density of water (1000 kg/m3) and g is the acceleration due to gravity (9.8 m/s^2). Table 20 shows the saturation, matric potential and equivalent radius of the maximum pore size filled. The CompB particles used in this test were the 100 µm size fraction. From Table 20, even at a pore saturation of 0.80, the CompB particles are about 10 times greater than the maximum pore size filled with water. This phenomena will need to be evaluated in more detail along with other 2-dimensional effects such as bed load and Comp B particle size.

Table 20. Saturation, Matric Potential and Equivalent Pore Radius

Saturation (S_l)	Matric Potential (ψ_m)	Equivalent Radius (r_{max})
0.80	-135 cm	10 µm
0.60	-185 cm	8 µm
0.40	-270 cm	5 µm

The time needed to reach a new steady state after a change in porous media saturation was very long (i.e. days). Natural soil systems would not remain at these intermediate saturation levels for such long periods of time and would normally be either fully saturated or at residual saturation. Therefore, pulsed water flow tests were completed to better mimic the continuum of saturation conditions during periodic rainfall events.

5.10 Effect Of Pulsed Water Flow

The pulsed water flow tests used the same unsaturated flow columns and test equipment as described in Section 5.9. Pulsed test MT5 was initiated at the end of the unsaturated flow part of test MT5. Two sets of pulse tests were completed with the MT5 column – one with a baseline porous media saturation of 0.40 and one at 0.80. Since the pulsed test portion of MT5 was started after a prolonged unsaturated flow test (~1750 hours), pulsed test MT12 was started with a fresh column. The MT5 column bed load was ~ 2.5% and the MT12 column bed load was ~ 0.25%. The baseline porous media saturation for MT12 was set at 0.40.

A set of pulsed tests was configured to place the same total volume of water into the column at a slow, medium and fast flow rate. The flow duration was varied to produce the same total volume of inflow water. The water pulse occurred once per day with five repetitions (Monday through Friday). The column rested at the baseline saturation for two days (Saturday and Sunday) with no water inflow. Thus, the duration for each set of pulse tests was three weeks. Table 21 shows the flow rate and duration for

each set of water inflow pulses. These were selected based on the maximum saturated conductivity (K_{sat}) of the porous media (0.86 cm/hr), ~40% of the K_{sat} and ~10% of K_{sat}.

Table 21. Pulsed Test Water Inflow

Pulse Rate (cm/hr)	Pulse Duration (hr)	Total Pulse Volume (mL)
1	1	20
0.33	3	20
0.1	10	20

Figure 53 shows the column matric potential for Tensiometer #1 (5 cm below the top) during pulse test MT5. The first set of three pulse repetitions is with a baseline saturation of 0.40 and the second set is for a baseline saturation of 0.80. From a baseline saturation of 0.40, the top tensiometer rises much more so than from a baseline saturation of 0.80 because of the steeper gradient on the moisture characteristic curve (Figure 11). During the second set of pulses the 1 cm/hr:1 hr pulse reaches matric potentials that indicate saturated conditions for brief periods of time.

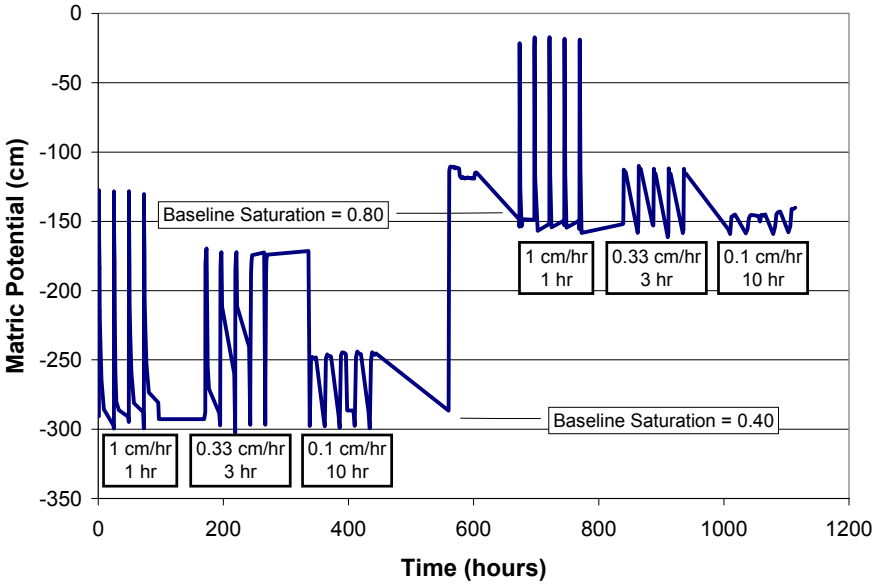

Figure 53. Column Matric Potential (Tensiometer #1) During Pulse Test MT5

Figure 54 shows the column matric potential during pulse test MT12. These are very similar to the first set of pulse tests for MT5 except that the 1cm/hr:1 hr pulse on MT12 was not greater than the 0.33 cm/hr:3 hr pulse that was observed in MT5.

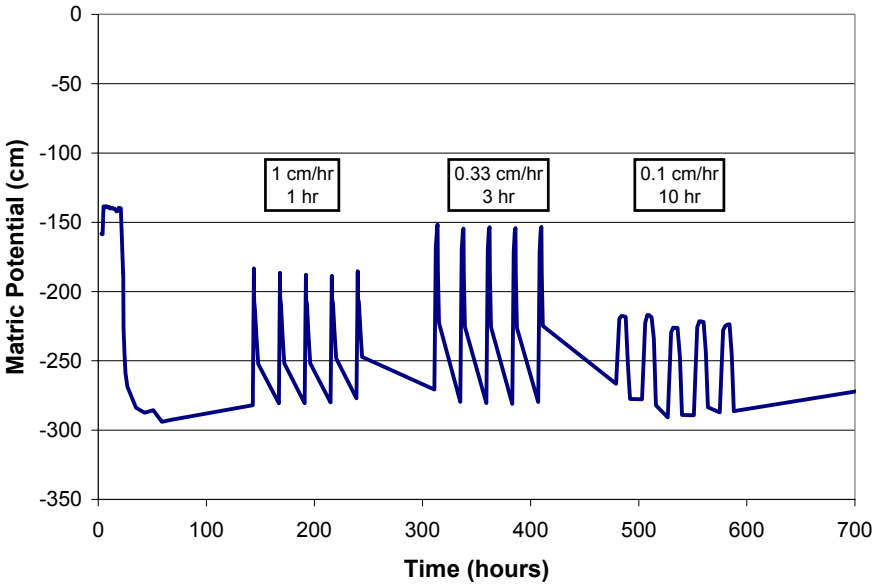

Figure 54. Column Matric Potential (Tensiometer #1) During Pulse Test MT12

Column effluent C/C_{max} for both RDX and TNT in both MT5 and MT12 are shown in Figure 55. The RDX effluent C/C_{max} for MT 5 during both set of pulse tests remain high at about 0.80 to 0.90. The TNT effluent C/C_{max} shows a declining trend at about a factor of ten below that of RDX; however, this was also evident at the end of the MT5 unsaturated flow test period.

Test MT12 used a factor of ten less CompB in the bed load (~0.25% vs ~2.5%) compared to MT5. The RDX effluent C/C_{max} was slightly lower (~0.50 to 0.70); and, whether this was a result of the decreased bed load is not certain. The TNT effluent C/C_{max} showed similar trends as the TNT in MT5, where the levels were about a factor of ten less than that of RDX and also showed a declining trend over time.

These pulse tests better mimic natural field conditions than the saturated flow tests. Periodic water inflow shows that RDX effluent C/C_{max} remains high (0.50 to 0.90), depending on the bed loading. This provides evidence that periodic rainfall can produce relatively high concentrations of RDX from small CompB particles.

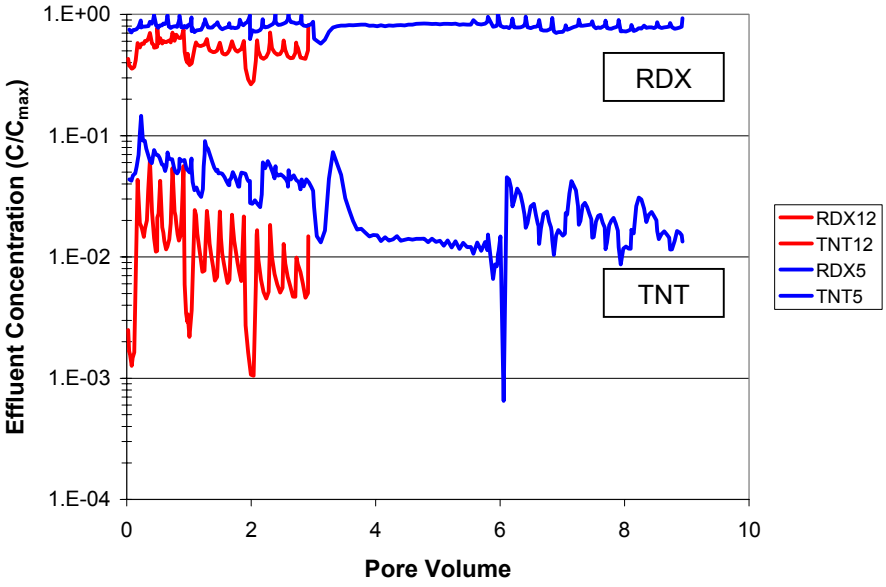

Figure 55. Effect of Pulsed Water Flow – Effluent Concentration (C/C_{max}), RDX and TNT

Moisture content check. A test was performed to evaluate the relationship of the moisture characteristic curve to the conditions in the column. At the end of MT5 pulse test, three samples of glass beads were collected from the top of the column, adjacent to tensiometer #1 (Figure 56). Gravimetric moisture content was determined by the oven drying method.

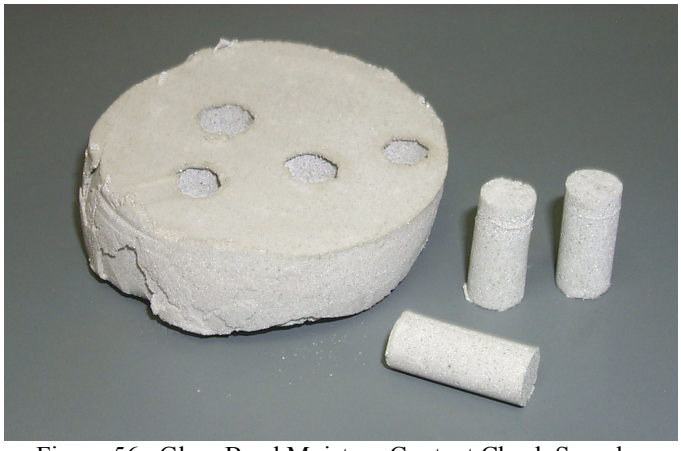

Figure 56. Glass Bead Moisture Content Check Samples

Results from the gravimetric moisture content measurements showed all three samples to be about 0.09 g/g. With a glass bead bulk density of 1.95 g/cm^3, the saturation was calculated to be about 0.80. At the end of test MT5 pulse, tensiometer #1 was showing a value of –140 to –150 cm tension. This corresponds to a moisture content of 0.79 to 0.73 g/g (Figure 11), which is in good agreement with the measured moisture content of 0.80.

5.11 Low Order Detonation Debris

Low order detonation tests were completed at NAVEODTECHDIV at Blossom Point, MD under the direction of SERDP Project CP-1155 (Pennington and Jenkins). Sandia received four samples collected after a series of low order detonations were completed. Each sample contained about 5 grams of material. Table 22 shows the results of a 0.8 g/4 mL sample:acetonitrile extract analysis.

Table 22. Detonation Debris Analytical Results – Discrete Samples (µg/g)

Location	RDX	TNT
Ground Zero	380	13335
#1 Spot	120	85
#2 Spot	325	1930
#3 Spot	27	445

These results showed the presence of RDX and TNT, but not at extremely high levels expected from low order detonations. However, when compared to Figure 4, any RDX above about 30 to 70 µg/g is very likely to have solid phase energetic material (see Section 2.0).

Two tests were completed with the low order detonation debris. One used only material from the Ground Zero location (MT11). The second test used material combined from Ground Zero and #2 Spot (MT 15). Using a weighted average approach to estimate the RDX and TNT concentration for this combined sample, the RDX was expected to be 352 µg/g and the TNT 7632 µg/g. Table 23 shows the results of four subsamples (0.8 g:4 mL acetonitrile extracts) of the combined material. These results demonstrate the heterogeneous nature of low order detonation debris.

Table 23. Detonation Debris Analytical Results – Combined Sample

Subsample No.	1	2	3	4
TNT (µg/g)	11508	16718	16134	5945
RDX (µg/g)	188	112	104	66

Table 24 shows a summary of the test parameters for the two tests containing the low order detonation debris, and one test (MT8) that contained a similar initial mass of RDX.

Table 24. Effect of Low Order Detonation Debris

MT Test No.	11	15	8
Test Series	1	2	1
Constant flow rate (ml/hr)	1.74	1.74	1.74
Bed depth (cm)	2.76	0.57	0.54
Initial RDX mgs	0.13	1.71	1.24
Initial TNT mgs	4.38	33.65	0.92
Loading (CompB) %	0.018%	0.720%	0.047%
Loading (RDX) %	0.001%	0.035%	0.025%
Loading (TNT) %	0.018%	0.685%	0.019%
Mass ratio to bed depth	0.050%	0.412%	0.025

Figure 57 shows the RDX effluent C/C_{max} results. The results for the low order detonation debris follow a similar pattern as the Effect of Initial Mass (Figure 31). There is no C/C_{max} plateau because even the 1.74 mg RDX is in the low initial mass region where the CompB particles showed no C/C_{max} plateau. The slopes of declining phase for both low order detonation debris tests were very similar and somewhat less than for the comparable CompB particle test. This lower slope for the low order detonation debris may be a result of the presence of soil particles in the bed, providing sorption sites and delaying mass transfer into the glass beads.

Figure 58 shows the TNT effluent C/C_{max} results that follow the same patterns as the RDX. Since the TNT initial mass was much greater than the RDX, the TNT shows higher effluent C/C_{max} initially, but as has been observed in many of the other tests, the TNT quickly declines in concentration.

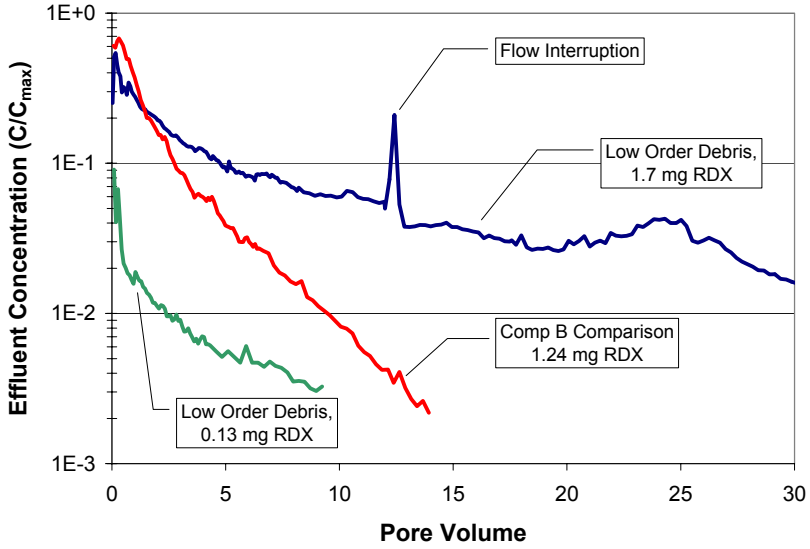

Figure 57. Effect of Low Order Detonation Debris – Effluent Concentration C/C_{max}, RDX

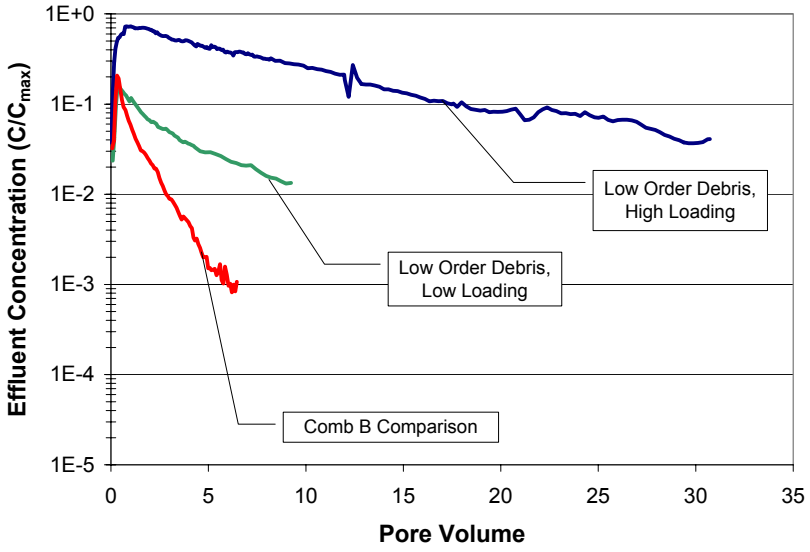

Figure 58. Effect of Low Order Detonation Debris – Effluent Concentration (C/C_{max}), TNT

5.12 Mass Balance

At the end of each test (starting with test number 5), the amount of RDX and TNT remaining in the column was measured. The contents of the column were removed and placed into a large sample container. A 1:1 sample mass to acetonitrile volume mixture was sonicated overnight at 10°C. A 5 mL sample of the extract was collected, filtered through a 0.45 µm syringe filter, and quantified on the GC/ECD. The total mass of RDX and TNT remaining in the column at the end of the test was determined and shown as the extraction row in Table 25. The effluent row is the sum total mass of RDX or TNT in the effluent as measured in each effluent sample.

The results in Table 25 show that mass balance results were generally very good. RDX values ranged from 59% to 95%, with two anomalous values over 100%. Most of the mass balance results were in the 80 to 90% range, which is very good because degradation was not accounted for in the estimate. TNT values ranged slightly lower, from 36% to 89%.

Table 25. Mass Balance of RDX and TNT

RDX Mass Balance: Cumulative %																							
Source	1	2	3	5	6	7	8	8b	8c	8d	9	9b	9b2	9b3	10	11	12	13	14	15	16	17	18
Efluent**	17	31	19	36	91	88	81	85	76	88	21	78	77	91	91	57	55	78	81	126	3	4	8
Extraction	na	na	na	50	0	4	2	6	3	3	55	8	6	3	5	52	3	10	6	47	92	84	62
Total	17	31	19	86	92	92	83	91	79	91	76	86	83	93	96	109	59	88	87	174	95	88	70

TNT Mass Balance: Cumulative %																							
Source	1	2	3	5	6	7	8	8b	8c	8d	9	9b	9b2	9b3	10	11	12	13	14	15	16	17	18
Efluent**	52	75	59	42	89	56	39	68	47	52	42	51	44	61	58	20	10	50	33	49	8	9	20
Extraction	na	na	na	2	0	1	1	1	3	1	4	4	3	1	3	14	0	6	3	5	65	70	53
Total	52	75	59	44	89	57	40	70	50	53	46	55	47	63	60	35	10	56	36	54	74	79	74

** based on total mass in for RDX and TNT (CompB particles)

Degradation is believed to occur only in the liquid phase. The CompB is unlikely to undergo degradation as a solid phase and the any sorbed amount would be unavailable for degradation. The total

mass degraded is proportional to the residence time of the analytes from release by the bed to collection as an effluent. For example, tests run at the saturated hydraulic conductivity of the glass beads (2.3E-4 cm/sec), the residence time for half the column height is about 9 hours. Effluent samples analyzed repeatedly over time show no significant difference – indicating that degradation is not taking place outside of the column environment. To estimate the mass lost to degradation, the degradation rates described in Section 4.7 could be used with the experiment duration shown in Table 26. Using a first order degradation rate for RDX (Figure 21), a 9 hour residence time indicates a 1% loss in concentration. Additional work is needed to complete this analysis.

Table 26. Experiment Duration (hours)

MT Test No.	1	2	3	5	6	7	8	8b	8c	8d	9	9b	9b2	9b3	10	11	12	13	14	15	16	17	18
Duration (hrs)	1001	1139	857	2914	1410	228	164	137	175	145	75	196	95	313	166	107	1918	146	292	471	303	149	441

6.0 Model Development

In order to simulate the mass transfer tests, modifications were made to the T2TNT code (Webb et al., 1999). A separate solid phase and mass transfer from the solid phase to water were added to the code. The details of the mass transfer model are discussed below.

6.1 Mass Transfer Formulation

The mass transfer rate from a solid to the surrounding fluid is given by:

$$\dot{m} = k\, A_i\, S_\ell\, \rho_f \left(C_s - C\right) \qquad [9]$$

where $\dot{m}$ is the mass transfer rate from the solid to the liquid phase (kg/s), k is the mass transfer coefficient (m/s), A_i is the solid phase interfacial area (m^2), S_ℓ is the liquid saturation, ρ_f is the fluid density (kg/m^3), C is the concentration of the solid material in the far-field fluid (mass fraction), and C_s is the saturation concentration of the solid material in the fluid (mass fraction). In equation [9], the mass transfer from the solid mass to the liquid phase is calculated. The liquid saturation, S_ℓ, is included to account for the wetted solid surface area.

The mass transfer coefficient, k, and the interfacial area, A_i, are unknowns in the above equation. For the purposes of this initial study, the mass transfer coefficient is assumed to be constant during the modeling of any specific test. Any variation of the mass transfer coefficient with parameters, such as flow rate, will be developed from test series that specifically vary this parameter. The interfacial area, A_i, varies dramatically over time as the mass is transferred from the solid phase into the water phase. The interfacial area is assumed to be a direct function of the time-dependent mass of the solid particles raised to an exponent X, or:

$$A_i = a\, M^X \qquad [10]$$

where a is a constant (m^2/kg^X), M is the mass of the solid particles (kg), X is the exponent on the solid mass. The constant a is determined using the initial solid mass and the initial surface area, which is based on initially spherical particles.

Using the definition of the interfacial area, the mass transfer relationship can then be written as:

$$\dot{m} = k\, a\, M^X\, S_\ell\, \rho_f \left(C_s - C\right) \qquad [11]$$

The fitting parameters for any given simulation run are the mass transfer coefficient, k, and the exponent X. The mass transfer model presented here is intentionally kept simple to easily vary *k* and *X* parameters to fit the experimental data and to determine their influence on this fit.

In general, the exponent *X* is a measure of the variation of surface area with mass. For instance, for spherical particles, *X* is simply 2/3; for long cylinders, *X* becomes 0.5 where the length is constant (Powers et al., 1994). If the surface changes from smooth to rough (e.g., pitted), the exponent may be less than 0.5. Similarly, if the surface starts out rough and becomes smooth, the exponent may be greater than 1.0.

The exponent *X* may also implicitly include the effect of particle mass and particle size on the mass transfer coefficient, such as the Reynolds number effect, because the mass transfer coefficient, k, is assumed to be constant for each experiment during this initial model development. This influence has been investigated to a limited degree by systematic variation of some parameters, such as flow rate, to determine whether the values of k and X vary systematically with the parameter of interest.

6.2 Simulation Model

For the saturated flow tests, two simulation models were developed for the initial data-model comparisons. Both models are one-dimensional. The two models only differ in the bed height of the energetic material. As discussed in Section 4.5, there are two distinct ranges of bed heights, which are between 0.52 and 0.57 cm and between 2.62 and 2.83 cm. Model meshes were developed for nominal bed depths of 0.5 cm and 2.75 cm as shown in Figure 59. For simplicity, only two different bed depths were considered; a nominal 0.5 cm bed depth for MT6, 7, 8, 8b, 8c, and 8d, and a nominal 2.75 cm bed depth for MT9b2, 9b3, 10, 13, and 14. The bed is placed vertically in the center of model. For the 0.5 cm bed height model, the computational domain is discretized using 26 elements with the bed including four of the elements. For the experiments with the 2.75 cm bed depth, the domain is discretized into 55 elements with 20 of the elements comprising the bed.

For the pulsed test, which is an unsaturated flow experiment, a different mesh than those for the saturated flow tests was developed because the column dimensions were different. The bed depth in the experiment was 0.49 cm, which was rounded off to 0.5 cm for the model. This mesh is shown in Figure 60. The computational domain is 59 elements total, with 10 elements in the bed. The individual elements in the energetic material bed are not shown due to their small size relative to the total model domain.

In this initial model development phase, only dissolution of RDX is considered. Once the behavior of the mass transfer coefficient and the surface area is understood for RDX, the data for TNT will be investigated to determine if the RDX relationships apply to TNT.

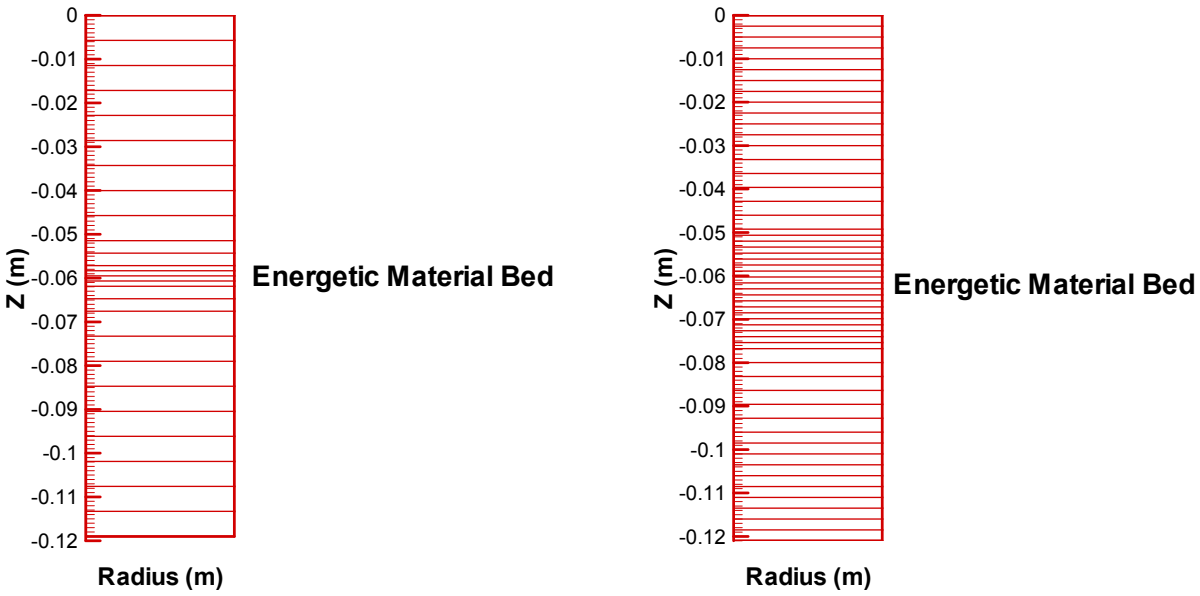

(a) 0.5 cm Bed Depth Model (b) 2.75 cm Bed Depth Model

Figure 59. Simulation Models for Saturated Flow Experiments

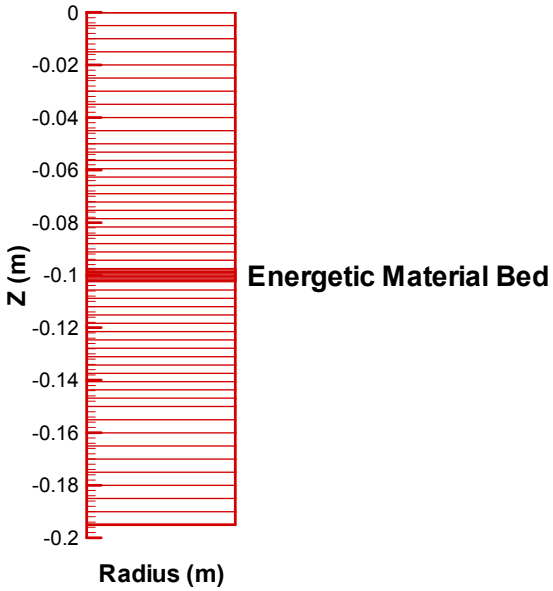

Figure 60. Simulation Models for Unsaturated Flow Experiments

6.3 Simulation Parameters

Diffusion and Dispersion. For simplicity, hydrodynamic dispersion is neglected in the present analysis. Note that the order of magnitude analysis conducted by Imhoff et al. (1993) showed that dispersion is

negligible in similar column tests. The energetic material is assumed to exist only as a separate solid phase and in the liquid phase. Molecular diffusion in the liquid phase is calculated using:

$$D_\ell = \phi(\tau_0\,\tau_\ell)\,D_{m,\ell} \qquad [12]$$

where D_l (m^2/sec) is the diffusion coefficient in the liquid phase (Rosenblatt, 1991), ϕ is the porosity, $\tau_0\,\tau_\ell = \phi^{1/3} S_\ell^{10/3}$ is the saturation dependent tortuosity model of Millington and Quirk (1961), and $D_{m,l}$ (m^2/sec) is the molecular diffusion coefficient in liquid.

Characteristic Curves. The capillary pressure and relative permeability of the porous media (i.e., the glass beads) is modeled using the standard model of van Genuchten (1980) and Mualem (1976), respectively:

$$p_c = -\frac{1}{\alpha}\left[(S_{ec})^{-1/m} - 1\right]^{1/n} \qquad [13]$$

$$k_{rl} = \sqrt{S_{ek}}\left[1 - \left(1 - S_{ek}^{1/m}\right)^m\right]^2 \qquad [14]$$

$$k_{rg} = \left(1 - S_{ek}\right)^{1/3}\left[1 - S_{ek}^{1/m}\right]^{2m} \qquad [15]$$

where p_c (Pa) is the capillary pressure, k_{rl} and k_{rg} are the liquid relative permeabilities of the liquid and gas phases, respectively, the ratio $1/a$ (Pa) roughly describes the gas entry pressure, and *n and m* are pore-size distribution parameters. The effective saturation for the capillary pressure, S_{ec}, and relative permeability, S_{ek}, are defined as:

$$S_{ec} = \frac{S_l - S_{lrc}}{1 - S_{lrc}} \qquad [16]$$

$$S_{ek} = \frac{S_l - S_{lrk}}{1 - S_{lrk} - S_{gr}} \qquad [17]$$

where S_l is the liquid saturation, S_{lrc} and S_{lrk} are the liquid residual saturation for the capillary pressure and relative permeability, respectively, and S_{gr} is the residual gas pressure. Note that the capillary pressure and relative permeability models are only important in the unsaturated pulse test and during the initial wet-up phase of the saturated flow tests.

Liquid-Solid Sorption. Liquid-solid sorption is included in the simulation through specification of a K_d factor, which is the ratio of the concentration on the solid phase, C_s, divided by the concentration in the liquid phase, C_l, or

$$K_d = \frac{C_s}{C_l} \qquad [18]$$

and K_d has units of mL/g.

Simulation Parameters. Simulation parameters are listed in Table 27. The characteristic curve parameters used in this simulation model have been measured for the glass bead bed as discussed in Section 4.4.

Table 27. Simulation Parameters

Porosity, ϕ (-)	0.3
Intrinsic permeability, K (m^2)	2.4×10^{-11}
RDX molecular diffusivity, D_m (m^2/sec)	7.15×10^{-10}
n (-)	19.9
m (-)	0.05
$1/\alpha$ (Pa)	10,873.0
$S_{lrc}=S_{lrk}$ (-)	0
S_{gr} (-)	0.01

For a given saturated flow test, the simulations mimic the various stages of the experiment. Starting from an initially dry column, the wetting-up stage is modeled for approximately 18-20 hours. After the wetting-up stage, the water flow rate is essentially constant and is based on actual measurements. As the water flows through the bed in the column, RDX mass is transferred from the solid phase to the water, which subsequently flows through the porous media (glass beads) and finally out of the column. The exit RDX concentration as a function of time from the simulations is then compared to the experimental results, and various parameters (k, X, K_d) are modified to improve the simulation results. Generally, the liquid-solid sorption coefficient, K_d, is kept constant or only varied slightly. The mass transfer coefficient, k, and the surface area exponent, X, are changed to improve the model response compared to the experimental data.

7.0 Data Model Comparisons

7.1 Illustrative Simulations Results of Column Experiments

As shown in Figure 61, there are two stages of the outlet concentration data from the experiments; an initial excess mass capacity stage where the exit effluent concentration is essentially constant, and a mass depletion stage where the exit concentration decreases dramatically with time. The exit concentration in the initial excess mass capacity stage is probably limited by the total mass transfer rate (mass transfer coefficient times the surface area) and the fraction of water contacting the particles in this stage. As the energetic material is dissolved and the mass is depleted, the column enters the mass depletion stage. The concentration rapidly decreases with time as the remainder of the energetic material dissolves. In this stage, the surface area of the particles limits the concentration.

The two stages and the response of the model are illustrated in Figures 62 to 64. The effect of changing the mass transfer coefficient, k, the area exponent, X, and the partition coefficient, K_d, is demonstrated for the MT9b2 experiment. Figure 62 shows the effect of the area exponent on the predicted outlet concentration of RDX. Varying the exponent from 2/3 to 2 makes a negligible difference on the values for the initial phase but a large difference on the shape during the depletion stage. The shape changes from concave downward for X=2/3 and X=1, to an approximately linear shape (on a semi-log plot) for X=1.5, to a concave upward shape for X=2. Clearly, the X=2 curve is a reasonable match to the data, especially during the depletion stage. Figure 63 shows the effect of varying the mass transfer coefficient, k, from 1.0×10^{-7} m/s to 1.0×10^{-6} m/s on the outlet concentration response. As the mass transfer coefficient gets larger, the initial peak increases slightly as does the width of the initial peak, while the slope in the depletion stage increases. A relatively narrow range of mass transfer coefficients ($5. \times 10^{-7}$ to $1. \times 10^{-6}$ m/s) seems to bracket the experimental results. Figure 64 shows the effect of varying the liquid-solid sorption coefficient, K_d. The effect is essentially a time shift in the curve as there is a small effect on the initial peak value and the shape during depletion stage. Therefore, variations in k and X are the main focus at present.

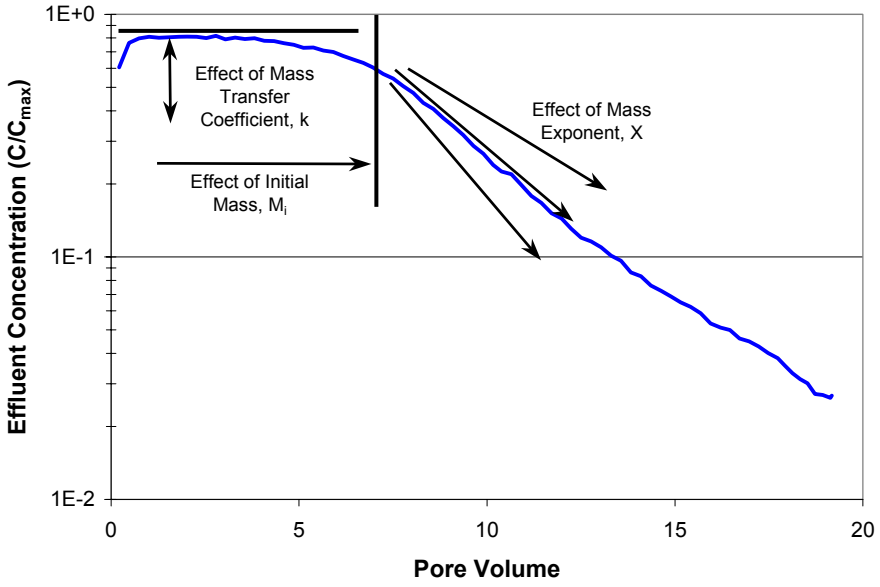

Figure 61. Experimental Stages

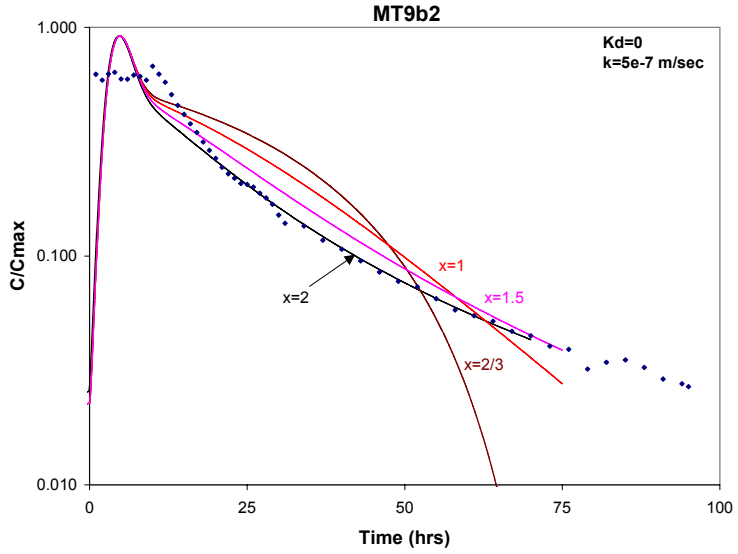

Figure 62. Effect of Surface Area Exponent X on Model Response for MT9b2

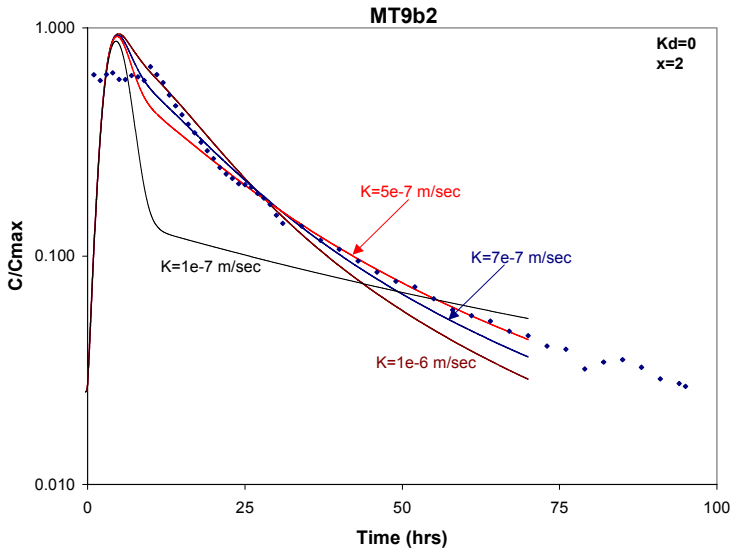

Figure 63. Effect of Mass Transfer Coefficient k on Model Response for MT9b2

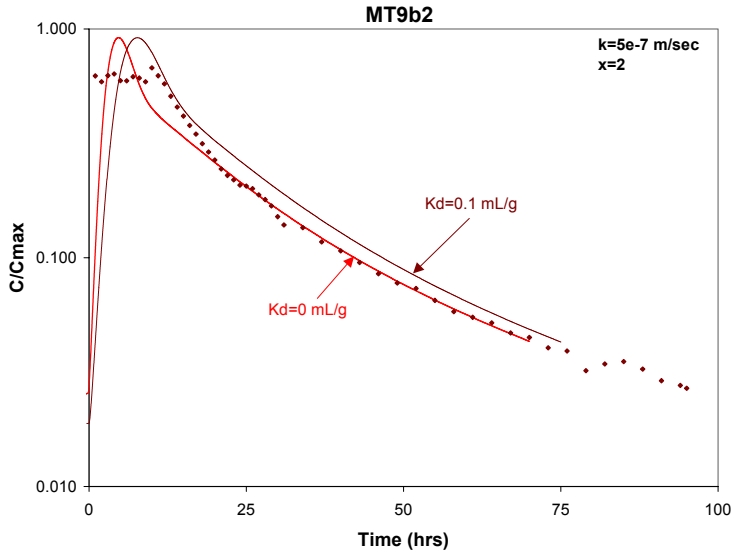

Figure 64. Effect of Solid Sorption Coefficient K_d on Model Response for MT9b2

7.2 Results for Individual Tests

In this section, we will show the comparison of the mass transfer model for given values of the parameters k, X, and K_d that best fit the concentration time history data for each test. The saturated flow tests will be discussed in numerical order followed by the unsaturated (pulse) test. Following this presentation, trends in the fitted parameters (k and X) will be discussed.

7.2.1 Saturated Flow Tests

MT6. Figure 65 shows the results for test MT6, which has a bed depth of 0.5 cm and a high Comp B bed loading of 2.5%. Due to the high bed loading, the initial peak lasts about 900 hours, followed by the depletion stage. For the first 600 hours, the initial excess mass capacity stage is simulated reasonably well including the magnitude. After 600 hours, the model predicts that the column enters the mass depletion stage, while the data indicates the excess mass capacity stage. The mass depletion stage is only qualitatively represented; there are important quantitative differences. For this initial model evaluation phase, this fit is probably adequate. It will be re-evaluated in future work.

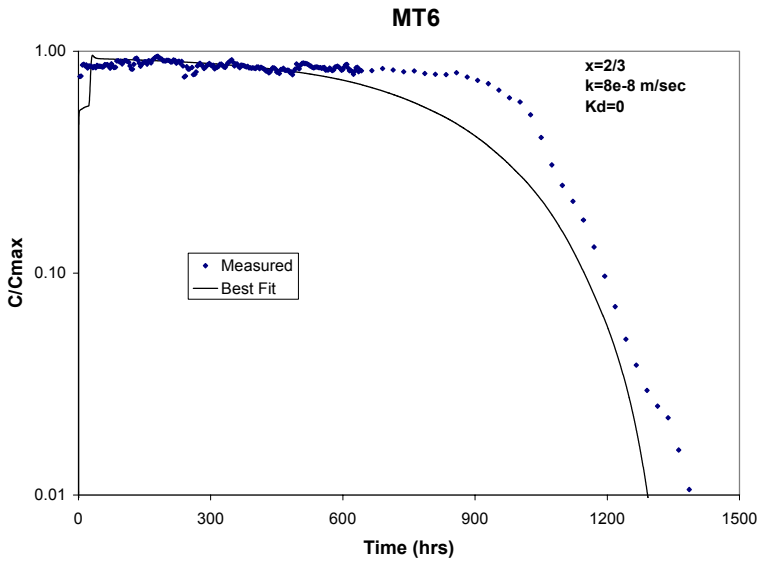

Figure 65. Data-Model Comparison for MT6

MT7. The results for MT7 are shown in Figure 66. MT7 is a small bed depth of 0.5 cm with a Comp B bed loading of 0.25%, which is an order of magnitude lower bed loading than MT6. Similar to MT6, the fit predicts the magnitude of the initial peak well but not the time duration, and the fit for the mass depletion stage is only a qualitative representation of the data. Again, this fit is adequate for this initial evaluation but will be re-evaluated in future work.

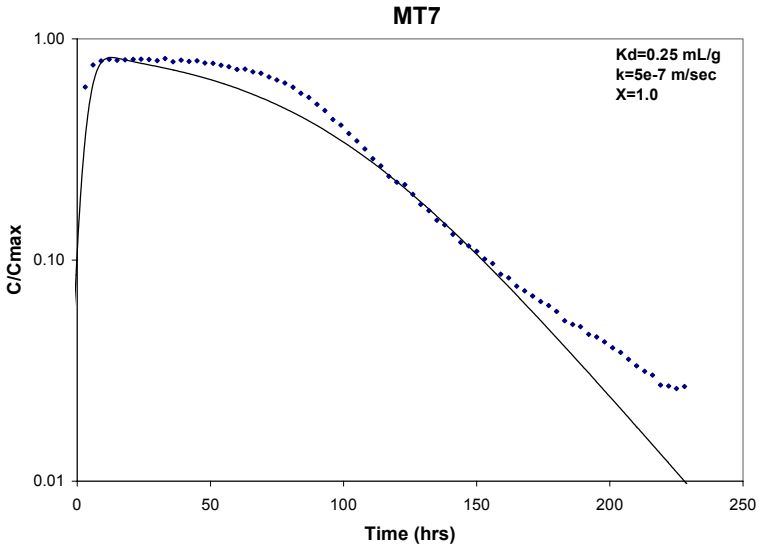

Figure 66. Data-Model Comparison for MT7

MT8. Test series MT8 consisted of four different experiments designated as MT8, MT8b, MT8c, and MT8d. They are all small bed depth (0.5 cm) tests with nominal 0.05% Comp B bed loading. Thus, the initial bed RDX mass is a factor of 50 less than MT6 and a factor of 5 less than MT7. The different tests were designed to investigate the effect of the initial wetting flow rate on the response of the outlet concentration. Additionally, tests 8 and 8d are duplicates to evaluate the repeatability of the experiments. Because the measured results are fairly similar for all the tests, only the fit for MT8 is shown in Figure 67. The mass transfer model does a very good job of fitting MT8, both for the initial excess mass capacity stage and the mass depletion stage.

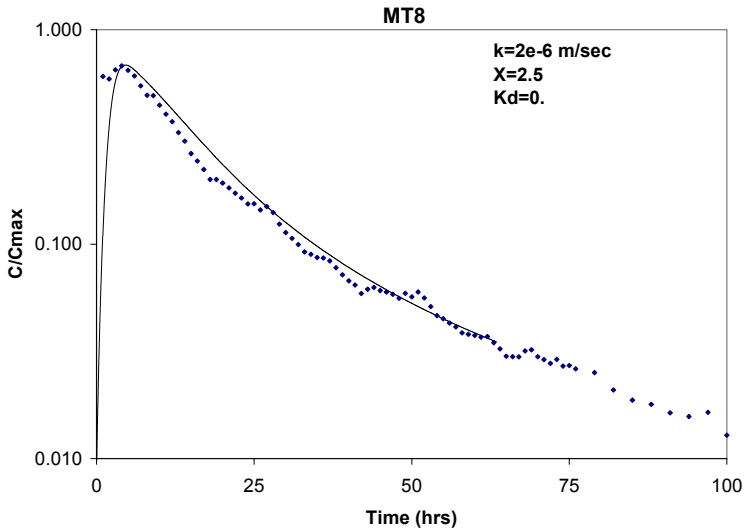

Figure 67. Data-Model Comparison for MT8

MT9. Test series MT9 consists of two separate tests, MT9b2 and MT9b3, with a bed height of 2.75 cm. The Comp B bed loading is 0.01% and 0.05% for MT9b2 and MT9b3, respectively. The fit for MT9b2 in Figure 68 shows that the initial excess mass capacity value is overestimated while the duration is smaller than observed. The mass depletion stage is well represented by the model. For MT9b3, the result shown in Figure 69 is similar to that for MT9b2, although the depletion stage is not quite as well matched. Overall, both fits are reasonably good considering the simplicity of the model.

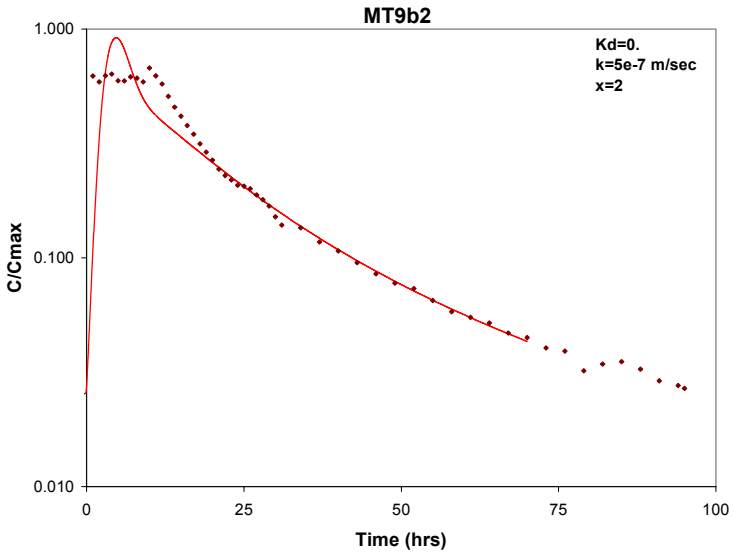

Figure 68. Data-Model Comparison for MT9b2

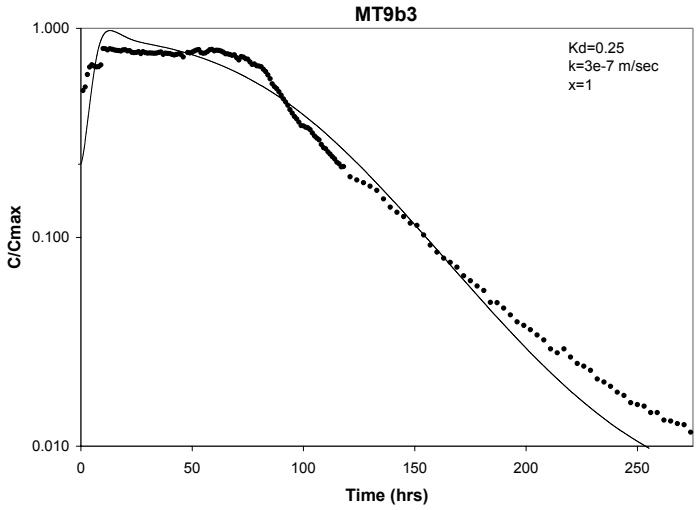

Figure 69. Data-Model Comparison for MT9b3

MT10. Test MT10 has a nominal 2.75 cm bed depth. The Comp B bed loading is 0.03%, or between the values for MT9b2 and MT9b3. The data-model comparison in Figure 70 shows that the initial peak during the excess mass capacity stage is overpredicted, while the duration is underpredicted. The fit during the mass depletion stage is very good.

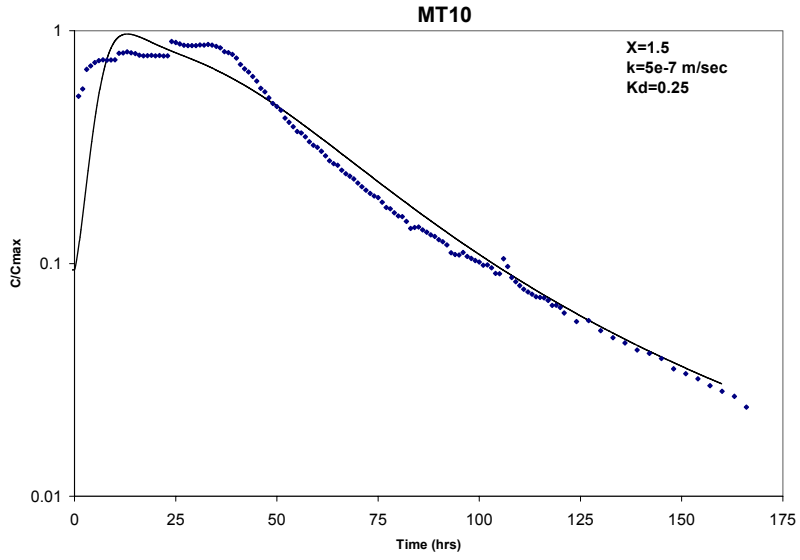

Figure 70. Data-Model Comparison for MT10

MT13. Experiment MT13 is essentially the same as MT10 described above but with a higher mass flow rate through the column to study flow rate effects. The data-model comparison is given in Figure 71. The initial peak is overpredicted. Similar to MT10, the mass depletion stage fit is very good.

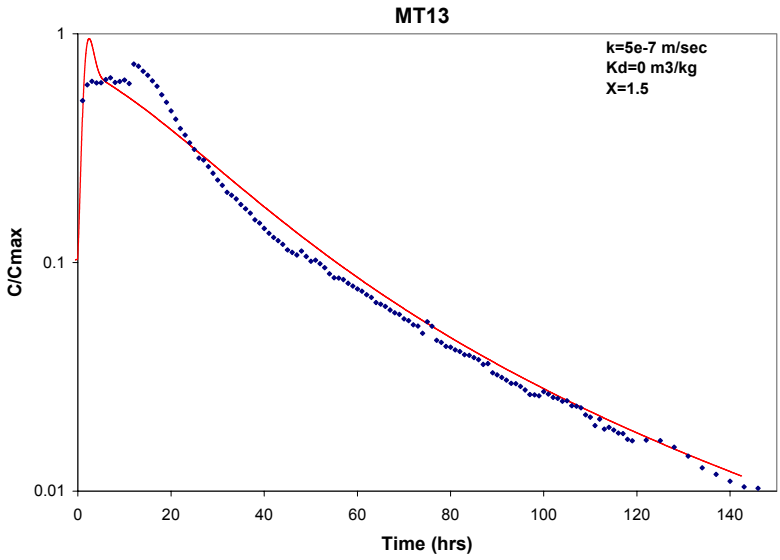

Figure 71. Data-Model Comparison for MT13

MT14. Experiment MT14 is essentially the same as MT10 described above but with a lower mass flow rate through the column to study flow rate effects. The initial peak during the excess mass capacity stage is overpredicted as shown in Figure 72. Similar to MT10 and MT13, the mass depletion stage fit is very good.

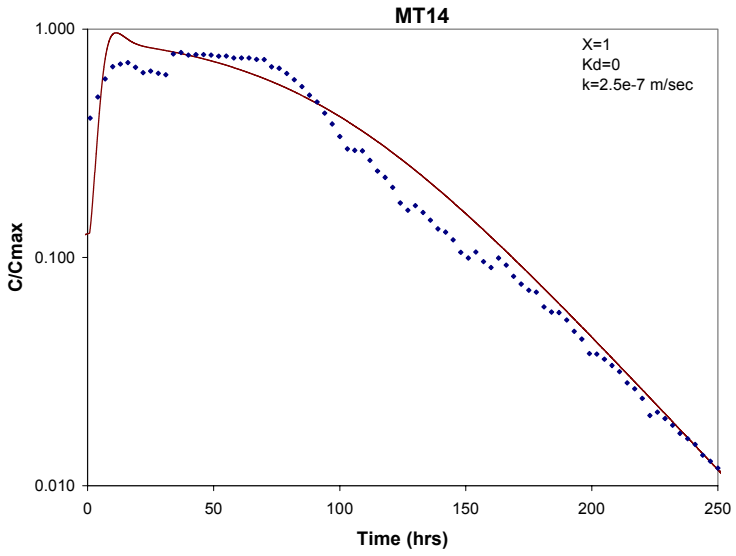

Figure 72. Data-Model Comparison for MT14

7.2.2 Pulse Tests

The MT12 experiment, which is an unsaturated pulse test, was simulated with T2TNT. The experimental setup is different than for the saturated flow tests because the column has a larger diameter. Simulation of this experiment provides for a good test of the model at a different length scale as well as an evaluation for unsaturated flow conditions.

The data-model comparisons are shown in Figures 73 through 75. Figure 73 compares the time-dependent RDX concentration exiting out of the column, while Figure 74 shows the water exit flow rate. Figure 75 shows the cumulative RDX exiting the column. The model results show that the RDX effluent concentrations (Figure 73) were mostly lower than the data for the first two sets of pulses. In the last set of pulses, the two values are reasonably close. The exit flow rate shown in Figure 74 shows similar differences in that the predicted flow rate is much different than the data for the first two pulse sets, while the last pulse set is similar to the data. The combination of effluent concentration and water flow equal the cumulative mass exiting the column, which is shown in Figure 75. In this figure, the data and model predictions are similar. Differences in the exit concentration are offset by differences in the mass flow rate such that the total mass transfer is well predicted. These differences point to the need to investigate the two-phase characteristic curves more closely as these curves dominate the short-term flow variability in the model predictions.

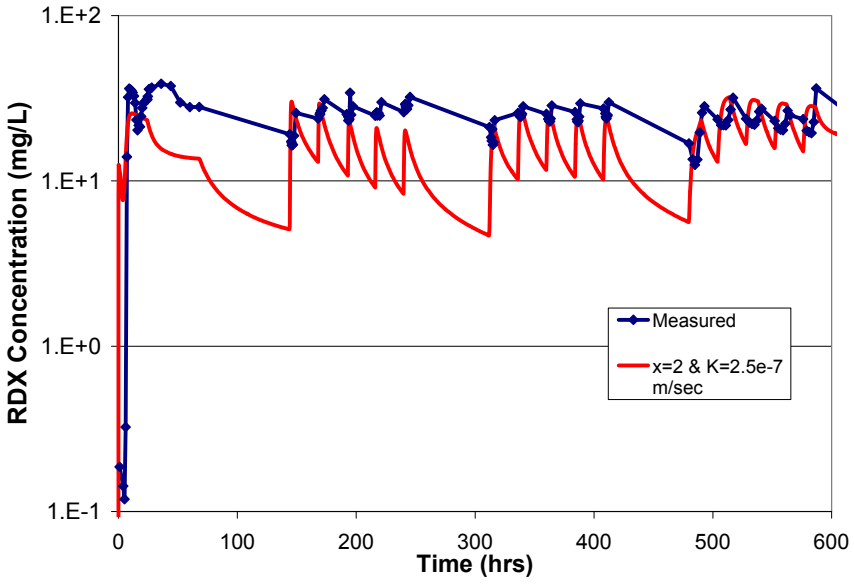

Figure 73. Data-Model Comparison for MT12 for Exit RDX Concentration

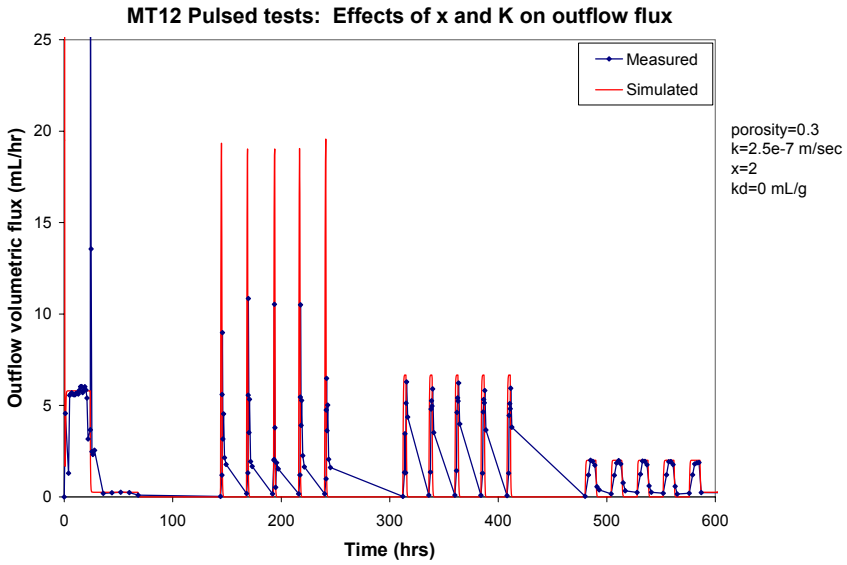

Figure 74. Data-Model Comparison for MT12 for Outflow Volumetric Water Flux

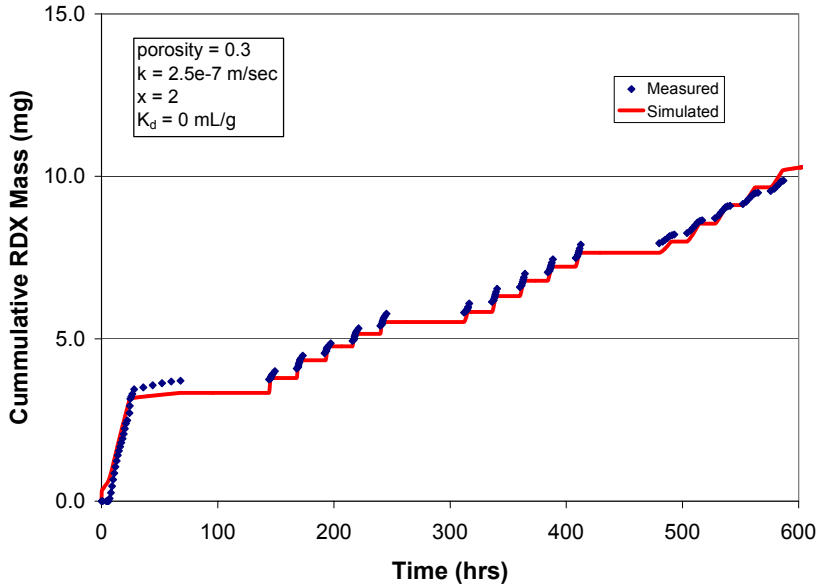

Figure 75. Data-Model Comparison for MT12 for Cumulative RDX Mass

7.3 Mass Transfer Parameters

Table 29 summarizes the best fits for the various mass transfer parameters for each experiment. The values from the unsaturated pulse test (MT12), which has a different column diameter, are consistent with the saturated flow values, so the model does not seem to be length-scale dependent. Changes in the value of K_d only result in a time shift. Thus, the value of K_d is not important in determining the shape of the curves. Initial parametric results are summarized below.

Table 28. Mass Transfer Parameters

	k (m/s)	X	K_d (mL/g)
Saturated Tests			
MT6	8.e-8	0.67	0.
MT7	5.e-7	1.0	0.25
MT8/8b/8c/8d	2.e-6	2.5	0.
MT9b2	5.e-7	2.	0.
MT9b3	3.e-7	1.	0.25
MT10	5.e-7	1.5	0.25
MT13	5.e-7	1.5	0.
MT14	2.5e-7	1.	0.
Pulse Test – Unsaturated			
MT12	2.5e-7	2.	0.

- Effect of Initial Wetting Phase Flow Rate (MT 8/8b/8c/8d) – No effect is seen in the simulation parameters as the fitting parameters are the same.

- Effect of Flow Rate (MT14, MT10, MT13 in order of increasing flow rate) – The fitting parameters show a small variation. The mass transfer coefficient and the area exponent may decrease with increasing flow rate. Additional tests are necessary to further evaluate possible flow rate effects.

- Effect of Bed Loading (MT8, MT7, MT6 in order of increasing bed loading) – The mass transfer coefficient, k, and the exponent, X, decrease significantly with increasing bed loading. This trend will be discussed in more detail below.

- Effect of Bed Depth (MT8 and MT9b2 in order of increasing bed depth and loading) – The values of k and X decrease with increased bed depth and loading similar to the bed loading effect.

- Effect of Initial Mass

  Low Mass (MT8, MT9b2)
  Medium Mass (MT10)
  High Mass (MT7, MT9b3)

In general, the values of k and X decrease as the initial mass increases.

The trends indicate that the initial mass is significant for the duration of the C/C_{max} plateau. A dependence on flow rate is possible and additional tests are needed to evaluate this further. Figures 76 and 77 plot the values of k and X as a function of the initial RDX mass per unit area, respectively. The trend of decreasing values of k and X with increasing mass per unit area is clearly seen in the two plots.

In addition, the MT12 pulsed test parameters are plotted on the curves indicating consistency between the parameters derived from the saturated flow test and for unsaturated conditions.

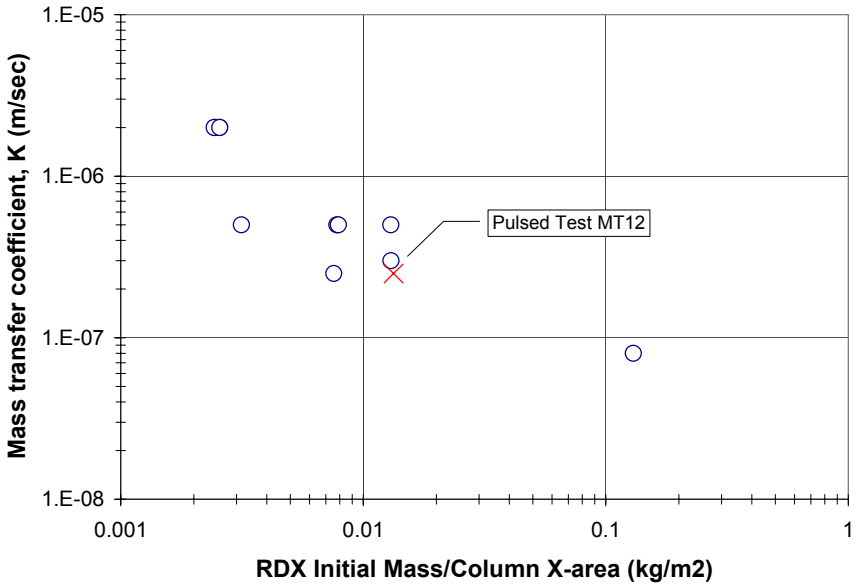

Figure 76. Effect of Initial RDX Mass per Unit Area on Mass Transfer Coefficient, k

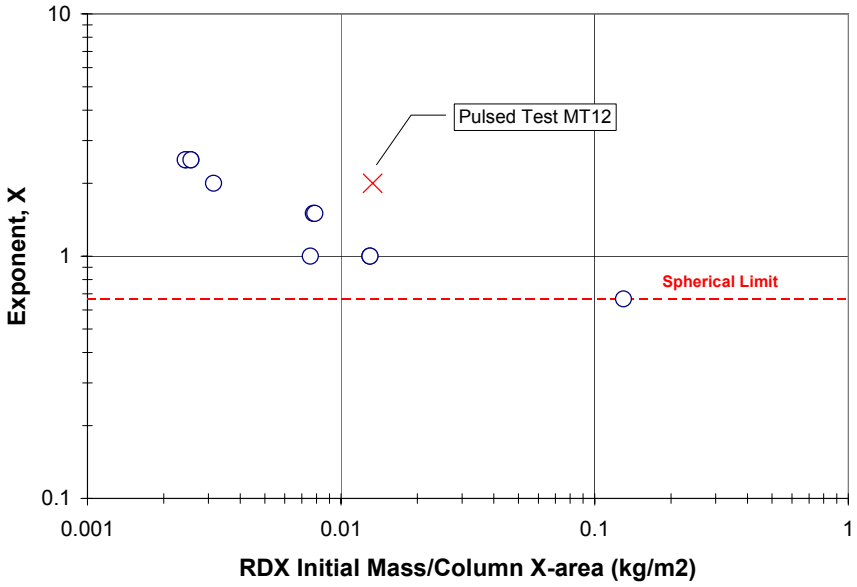

Figure 77. Effect of Initial RDX Mass per Unit Area on Interfacial Area Exponent, X

7.4 Discussion

A simple mass transfer formulation has been added to T2TNT to simulate the present experiments for RDX dissolution and transport. The model contains two fitting parameters – the mass transfer coefficient from the solid phase to the water, k, and an exponent on the solid surface area function, X. The parameters are varied to try to match the measured exit RDX concentration as a function of time. There are two general regions in the outlet concentration data – an initial excess mass capacity stage and a mass depletion stage. The mass transfer coefficient, k, is most important in the prediction of the initial stage, while the area parameter X is most important in the depletion stage. A sorption coefficient, K_d, is also included in the model, but it is essentially a time shift parameter that has little influence on the shape of the curve.

The parameters were varied for the individual experiments, and most of the fits match the data well. Saturated flow and an unsaturated pulse experiment were modeled. The values of k and X are reasonably consistent for the two types of tests (saturated steady-state and unsaturated transient), and the values tend to decrease with an increasing mass density. Variation of the parameters with the flow rate is possible, but additional experiments are needed to further evaluate this possible influence.

The above simulations are only for a single particle size of approximately 100 μm diameter. While some experiments were conducted for 1000 μm diameter particles, these tests were not simulated with the present model. Due to the small number of particles in some of these tests, a two-dimensional model considering bypass flow needs to be developed. At present, only one-dimensional models have been considered.

Two-dimensional models may also be used to improve the prediction of the initial peak. In many simulations, the experimental peak outlet concentration is much lower than the predicted value. This difference suggests that a finite amount of water may be bypassing the bed even for the 100 μm diameter particles, possibly due to wall effects.

Further development of the mass transfer correlation may try to combine the mass transfer coefficient and surface area into a lumped mass transfer coefficient approach similar to that of Powers et al., 1992.

Overall, this initial mass transfer model successfully fit the experimental data for the 100 μm particles. Further development of the model, including development of a two-dimensional model, is needed. Additional data should be obtained to further exercise the model to determine its strengths and weaknesses, especially for different particle sizes and for variation in the flow rate.

8.0 Summary

8.1 Results to Date

This effort focused on experimental measurement of the solid phase energetic material mass transfer process using laboratory porous media columns. The principal factors (pore fluid velocity, temperature, energetic material initial mass and particle size, etc.) that influence the mass transfer process were evaluated individually to assess variations in the magnitude of solute (e.g. RDX and TNT) effluents. Summary results are as follows:

- RDX effluent concentrations mostly near C_{max}
- Water Flow Rate has minimal impact (impact on depletion phase only)
- Water Pulse limits C/C_{max} vs. continuous flow
- Temperature has major impact
- EM Initial Mass important in duration of peak effluent C/C_{max}
- EM Bed Depth/Load not important
- EM Particle Size influences depletion phase
- Two stage mass transfer
  - excess mass capacity stage - high C/C_{max} ratio
  - mass depletion stage - declining C/C_{max} until exhaustion

Notable was the observation that under most circumstances, the effluent concentrations were very high, near the maximum controlled by temperature dependent water solubility. Figure 78 shows the peak concentration of RDX and TNT in many of the experiments. The average RDX concentration was about 31 mg/L (~75% C/C_{max}) and TNT was about 43 mg/L (~33% C/C_{max}). This implies that rainfall can induce a rapid mass transfer of RDX and TNT to soil pore water and additional work is needed to assess the impacts to groundwater.

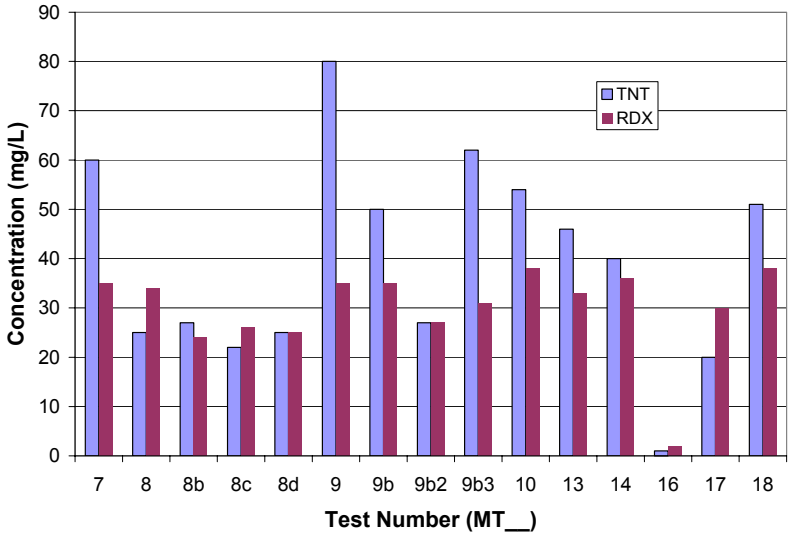

Figure 78. Peak Concentrations of RDX and TNT in the Saturated Flow Tests

A mathematical expression of mass transfer from the solid phase energetic material to the pore water was developed for representation in a computational model (T2TNT). This model was used to derive coefficients of mass transfer from the data and resulted in a very good first approximation of the process. Summary results include:

- Simple mass transfer formulation does a good job of fitting the experimental data for a particle size of 100 μm.
- The mass transfer model parameters are consistent between saturated and unsaturated experiments.
- Additional experiments are needed to further evaluate the potential effect of flow rate.
- A two-dimensional model is needed to model larger particle size experiments due to the possibility of bypass flow.

8.2 Path Forward – Near Term

Further work is needed to: 1) refine the understanding of the mass transfer process with additional laboratory tests and simulation model improvements, and 2) develop computational scenarios that mimic the surface distribution of low order detonation debris for evaluation of the environmental consequences of detonation debris left on military test and training ranges. Work in the near term is needed in the following experimental and modeling areas:

Experimental

- Solid Phase Particle Size - The initial workscope found consistent relationships with a single particle size fraction (100μm) for temperature, initial mass, bed depth, bed loading, and water flow. When a larger particle size (1000 μm) was used, mass transfer relationships based solely on initial mass deviated greatly, indicating that other factors must be included. Data normalization with number of particles, interfacial area and fraction of flow area did not fully describe this phenomenon. Additional tests are needed to evaluate the impact of particle size because the low order detonation process produces a size distribution of debris, which will be evaluated by Pennington, Jenkins and Taylor (ERDC, CP-1155).
- Weathered Energetic Material - Surface deposits of visible (e.g. large) energetic materials exposed to weathering show a red-brown coating indicative of chemical reactions. The nature of sunlight induced TNT polymerization and persistence of these weathered deposits may imply a lower mass transfer rate compared to virgin material. Test results are needed to evaluate the impact of weathering on the mass transfer process.
- Surface Deposits - Previous test designs used near surface buried deposits (~ 5-10 cm below the surface) necessary to evaluate initial mass transfer processes. Energetic material burial increases the duration and contact with soil moisture compared to surface deposits. Transient wetting on surface

deposits from precipitation may delay or diminish mass transfer compared to continuously wet conditions below the surface.

- Low Order Detonation Debris – Initial laboratory tests with low order detonation debris showed consistent results compared to the Comp B test material. However, this debris contained only a small mass of energetic material, potentially not even as a separate solid phase. Low order detonations at NAVEOD Blossom Point (mid-September 2002) will provide additional material and will be characterized by particle size distribution and nature of energetic material (by electron microscopy, Susan Taylor, CRREL). Explosive material shipping containers have been sent to Blossom Point for use in transporting these materials back to Sandia. Collaboration with Susan Taylor will provide great insight into methods to evaluate the physical nature of the energetic material both before and after mass transfer laboratory tests.

Modeling

- Energetic Material Mass Transfer Correlations - Data model comparisons to date used a constant mass transfer coefficient and an exponent on the mass to describe variations in the slope of the decline phase in the experimental data. More work is needed to develop correlations to describe the variation in mass transfer coefficient and the mass exponent on dynamic parameters such as the flow rate, particle size, etc. as conditions evolve and the particle mass declines.
- 2-d Effects Model - Simulation model evaluations used 1-d formulations to date. The particle size effects indicate that 2-d effects involving flow area contact with the energetic material particles may be important in describing the average effluent from contact and non-contact areas, especially if there are only a few large particles or "hot spots". A 2-d formulation of T2TNT with the mass transfer correlation derived above can be used to evaluate the phenomenon with linkages to experimental efforts noted above.
- Screening assessments – The 2-d effects model can begin to be used to evaluate environmental impacts from weather driven mass transfer to soil pore water. Spatial distribution of energetic material particles in pore space with varying proportions of pore fluid contact and non-contact regions can provide an indication of the spatial density of energetic material deposits that drive exceedances in groundwater contamination criteria. Simple models would be used with measured low order detonation debris and the mass transfer correlations derived above to investigate the influence of weather on ground water concentrations of RDX and TNT.

8.2 Path Forward – Long Term

Completion of laboratory-scale mass transfer tests and development of a preliminary analysis tool have provided a basic understanding of the environmental impacts of low order detonation debris.

Confident application for range management decisions requires validation of laboratory test data at field scale.

Design and construction of pilot scale caisson tests can accomplish this, where low order detonation debris can be seeded into soil columns buried into the ground (or in a greenhouse). Caisson tests will be performed with and without plants to evaluate the effect of the RDX and TNT transport to the pore water. Time sequenced soil pore water samples can be obtained and the data linked to changes in surface weather conditions (natural and precipitation supplemented). Adjustments in the simulation model may be needed to refine effects observed at field scale for improved situational analysis for military range specific applications. The T2TNT simulation model will be modified to include the effect of trees and plants that might be useful for mitigation of RDX and TNT transport through the root zone.

References

Andraski, B.J., 1997, "Test-Trench Studies in the Amargosa Desert, Southern Nevada: Results and Application of Information to Landfill Covers in Arid Environments," Conference Proceedings, Landfill capping in the semi-arid west: Problems, perspectives, and solutions, Environmental Science and Research Foundation, Idaho Falls, ID, pp. 165-179.

Braud, I., Dantas-Antonino, A.C., Vauclin, M., Thony, J.L., Ruelle, P. (1995). "A Simple Soil-Plant-Atmosphere Transfer Model (SiSPAT) Development and Field Verification*," Journal of Hydrology* 166:213-250.

Braud, I., J. Noilhan, P. Bessemoulin, P. Mascart, R. Haverkamp, and M. Vauclin, 1993, "Bare-Ground Surface Heat and Water Exchanges Under Dry Conditions: Observations and Parameterization," *Boundary-Layer Meteorology*, 66:173-200.

Faybishenko, B., 2000, "Vadose Zone Characterization and Monitoring," Chapter 3 in Vadose zone science and technology solutions, B.B. Loomey and R. W. Falta, eds., Batelle Press, Columbus, OH, pp. 133-509.

Finsterle, S., 1999. ITOUGH2 User's Guide, LBNL-40040, Lawrence Berkeley National Laboratory, Berkeley, CA.

Hawari, J., 2000. Biodegradation of RDX and HMX: From Basic Research to Field Application. In Biodegradation of Nitroaromatic Compounds and Explosives, J. Spain, J. Hughes, H. Knackmuss eds. Lewis Publishers, Boca Raton, FL Chapter 11, pp 277-310.

Imhoff, P.T., P.R. Jaffe, and G.F. Pinder, 1993. An experimental study of complete dissolution of a nonaqueous phase liquid in saturated porous media. Water Resources Research, Vol. 30, No. 2, pp 307-320, February 1993.

Klute, A., 1986. Water Retention: Laboratory Methods. In Methods of Soil Analysis, Part 1, Physical and Mineralogical Methods, Second Edition, A. Klute, Ed. American Society of Agronomy, Inc. and Soil Science Society of America, Inc. Madison, WI. 1986.

Kutilek, M., and D.R. Nielsen, 1994, "Soil Hydrology, Cremlingen-Destedt," Catena-Verl., as referenced by Faybishenko, 2000.

McGrath, C.J.; Review of formulations for Processes Affecting the Subsurface Transport of Explosives. Technical Report IRRP-95-2; U.S. Army Engineer Waterways Experiment Station: Vicksburg, MS, 1995.

McLellan, W.L., W.R. Hartley, M.E. Brower. 1988. Hexahydro-1,3,5-Trinitro-1,3,5-Triazine (RDX) Health Advisory. US Environmental Protection Agency, Office of Drinking Water, Washington, D.C. PB90-273533, November 1988.

Miller, C.T., M.M. Poirier-McNeill, and A.S. Mayer, 1990. Dissolution of trapped nonaqueous phase liquids: Mass transfer characteristics. Water Resources Research, Vol 26, pp 2783-2796, 1990.

Millington, R.J., and J.M. Quirk, 1961, "Permeability of porous solids," Trans. Faraday, Soc., 57:1200-1207.

Mualem, Y., 1986. Hydraulic Conductivity of Unsaturated Soils: Prediction and Formulas. In Methods of Soil Analysis, Part 1, Physical and Mineralogical Methods, Second Edition, A. Klute, Ed. American Society of Agronomy, Inc. and Soil Science Society of America, Inc. Madison, WI. 1986.

Phelan J.M., M. Gozdor, S.W. Webb, and M. Cal, 2000, "Laboratory Data and Model Comparison of the Transport of Chemical Signatures From Buried Landmines/UXO," SPIE 14th International Symposium on Aerospace/Defense Sensing, Simulation, and Controls, Orlando, FL, April 2000.

Phelan, J.M. and J.L. Barnett. 2001. Phase Partitioning of TNT and DNT in Soils. Sandia National Laboratories Report SAND2001-0310, Albuquerque, New Mexico. February 2001.

Phelan, J.M., and Webb, S.W., 1997. "Environmental Fate and Transport of Chemical Signatures from Buried Landmines - Screening Model Formulation and Initial Simulations. Sandia National Laboratories," SAND97-1426, Sandia National Laboratory, Albuquerque, NM.

Phelan, J.M., J.V. Romero, J.L. Barnett, and D.R. Parker, 2002. Solubility and Dissolution Kinetics of Composition B Explosive in Water. Sandia National Laboratories Report SAND2002-2420, July 2002.

Phelan, J.M., P.J. Rodacy and J.L. Barnett, 2001. Explosive Chemical Signatures from Military Ordnance, Sandia National Laboratories Report SAND2001-0755, Albuquerque, New Mexico. April 2001.

Phelan, J.M., S.W. Webb, J.L. Barnett, M. Gozdor and M. Cal, 2001. Analysis of Landmine Explosive Chemical Soil Transport using T2TNT. In preparation for SPIE 15th International Symposium on Aerospace/Defense Sensing, Simulation, and Controls, Orlando, FL, April 2001.

Plumb, O.A., 1991, "Heat Transfer During Unsaturated Flow in Porous Media," in Convective Heat and Mass Transfer in Porous Media, S. Kakac, et al, eds, Kluwer Academic Publishers, the Netherlands, pp. 435-464.

Powers, S.E., L.M. Abriola, W.J. Weber, Jr. 1994. An experimental investigation of nonaqueous phase liquid dissolution in saturated subsurface systems: Transient mass transfer rates. Water Resources Research, Vol. 30, No. 2, pp 321-332, February 1994.

Powers, S.E., L.M. Abrolia, and W.J. Weber, Jr., 1992, "An experimental investigation of nonaqueous phase liquid dissolution in saturated subsurface systems: Steady state mass transfer rates," Water Resources Research, 28:2691-2705.

Pruess, K. (1991). TOUGH2 – A General-Purpose Numerical Simulator for Multiphase Fluid and Heat Flow, LBL-29400, Lawrence Berkeley Laboratory, Berkeley, CA.

Rosenblatt, D.H.; Burrows, E.P.; Mitchell, W.R.; Parmer, D.L., 1991. Organic Explosives and Related Compounds. In The Handbook of Environmental Chemistry; Hutzinger, O. Ed.; Springer-Verlag: New York, 1991; Volume 3, Part G.

Satterfield, C.N., M. W. Van Eek, and G.S. Bliss, 1978. Liquid-Solid Mass Transfer in Packed Beds with Downward Concurrent Gas-Liquid Flow. AIChE Journal, Vol 24, No. 4, pp 709-717, July 1978.

Singh, J., S.D. Comfort and P.J. Shea, 1998. Long-term RDX sorption and fate in soil. J Environ Qual 27:572-577.

Van Genuchten, M. Th., and P.J. Wirenga. 1986. Solute Dispersion Coefficients and Retardation Factors. In Methods of Soil Analysis, Part 1, Physical and Mineralogical Methods, Second Edition, A. Klute (ed.), American Society of Agronomy, Inc. and Soil Science Society of America, Inc, Madison, WI, 1986.

Verschueren, K.; *Handbook of Environmental Data on Organic Chemicals*, 2nd ed.; Van Nostrand Reinhold Co.; New York, 1983.

Wakao, N., and S. Kaguei, 1982, Heat and Mass Transfer in Packed Beds, Gordon and Breach Science Publishers, New York.

Webb, S.W., and J.M. Phelan, 2000, "Effect of Diurnal and Seasonal Weather Variations on the Chemical Signatures From Buried Landmines/UXO," SPIE 14th International Symposium on Aerospace/Defense Sensing, Simulation, and Controls, Orlando, FL, April 2000.

Webb, S.W., K. Pruess, J.M. Phelan, and S.A. Finsterle, 1999, "Development of a Mechanistic Model for the Movement of Chemical Signatures From Buried Landmines/UXO," SPIE 13th International Symposium on Aerospace/Defense Sensing, Simulation, and Controls, Orlando, FL, April 1999.

Distribution:

1	MS0719	S.M. Howarth, 6131
1	MS0719	J.M. Phelan, 6131
1	MS0719	S.W. Webb, 6131
1	MS0719	J.V. Romero, 6131
1	MS1452	B.W. Marshall, Jr.2552
1	MS1452	P.J. Rodacy, 2552
1	MS1452	J.L. Barnett, 2552
1	MS1452	F.A. Griffin, 2552
1	MS0735	E.K. Webb, 6115
1	MS0735	M. Eliassi, 6115
1	MS9018	Central Technical Files, 8945-1
2	MS0899	Technical Library, 9616
1	MS0612	Review and Approval Desk, 9612 for DOE/OSTI

2 Dr. Robert Holst
Strategic Environmental Research and Development Program
901 North Stuart Street, Suite 303
Arlington, VA 22203

2 Dr. Jeff Marqusee
Strategic Environmental Research and Development Program
901 North Stuart Street, Suite 303
Arlington, VA 22203

1 Dr. Thomas Jenkins
U.S. Army Corps of Engineers
Engineer Research and Development Center
Cold Regions Research and Engineering Laboratory
72 Lyme Road
Hanover, N.H. 03755-1290

1 Dr. Susan Taylor
U.S. Army Corps of Engineers
Engineer Research and Development Center
Cold Regions Research and Engineering Laboratory
72 Lyme Road
Hanover, N.H. 03755-1290

1 Dr. Judy Pennington
U.S. Army Corps of Engineers
Engineer Research and Development Center
Waterways Experiment Station
3909 Halls Ferry Road
Vicksburg, MS 39180-6199

1 Lt. Jeff Lewis, M.Eng.
DRDC-Valcartier
2459 Pie-XI Blvd. North
Val-Belair
QC G3J1X5